



**IMPROVEMENTS TO EMISSIVE PLUME AND  
SHOCK WAVE DIAGNOSTICS AND  
INTERPRETATION DURING PULSED LASER  
ABLATION OF GRAPHITE**

DISSERTATION

Timothy I. Calver, Major, USAF  
AFIT-ENP-DS-21-S-023

**DEPARTMENT OF THE AIR FORCE  
AIR UNIVERSITY**

***AIR FORCE INSTITUTE OF TECHNOLOGY***

---

**Wright-Patterson Air Force Base, Ohio**

DISTRIBUTION STATEMENT A.  
APPROVED FOR PUBLIC RELEASE; DISTRIBUTION UNLIMITED

The views expressed in this document are those of the author and do not reflect the official policy or position of the United States Air Force, the United States Department of Defense or the United States Government. This material is declared a work of the U.S. Government and is not subject to copyright protection in the United States.

AFIT-ENP-DS-21-S-023

IMPROVEMENTS TO EMISSIVE PLUME AND SHOCK WAVE DIAGNOSTICS AND  
INTERPRETATION DURING PULSED LASER ABLATION OF GRAPHITE

DISSERTATION

Presented to the Faculty  
Graduate School of Engineering and Management  
Air Force Institute of Technology  
Air University  
Air Education and Training Command  
in Partial Fulfillment of the Requirements for the  
Degree of Doctor of Philosophy in Applied Physics

Timothy I. Calver, BS, MS

Major, USAF

September 2021

DISTRIBUTION STATEMENT A.  
APPROVED FOR PUBLIC RELEASE; DISTRIBUTION UNLIMITED

AFIT-ENP-DS-21-S-023

IMPROVEMENTS TO EMISSIVE PLUME AND SHOCK WAVE DIAGNOSTICS AND  
INTERPRETATION DURING PULSED LASER ABLATION OF GRAPHITE

DISSERTATION

Timothy I. Calver, BS, MS  
Major, USAF

Committee Membership:

Glen P. Perram, PhD  
Chairman

LTC Michael B. Shattan, PhD  
Member

Lt Col James L. Rutledge, PhD  
Member

ADEDEJI B. BADIRU, PhD  
Dean, Graduate School of Engineering and Management

## Abstract

Emissive plumes are commonly leveraged in laser ablation as optical signatures that reflect physical processes that occur during a laser ablation event. The purpose of this work is to improve the interpretation of common diagnostic techniques used to characterize pulsed laser ablation, to find simple but universal scaling relationships for comparing ablation dynamics across different target materials and ablation conditions, and to provide a comprehensive and systematic analysis of emissive plume and shock wave dynamics for graphite across a range of experimental conditions. Three experiments were performed using two pulsed laser sources: a 4 J/cm<sup>2</sup> nm KrF laser ( $\lambda = 248$  nm), and a 5.70 J/cm<sup>2</sup> frequency-doubled Nd:YAG laser ( $\lambda = 532$  nm). Gas backgrounds consisted of air, argon, nitrogen, helium, and a mixed gas of 70% CO<sub>2</sub> and 30% N<sub>2</sub> for pressures ranging from 1–180 Torr.

Emissive plumes from ablation with a KrF laser were observed with a fast-gated ICCD camera to find and validate new scaling relationships for common ablation diagnostic parameters. Plume shock front trajectories were found and characterized with free expansion, Sedov-Taylor blast wave, and drag models. Initial plume expansion velocities of 1.37–1.98 cm/ $\mu$ s corresponded to plume kinetic energies between 12–25 eV/atom. The plume expands with initial Mach numbers of  $M \sim 48$ , decreasing to  $M \sim 7$  as the emission becomes too weak to detect. The plumes begin with a planar shock front and thickness of a few mean free paths, but evolve to higher dimensionality depending on pressure and mass of the background gas. Non-dimensional factors from a recent study were validated for graphite. The Sedov-Taylor energy released in the sudden ablation is typically 33% the laser pulse energy. Blast energy and plume dimensionality were found to be correlated with stopping distances, which are typically greater than  $10^3$  mean free paths. A new scaling method for Sedov-Taylor energy ratio was proposed and validated for graphite and other target ma-

terials from the literature, enabling comparisons of laser-plume energy coupling between different target materials ablated under varying environmental and system conditions.

Emissive plumes and shock waves were observed with a fast-gated ICCD camera and schlieren imaging to develop and validate an improvement to Sedov-Taylor laser-plume energy coupling analyses. Initial plume expansion velocities of 1.9–3.45 cm/ $\mu$ s corresponding to kinetic energies between 26–74 eV/atom. The emissive plume expands with initial Mach numbers up to  $M \sim 54$  at  $t = 62$  ns, decreasing to  $M \sim 12$  as the emission becomes too weak to detect after several microseconds. The shock wave expands with initial Mach numbers up to  $M \sim 55$  at  $t = 62$  ns, decreasing to  $M \sim 1$  at  $t = 20$   $\mu$ s. Shock detachment locations were determined and then used to define a new limit for sectioning emissive plume data during Sedov-Taylor analysis, improving the accuracy of laser-plume coupling energy estimates. The technique was validated over a range of experimental conditions, with detachment-limited Sedov-Taylor energy values for the emissive plume in agreement with the shock wave energy to within 3–5%. The Sedov-Taylor energy released in the sudden ablation was typically 55–75% of the laser pulse energy. Shock detachment was found to scale with mean free path, which may allow prediction for other gases and pressures.

Emissive plumes and shock waves were observed with a fast-gated ICCD camera and schlieren imaging to examine the morphology of the emissive plume and corresponding ablation shock wave. The imagery was used to determine dependence of plume and shock wave expansion on rectangular and circular laser footprint geometry. Radii of curvature ratios were developed using shock wave imagery and compared to the Sedov-Taylor dimensionality. The 10 Torr shock waves for both geometries exhibit mostly spherical shock fronts, but the Sedov-Taylor dimensionality decreases to planar-cylindrical for the rectangle geometry and cylindrical-spherical for the circular geometry.

## Acknowledgements

This dissertation would not have been realized without the continued assistance, advice, and support of many people over the last three years:

First, I am deeply grateful to my advisor, Dr. Glen Perram, for all of his guidance and support during the research and writing of this dissertation over the last three years.

I would like to express my appreciation to my committee members, Lt Col James Rutledge and LTC Michael Shattan, who provided invaluable contributions to my doctoral experience.

Special thanks is due to LTC Michael Shattan for providing lab space and laser equipment at short notice when my original lab became unavailable during a global pandemic. I am also grateful to Mr. Greg Smith and Mr. Ben Doane for their technical assistance, especially in tracking down equipment so I could construct my experiments.

I would like to extend my sincere thanks to Dr. William Bauer for collecting a graphite imagery dataset in the final days of his PhD efforts at AFIT in 2017, which I analyzed for the first study presented in this dissertation.

I would like to thank my AFTAC Division Chief, Dr. Charles Brennan, and all my AFTAC coworkers for their encouragement and support when I decided to apply to the AFIT in-residence PhD program.

Most importantly, I would like to extend my deepest appreciation and love to my parents for their unwavering encouragement, patience, and steadfast support especially during the longer hours of this endeavor. Without them, none of this would have been possible.

Timothy I. Calver

# Table of Contents

	Page
Abstract .....	iv
Acknowledgements .....	vi
List of Figures .....	ix
List of Tables .....	xv
List of Symbols .....	xvi
I. Introduction .....	1
II. Background .....	6
2.1 Laser Ablation Process Regimes .....	6
2.1.1 Laser-Target Interaction .....	6
2.1.2 Laser-Plume Interaction .....	9
2.1.3 Plume Propagation .....	10
2.2 Optical Plume Imaging Techniques .....	12
2.2.1 Fast Optical Emission Imaging .....	12
2.2.2 Schlieren Imaging .....	13
2.3 Previous Work .....	15
2.3.1 Emissive Plume Dynamics, Shock Strength, and Shock Thickness .....	15
2.3.2 Shock Wave Propagation and Shock Detachment .....	16
2.3.3 Plume and Shock Morphology .....	17
III. Shock front behavior during pulsed laser ablation of graphite .....	19
3.1 Introduction .....	19
3.2 Apparatus and Methodology .....	22
3.3 Results .....	25
3.3.1 Plume Imagery and Shock Front Propagation Speeds .....	25
3.3.2 Diffuse Emission at Early Times .....	37
3.4 Discussion .....	39
3.4.1 Sedov-Taylor Blast Energy .....	39
3.4.2 High Limit Ablated Mass and Hole Depth Estimates .....	41
3.4.3 Non-dimensional Factors for Hole Depth, Fluence, and Pulse Duration .....	43
3.4.4 Shock Thickness and Strength in Graphite and Barium .....	45
3.5 Conclusions .....	49

	Page
IV. Shock front detachment during pulsed laser ablation of graphite .....	51
4.1 Introduction .....	51
4.2 Apparatus and Methodology .....	54
4.3 Results .....	58
4.3.1 Shock wave Propagation Imagery .....	58
4.3.2 Emissive Contact Front Imagery and Propagation .....	62
4.4 Discussion .....	69
4.4.1 Shock Detachment from Emissive Plume .....	69
4.4.2 Sedov-Taylor Blast Energy Comparison: Shock wave and Emissive Contact Front .....	72
4.5 Conclusions .....	77
V. Plume and shock morphology of pulsed laser ablation of graphite .....	79
5.1 Introduction .....	79
5.2 Apparatus and Methodology .....	81
5.3 Results and Discussion .....	84
5.3.1 Rectangular Spot Plume Morphology .....	84
5.3.2 Circular Spot Plume Morphology .....	89
5.3.3 Rectangular Spot Shock Morphology .....	92
5.3.4 Circular Spot Shock Morphology .....	100
5.4 Conclusions .....	105
VI. Conclusions .....	107
6.1 Conclusions .....	107
6.2 Recommendations for Future Work .....	111
Bibliography .....	113

## List of Figures

Figure		Page
1	Schematic of a dual-field-lens schlieren imaging apparatus. ....	14
2	Experimental apparatus includes a vacuum chamber containing a sample target carousel, vertically mounted PIMAX I ICCD camera, and ports for other diagnostic equipment. The target is ablated using a KrF pulsed laser source ( $\lambda = 248$ nm, 25 ns pulse width, average energy 170 mJ per pulse at target). ....	23
3	ICCD camera field of view. The ICCD camera images the xz-plane, capturing the plume's propagation from the target to a distance 5.24 cm from the target. ....	23
4	Graphite ablation plume ICCD image with 369 ns gate delay in air at 10 Torr with no spectral filter. ....	27
5	Centerline intensity profile with a 5-pixel (0.5 mm) row average corresponding to the image in Fig. 4 with peak intensity ( $\diamond$ ) and defined shock front position at 50% peak intensity ( $\times$ ) at $t = 369$ ns with no spectral filter in air at 10 Torr. ....	27
6	Plume shock trajectory for graphite in an air background gas at 10 Torr. The gray vertical error bars represent the z distance error resulting from the ICCD gate width size which increased from 2.2 ns at the earliest shock location to 3.1 ns for the latest shock location. An ICCD pixel size marker denoted with the arrow is included for reference to the distance axis, z. ....	28
7	Location of graphite shock front position in air at 10 Torr with least-square fits to the free expansion (—), Sedov-Taylor (- - -), and drag (.....) models. ....	30
8	Sedov-Taylor fit for graphite in air at 10 Torr. The fit coefficients are $a = 0.544 \pm 0.003$ cm/ $\mu\text{s}^{2/(n+2)}$ , and dimensionality $n = 2.65 \pm 0.12$ . The dotted line is the low limit, $0.316 \pm 0.03$ cm. The high limit is 6.37 cm. ....	35

Figure	Page
9	Graphite plume trajectories in air (×), argon (Δ), argon using the C <sub>2</sub> filter (○), helium (◇), and nitrogen at 10 Torr (□) and nitrogen at 1 Torr (★). Drag fits are represented by dashed lines (---). . . . . 36
10	(a–h) Unfiltered ICCD images demonstrating diffuse emission at early times for graphite in nitrogen at 1 Torr. Images show gate delays from 2.2 ns to 150 ns with emission from the shock front appearing at 84.7 ns (e). The diffuse emission peak intensity occurs at 106.2 ns (f), and has faded by 150.3 ns (h). . . . . 38
11	Sedov-Taylor/laser pulse energy ratio versus stopping distance normalized with mean free path for graphite results in this work (■) compared to barium [52] (Δ), graphite [17, 21, 24] (●), graphite from Márton et. al. [85] (★), graphite from Mahmood et. al. [105] (◆), and titanium (+) and aluminum from Bauer [72] (×). . . . . 40
12	Non-dimensional hole depth, $h^*$ , as a function of non-dimensional fluence, $f^*$ , for graphite in this study (◇), and for various materials $t^* < 1$ (□), $t^* > 1$ (○) from Van Woerkom et. al. [11] . . . . . 45
13	Evolving shock speed (×) and thickness (○) for nitrogen at 1 Torr. . . . . 47
14	Normalized shock strength from shock tube experiments: in N <sub>2</sub> (▶) [69], in Ar (◆) [115] and (●) [110], and pulsed laser ablation: Ba in O <sub>2</sub> at 0.05–0.4 Torr (▲) [52], C in Ar at 0.3 Torr (★) [71], and the present results in N <sub>2</sub> at 1 Torr (■). Predictions from the analytic theory [68] for $s = 0.82$ (—) and $s = 0.64$ (---). . . . . 49
15	Schematic of the experimental apparatus which includes a vacuum chamber containing a sample target, PIMAX 4 ICCD camera, schlieren light source, and schlieren optics. The target is ablated using a Nd:YAG pulsed laser source ( $\lambda = 532$ nm, 12.5 ns pulse width, average energy 90 mJ per pulse at target). . . . . 54

Figure	Page
16	ICCD camera field of view. The ICCD camera views the xz-plane and images the shock wave and emissive plume propagation from the target out to a distance 2.81 cm from the target along the z-axis. The camera field of view is denoted by the dashed lines while the schlieren test region is denoted by the circular shaded area. . . . . 55
17	a) Unprocessed graphite ablation schlieren shock wave image for 7.9 $\mu$ s gate delay in nitrogen at 10 Torr with shock wave and plume visible in the LED illuminated region, b) Image processed with background and flat corrections, c) Centerline intensity profile with a 5-pixel (0.22 mm) row average with shock wave position approximately 1.5 cm from the target surface at t = 7.9 $\mu$ s. . . . . 59
18	Schlieren shock wave image series for graphite in 10 Torr nitrogen from 1.6 $\mu$ s to 17.3 $\mu$ s after the laser pulse. Both the emissive plume and the shock wave (dark band) are visible in the early images with the emissive plume fading at later times. . . . . 59
19	Shock wave trajectory and corresponding Mach numbers for graphite in a nitrogen background gas at 10 Torr. Gray vertical error bars for each series represent the z distance error and Mach error resulting from the ICCD 20 ns gate width. . . . . 60
20	a) Shock wave trajectories for graphite in nitrogen gas at 3–180 Torr, b) Shock wave trajectories for graphite in nitrogen, argon, and CO <sub>2</sub> /N <sub>2</sub> for background pressures of 3–180 Torr. . . . . 61
21	a) Graphite ablation plume ICCD image with 175.2 ns gate delay in nitrogen at 10 Torr, b) Centerline intensity profile with a 5-pixel (0.22 mm) row average corresponding to the image in Fig. 21a with peak intensity and defined contact front position at 50% peak intensity for t = 175.2 ns in nitrogen at 10 Torr. . . . . 62
22	a) Emissive plume contact front trajectory for graphite in a nitrogen background gas at 3–180 Torr. Drag model fits are represented by dashed lines, b) Emissive plume contact front Mach numbers for graphite in a nitrogen background gas at 3–180 Torr. . . . . 63

Figure	Page
23	a) Sedov-Taylor fit to shock wave trajectory of graphite in a nitrogen background gas at 10 Torr with the fit extending to the Sedov-Taylor low limit $z_{low} = 0.176 \pm 0.003$ cm, b) Expanded view of shock detachment between emissive contact front and shock wave for graphite in a nitrogen background gas at 10 Torr along with a zoomed inset of the detachment point. The shock detachment point, $z_D = 0.39 \pm 0.05$ cm, occurs near the crossing point of the shock wave ST fit and emissive contact front drag fit. 95% confidence intervals for the ST and drag fits are provided. . . . . 70
24	Shock detachment compared to mean free path in nitrogen, argon, and CO <sub>2</sub> /N <sub>2</sub> for background pressures of 3–180 Torr along with power law fit curves. Fit exponents are 0.357 for Ar, 0.308 for N <sub>2</sub> , and 0.283 for 70% CO <sub>2</sub> 30% N <sub>2</sub> . . . . . 71
25	a) Sedov-Taylor energy, $E_{ST}$ , and b) dimensionality, $n$ , for shock detachment-limited emissive plume (black markers) and schlieren-imaged shock wave (blue markers) for 3–180 Torr in N <sub>2</sub> , Ar, and CO <sub>2</sub> /N <sub>2</sub> . . . . . 76
26	Experimental apparatus includes a vacuum chamber containing a sample target, PIMAX 4 ICCD camera, white light LED, and schlieren optics. The target is ablated using a Nd:YAG pulsed laser source ( $\lambda = 532$ nm, 12.5 ns pulse width, average energy 90 mJ per pulse at target). . . . . 82
27	Emissive ICCD image series demonstrating plume morphology for ablation of graphite in nitrogen at 10 Torr for the rectangular laser footprint viewed along the short x-axis (a–f), and long y-axis (g–l), with gate delays from 100 ns to 820 ns. . . . . 85
28	Emissive ICCD image series at $t = 618$ ns demonstrating plume morphology for ablation of graphite in nitrogen (a–d), argon (e–h), and 70% CO <sub>2</sub> /30% N <sub>2</sub> (i–l), for a rectangular laser footprint viewed along the short x-axis, in pressures ranging from 3 to 180 Torr. . . . . 87
29	Emissive ICCD image series at $t = 618$ ns demonstrating plume morphology for ablation of graphite in nitrogen (a–d), argon (e–h), and 70% CO <sub>2</sub> /30% N <sub>2</sub> (i–l), for a rectangular laser footprint viewed along the long y-axis, in pressures ranging from 3 to 180 Torr. . . . . 88

Figure	Page
30	Emissive ICCD image series demonstrating plume morphology for ablation of graphite in nitrogen at 10 Torr for a circular laser footprint with gate delays from 120 ns to 830 ns. . . . . 90
31	Emissive ICCD image series at $t \sim 330$ ns demonstrating plume morphology for ablation of graphite in nitrogen (a–d), argon (e–h), and 70% CO <sub>2</sub> /30% N <sub>2</sub> (i–l), for a circular laser footprint in pressures ranging from 3 to 180 Torr. The slightly different delays are due to minor gate width differences between each series. . . . . 92
32	Schlieren ICCD image series demonstrating shock wave morphology for ablation of graphite in nitrogen at 10 Torr for a rectangular laser footprint viewing the short x-axis with gate delays from 6.3 $\mu$ s to 20 $\mu$ s. Hemispheres are superimposed on the images, corresponding to the shock location normal to the target surface, along with two 45 degree guidelines and a 90 degree (normal) guideline used to estimate radii of curvature ratios. . . . . 94
33	Schlieren ICCD image series demonstrating shock wave morphology for ablation of graphite in nitrogen at 10 Torr for a rectangular laser footprint viewing the long y-axis with gate delays from 6.3 $\mu$ s to 20 $\mu$ s. . . . . 95
34	Schlieren image series at $t = 14.6$ $\mu$ s demonstrating plume morphology for ablation of graphite in nitrogen (a–c), argon (d–f), and 70% CO <sub>2</sub> /30% N <sub>2</sub> (g–i), for a rectangular laser footprint viewing the short x-axis in pressures ranging from 10 to 180 Torr. . . . . 97
35	Schlieren image series at $t = 14.6$ $\mu$ s demonstrating plume morphology for ablation of graphite in nitrogen (a–c), argon (d–f), and 70% CO <sub>2</sub> /30% N <sub>2</sub> (g–i), for a rectangular laser footprint viewing the long y-axis in pressures ranging from 10 to 180 Torr. . . . . 98
36	Schlieren ICCD image series demonstrating shock wave morphology for ablation of graphite in nitrogen at 10 Torr for a circular laser footprint with gate delays from 6.3 $\mu$ s to 20 $\mu$ s. . . . . 101

Figure		Page
37	Schlieren image series at $t = 14.5 \mu\text{s}$ demonstrating shock wave morphology for ablation of graphite in nitrogen (a–c), argon (d–f), and 70% $\text{CO}_2$ /30% $\text{N}_2$ (g–i), for a circular laser footprint in pressures ranging from 10 to 180 Torr. ....	103

## List of Tables

Table		Page
1	Thermodynamic and transport properties of pyrolytic graphite samples. ....	24
2	Free expansion and drag model fit results for plume propagation. ....	31
3	Sedov-Taylor fit results. ....	34
4	Properties of pyrolytic graphite samples. ....	56
5	Free expansion velocity and kinetic energy for the emissive plume. ....	65
6	Shock Detachment locations for graphite ablation in N <sub>2</sub> , Ar, and 70% CO <sub>2</sub> 30% N <sub>2</sub> gases from 3–180 Torr. ....	71
7	Sedov-Taylor fit results for schlieren shock wave and emissive plume in N <sub>2</sub> , Ar, and 70% CO <sub>2</sub> 30% N <sub>2</sub> gases. ....	74
8	Sedov-Taylor energy for shock detachment-limited emissive plume and schlieren shock wave in N <sub>2</sub> , Ar, and 70% CO <sub>2</sub> 30% N <sub>2</sub> gases. ....	77
9	Properties of pyrolytic graphite samples. ....	83
10	Rectangular laser spot Sedov-Taylor dimensionalities and radius of curvature ratios for ablation shock waves. ....	99
11	Circular laser spot Sedov-Taylor dimensionality and radius of curvature ratio for ablation shock wave. ....	105

## List of Symbols

$\alpha$  Absorption coefficient,  $\text{cm}^{-1}$

$a$  Sedov-Taylor fit parameter,  $\text{cm}/\mu\text{s}^{2/(2+n)}$

$A_L$  Laser spot area,  $\text{mm}^2$

Ar Argon gas

$b$  Sedov-Taylor fit parameter

$\beta$  Drag Coefficient,  $\mu\text{s}^{-1}$

$c$  Speed of light, m/s

$\text{CO}_2/\text{N}_2$  Mixed gas: 70% Carbon Dioxide and 30% Nitrogen

$C_p$  Specific Heat Capacity at constant pressure,  $\text{J}/(\text{kg}\cdot\text{K})$

$\delta$  Shock thickness, distance between 25% and 75% of the maximum intensity for the leading edge of the plume, cm

$\delta_\nu$  Shock thickness given a velocity  $\nu$ , m

$d$  Diameter of gas species, m

$(\frac{d\nu}{dz})_{max}$  Maximum velocity gradient, m/s

$e$  Electron charge, C

$E_a$  Laser ablation energy, J

$E_p$  Laser pulse energy, J

$E_{ST}$  Sedov-Taylor blast energy, J

$f^*$  Nondimensional fluence: applied fluence relative to the material's vaporization threshold

$F$  Fluence, J/cm<sup>2</sup>

$f$  Focal length, mm

$F_{th}$  Ablation threshold fluence, J/cm<sup>2</sup>

$h^*$  Nondimensional hole depth: hole depth relative to the thermal diffusion length during the laser pulse duration

$h$  Hole depth, m

$h_s$  Heat of Sublimation, kJ/g

$I(z)$  Intensity at depth  $z$ , W/cm<sup>2</sup>

$I_o$  Initial intensity, W/cm<sup>2</sup>

$I_b$  Background intensity, counts

$I_m$  Peak intensity, counts

$\kappa$  Diffusivity, cm<sup>2</sup>/s

$\kappa_0$  Material attenuation coefficient,  $\text{m}^{-1}$

$K$  Thermal Conductivity,  $\text{W}/(\text{m}\cdot\text{K})$

$k_B$  Boltzmann constant

$KE$  Kinetic Energy, eV

$\lambda$  Mean free path,  $\mu\text{m}$

$\lambda_0$  Vacuum wavelength, m

$\lambda_L$  Laser wavelength, m

$l_0$  Length scale, mm

$l_D$  Diffusion length, nm

$l_{depth}$  Penetration depth, m

$l_{Knudsen}$  Knudsen Layer thickness, m

$\mu$  Temperature dependent viscosity,  $\text{kg}/(\text{m}\cdot\text{s})$

$m_e$  Electron mass, kg

$M$  Mach number

$m$  Mass of atom or molecule, kg

$m_a$  Mass ablated from target,  $\mu\text{g}$

$m_1, m_2$  Condensed matter atomic/molecular mass for particle, 1, in a gas, 2, kg

$\nu_1, \nu_2$  Post-shock velocity and Pre-shock velocity, m/s

$N_2$  Nitrogen gas

$n$  Sedov-Taylor dimensionality parameter

$n_c$  Critical plasma density,  $\text{cm}^{-3}$

$n_e$  Electron number density,  $\text{cm}^{-3}$

$P_b$  Pressure of the background gas, Torr

$\rho$  Density,  $\text{g/cm}^3$

$R$  Surface reflectivity

$r_a, r_b$  Condensed matter atomic radius, nm

$S$  Shock strength,  $\text{cm}^{-1}$

$s$  Sedov-Taylor Energy deposition parameter

$s$  Kremer-Müller model temperature exponent in temperature-dependent viscosity

$\tau_0$  Time scale, ns

$\tau_p, t_p$  Laser pulse temporal profile (Full-width at half-max), ns

$t$  Time from peak of the laser pulse, ns or  $\mu\text{s}$

$T$  Temperature, K

$t_\omega$  Thermal diffusion time of a material relative to a length  $\omega$ , ns

$t^*$  Nondimensional pulse duration: pulse duration relative to the thermal diffusion time of the laser spot area

$v_0$  Initial velocity of plume or shock, cm/ $\mu$ s

$\nu_p$  Plasma resonant frequency, MHz

$\omega$  Spot radius (at  $1/e$  point of Gaussian fit to transverse spatial extent) as a function of distance along propagation direction, m

$\omega_0$  Value of  $\omega$  at laser focus along direction of propagation, m

$\xi_n$  Constant dependent on ratio of specific heats

$z_0$  Initial plume position, cm

$z_{25}, z_{75}$  Distance from the target where the leading edge intensity is 25% or 75% of the max intensity

$z$  Material depth for Beer's Law, cm

$z$  Position of emissive plume contact front or shock wave

$z_D$  Shock detachment distance from target, cm

$z_{high}$  Distance to target for Sedov-Taylor high limit, cm

$z_{low}$  Distance to target for Sedov-Taylor low limit, cm

$Z_s$  Stopping distance, cm

$Z(t)$  Distance from target at time  $t$ , cm

# IMPROVEMENTS TO EMISSIVE PLUME AND SHOCK WAVE DIAGNOSTICS AND INTERPRETATION DURING PULSED LASER ABLATION OF GRAPHITE

## I. Introduction

Pulsed laser ablation of various materials has a wide variety of industrial, research, and military applications. Optical diagnostics of pulsed laser ablation plume trajectories are routinely used to determine and characterize ablation parameters such as laser-plume energy coupling, plume stopping distances, kinetic energies, and velocities, and these parameters are essential to most material processing control strategies [1, 2]. These characteristic parameters reflect ablation conditions and are an important piece of the puzzle towards understanding how plume dynamics evolve and relate to laser ablation [2, 3]. However, a challenge with plume diagnostics has been the ability to compare results from different materials across different ablation conditions in order to achieve a unified understanding of the physical processes of laser ablation. This challenge is compounded by the use of imperfect diagnostic techniques to analyze the emissive plume, such as Sedov-Taylor blast energy analysis that was originally created to describe shock wave dynamics [4, 5]. Another related issue is that little literature exists regarding pulsed laser ablation dynamics in varied conditions using a single experimental apparatus, resulting in researchers potentially attributing differences between results to experimental setup differences instead of physical processes. The end result is significant gaps in the knowledge base that inhibit a unified understanding of the ablation processes which influence emissive plume and shock wave plume dynamics. This leads to the purpose of this work: to improve the interpretation of common diagnostic techniques used to characterize pulsed laser ablation, to find simple but universal scaling relationships for comparing ablation dynamics across different target

materials and ablation conditions, and to provide a comprehensive and systematic analysis of emissive plume and shock wave dynamics to fill some of the gaps in the literature.

Graphite was chosen as the target material for this work since it has been less studied in pulsed laser ablation than other materials such as metals or polymers. In addition, pulsed laser ablation of graphite has a wide variety of useful applications, due to its unique thermal and material properties, including production of thin films and nano-materials including diamond-like carbon and silicon carbide carbon nitride composites [6, 7], characterization and testing of hypersonic thermal protection materials [8], and laser battle damage [9, 10].

Deficiencies in the diagnostic comparisons of ablation plumes across varied experimental conditions and target materials are evident. The use of Sedov-Taylor analysis for determining laser-plume coupling is common across laser ablation studies. However, the physical processes influencing laser coupling energies are difficult to interpret and decouple across different environment conditions such background gases, pressures, laser fluence and laser spot size. Reducing the dimensionality of comparisons across materials and conditions would improve the understanding of fundamental laser ablation processes and allow for predictions of effects without having to obtain data for every possible combination of experimental and environmental conditions [11]. In addition, inadequacies in the diagnostics provide an area for improvement. This is evident in the use of emissive plume Sedov-Taylor analysis, which can be greatly influenced by the choice of data sectioning limits. If data points in the plume trajectory for the non-shock region are included in the Sedov-Taylor fitting, the fit coefficients can be affected as the trajectory has diverged from the model assumptions, leading to reduced accuracy of laser-plume coupling energy estimates. Improvements to plume diagnostic parameter interpretation and estimation are key to enabling universal comparisons of plume dynamics between target materials that reveal the physical processes governing laser ablation.

The existing literature for pulsed laser ablation of graphite, and other target materials in

general, is fragmented with little comprehensive or systematic investigations into laser coupling to plume overpressure and how that overpressure drives expansion for both emissive plumes and shock waves. A fairly extensive body of literature exists on pulsed laser ablation of graphite to include ablation with lasers at 248 nm [12–16] and 1064 nm [17–20], as well as studies focusing on spectroscopic analyses of specific plume species such as  $C_2$  and CN molecules [21–24]. However, the prior literature is dominated by characterization of emissive plumes [25–33], and there are no studies that explore both emissive plumes and shock wave dynamics in systematic detail. In addition, most studies limit their focus to a single gas or pressure with very few studies [15, 22, 34] exploring a range of gases, thus providing little overarching insight into the evolving plume and shock wave dynamics for different conditions.

The key research objectives in this work are as follows:

1. Find simple but universal scaling relationships for optical diagnostic parameters such as laser-plume energy coupling for comparing emissive plume ablation dynamics across different target materials and conditions.
  - 1.1 Determine if the laser-plume energy coupling ratio can be scaled using plume stopping distance normalized by mean free path. Compare the energy scaling to other target material data in the literature, such as graphite, aluminum, titanium, barium that have provided Sedov-Taylor coefficients ready for scaling.
  - 1.2 Validate a recently developed method that proposed novel non-dimensional variables for comparing ablation results across disparate materials and experimental conditions [11]. Test with the current graphite data and extend the non-dimensional factor results, which previously did not include graphite as a target material.
  - 1.3 Explore the relationship between shock strength and Mach number to determine

if a normalized shock strength to Mach number curve is universal for different background gases and target materials.

2. Develop a technique using shock detachment for sectioning emissive plume trajectory data for Sedov-Taylor analysis to obtain a more meaningful interpretation of the laser energy deposited into the plume.

1.1 Determine shock detachment distances using emissive plume and shock wave imagery. Utilize detachment-limited trajectories to improve Sedov-Taylor data sectioning for laser-plume energy coupling estimates.

1.2 Determine key propagation parameters for the emissive plume including velocities and kinetic energies, and compare plume and shock wave laser-plume energy coupling with Sedov-Taylor blast theory analysis.

3. Conduct a systematic analysis of graphite emissive plume and shock wave morphology across a range of experimental conditions.

1.1 Compare effects of rectangular and circular laser spot geometry on plume and shock morphology including dependence on pressure and background gas.

1.2 Explore plume and shock morphology viewed in two angles for the rectangular laser spot. Correlate emissive plume structure to shock wave imagery.

1.3 Compare shock wave Sedov-Taylor dimensionality to a visual analysis of the shock wave curvature in the schlieren imagery.

The format of this dissertation is as follows: Chapter 2 provides an overview of the various process regimes in pulsed laser ablation including laser-target interactions, laser-plume interactions, plume and shock wave propagation, and a brief overview of the techniques utilized in this work. A review of relevant literature is presented. Detailed literature reviews of relevant prior work are also presented within each chapter as necessary.

Chapter 3 presents a study of emissive plume dynamics using fast-gated imagery to improve the interpretation of optical diagnostic parameters for plume trajectory characterization and laser-plume energy coupling efficiency. A new scaling method is developed and validated that enables comparisons of laser-plume energy coupling between different target materials ablated under varying environmental and system conditions. In addition, an analysis is presented leveraging the emissive plume to explore shock thickness and shock strength. Chapter 3 was published as a paper in *Optical Engineering* in May 2021 [35].

Chapter 4 details the dynamics of the ablation shock wave and emissive plume using fast-gated and schlieren imagery with a focus on characterizing shock detachment in order to enhance data sectioning for Sedov-Taylor analysis. Shock wave and emissive plume trajectories are characterized with Sedov-Taylor analysis. The Sedov-Taylor energies for the emissive plume are shown to be significantly improved by using shock detachment to inform data sectioning, resulting in more accurate laser-plume energy estimates. Chapter 4 was submitted to the peer-reviewed journal, *Applied Physics A*, in July 2021.

Chapter 5 documents a study examining morphology of emissive plumes and corresponding shock waves during pulsed laser ablation of graphite comparing rectangular and circular laser spots. Plume and shock morphology are discussed including examination of temporal propagation, shock curvature, and the effect of viewing angle on plume and shock appearance. Chapter 5 has been prepared for submission to a peer-reviewed journal.

Chapter 6 provides the conclusion to the dissertation and discusses suggested future research that could further enhance this area of work. Finally, while Chapters 3–5 have been or will be published with co-authors, Major Timothy Calver is the primary author and principal investigator for all the works.

## II. Background

### 2.1 Laser Ablation Process Regimes

Research in pulsed laser ablation of materials focuses primarily on three main physical process regimes that include interactions between the laser and the target material, interactions between the laser and the plume after the material is ablated from a surface, and the dynamics of the plume of ablated materials as it propagates away from the target through vacuum or a background gas.

#### 2.1.1 Laser-Target Interaction

In pulsed laser ablation of a solid target, photons from the laser interact with the material absorbing into and reflecting off the material. The attenuation of light in a material is described by the Beer-Lambert law given as:

$$I(z) = I_o(1 - R)e^{-\alpha z} \quad (1)$$

where  $I(z)$  is the laser intensity at a penetrative depth  $z$ ,  $R$  is the material reflectivity,  $I_o$  is the laser intensity at the material surface, and  $\alpha$  is the absorption coefficient for the material [36]. The absorption coefficient is given by:

$$\alpha = \frac{4\pi\kappa_0}{\lambda_0} \quad (2)$$

where  $\lambda_0$  is the vacuum wavelength and  $\kappa_0$  is the attenuation coefficient of the material [36]. The attenuation coefficient of a material is highly dependent upon the incident photon wavelength [37]. The optical penetration depth is the distance into a material for which the intensity of incident electromagnetic radiation drops to 1/e of the original intensity. The optical penetration depth can be found by taking the inverse of the absorption coefficient,

yielding:

$$l_{depth} = \frac{\lambda_0}{4\pi\kappa_0}. \quad (3)$$

As a result, the optical penetration depth,  $l_{depth}$ , is dependent upon the laser wavelength and the target material's properties [36]. Absorption of laser photons is a key process of pulse laser ablation since the absorption directly influences the transfer of energy into the material through two processes: photoionization and phonon transfer. It is possible for laser photon interaction to liberate electrons from an atom through photoionization. This effect can occur with high intensity lasers when a laser photon interacts with and ionizes an atom, if the photon has sufficient energy to cross the ionization threshold [38]. It is possible for multi-photon photoionization to occur as well, with two or more photons interacting with an atom. However, photoionization requires high photon energies to occur efficiently, and the reaction cross section for multiphoton photoionization decreases dramatically for each additional photon that interacts in a single event [39].

The most common energy transfer process in a target material is through phonon interactions which appear as heat in the material. When laser photons are absorbed into a material, the energy of the photon is transferred to phonons within the material which increase lattice vibrations leading to heating. As the heat in a material increases, eventually it will reach a melting point at which the material will begin to change phase from solid to liquid. The melted material will absorb more energy from the laser photons, eventually reaching the material vaporization point and the material will transition to a vapor phase. During the vaporization of material from the liquid surface, the temperature of the vapor particles will be determined by the Knudsen layer. The Knudsen layer is a region just above the liquid-gas interface point where the plume begins to form and where the laser can interact with the plume species. The Knudsen layer thickness is described by:

$$l_{Knudsen} = \frac{k_B T}{\pi d^2 P_b} \quad (4)$$

where  $k_B$  is the Boltzmann constant,  $T$  is the temperature,  $d$  is the diameter of the gas species, and  $P_b$  is the background gas pressure [40]. Depending upon the material and laser characteristics, it is possible for the laser to induce a direct phase change from solid to vapor as well. For example, aluminum and titanium will melt and then vaporize as more energy is deposited into the material by the laser. However, graphite has no melting point under the conditions explored in this work, and will transition directly from a solid to a vapor [41, 42]. As a result of the laser interaction processes during ablation, the primary process for ablating material into a plume will be thermal effects induced in the material by the laser irradiation.

Although thermal processes account for much of the material ablated from a target, evidence is mentioned in the literature for additional ablation due to non-thermal processes including phase explosion and Coulomb explosion. Phase explosion is a process that occurs in the nanosecond laser pulse duration regime when the temperature of a material approaches the critical temperature which results in a liquid-gas meta-phase that explosively boils off the material, enhancing the total ablation volume [43]. The laser fluence threshold for phase explosion in graphite has been shown to be 3.75 to 4.5 J/cm<sup>2</sup> in air [19, 44], while a recent study found that the mass ablated from phase explosion was negligible at fluences less than 25 J/cm<sup>2</sup> [45]. Coulomb explosion, also known as electronic ablation, is a process that occurs in cases where the laser pulse duration is less than the material thermal relaxation time [2]. In the Coulomb explosion process, outer valence electrons can be removed from the target atoms by the incident laser pulse, leaving the affected atoms with a positive charge. The Coulomb repulsion force then explosively propels the atoms away from the surface and from each other. Coulomb explosion in graphite is dominant in the picosecond and femtosecond laser pulse width regimes due to the smaller timescales compared to the thermal relaxation time [46, 47].

### 2.1.2 Laser-Plume Interaction

Once a portion of the target material has vaporized from thermal effects and other laser-target processes, the constituent species of particles in the plume can interact with the incident laser if it is still lasing. Phonon heating can occur with clusters of material that have ablated off target. Another process for laser-plume interaction is photoionization, which can occur between the laser and species of the plume containing bound electrons through the same process as described above. Laser photons can excite and ionize plume constituents, freeing electrons into the plume. The dominant process of laser-plume interaction is the inverse-Bremsstrahlung process where free electrons in the ablation plume couple with the field of the laser by absorbing photons and then experience acceleration from the energy that is transferred to them [48]. The accelerated electrons can then experience collisions with neutral or ionic species in the plume resulting in excitation, or ionization if enough energy is transferred in the collision. The energy transfer process of inverse-Bremsstrahlung is the most efficient when the laser frequency is near the plasma frequency, given by

$$\nu_p = (4\pi n_e e^2 / m_e)^{1/2} \quad (5)$$

where  $\nu_p$  is the resonant plasma frequency,  $n_e$  is the electron number density,  $e$  is the electron charge, and  $m_e$  is the electron mass [49]. The plasma can continue to absorb energy from the laser until the plasma density is greater than the critical density. The plasma critical density is given by:

$$n_c = \frac{\pi m_e c^2}{e^2 \lambda_L^2} \quad (6)$$

where  $n_c$  is the critical plasma density,  $m_e$  is the electron mass,  $c$  is the speed of light,  $e$  is the electron charge, and  $\lambda_L$  is the laser wavelength [50]. Once the plasma critical density is exceeded, the laser cannot propagate through the plasma and will scatter or reflect off

the plasma surface. The plume will become optically thick to the laser and will effectively shield the target from further material ablation. Plume absorption and scattering processes both result in plume shielding that decreases ablation from the target. The coupling of the laser energy into the ablation plume via inverse-Bremsstrahlung and photoionization results in high temperatures, velocities and Mach numbers for plume species excited through these processes. Once the laser pulse duration has ended, the plume enters the plume propagation regime.

### **2.1.3 Plume Propagation**

The overall dynamics of the plume expansion are not completely understood as multiple complex processes are involved between the start of a laser ablation event and the time the plume stops in the background gas if present. Plume dynamics can be explored using intensified charge-coupled device (ICCD) imagery or spectroscopic techniques to characterize the plume expansion. Plume trajectories are created by plotting the position of the shock front for each time step allowing for the analysis of the plume shock front propagation over time and distance. In a vacuum, the plume is considered to be collision-free and adiabatic [51]. The dynamics of an ablation plume are also highly dependent on the background gas and pressure. Plume expansion is typically characterized into three distinct regions including the free expansion region, the blast wave region typically characterized by the Sedov-Taylor equation, and the drag region characterized by the drag model [2].

At very early times within the plume expansion, ablated material has not had enough time to interact with any background gas. As a result, a free expansion model can be used to characterize the expansion of the plume for both a vacuum case and for early plume expansion times in a background gas [52]. In the free expansion region, the plume constituents will experience constant velocities. It is important to note that in ablation into a vacuum without a background gas, intra-plume collisions still occur due to some plume

species having faster initial velocities than others [53]. However, vacuum cases are still characterized with the free expansion model in the literature. The plume near the end of the free expansion region acts as a mechanical piston which compresses the background gas, leading to the formation of a shock front [54]. Since the plume is typically expanding with velocities greater than the local sound speed of the background gas, a shock wave is formed. The formation of the shock front is typically considered the boundary between the free expansion region and the shock region where the shock front has developed.

At the shock front, collisions between the plume species and the gas result in increased emission as faster moving material is collisionally excited, emits photons and then slows due to the loss of energy. Slower moving material behind the contact front then catches up, collides with the background gas, and then also excites, emits photons, and slows. Plume emission is primarily the result of translational-to-electronic energy (T-E) excitation. The plume dynamics in middle region in which the shock front is well-developed can be characterized using blast wave theory with the Sedov-Taylor model [4, 5]. The Sedov-Taylor model is valid when the mass displaced by the shock front is larger than the mass inside the plume and when the pressure behind the shock front is still very large compared to the background gas pressure [55]. The Sedov-Taylor model is useful for estimating the amount of energy from the ablation laser that couples into the plume during the explosive ablation event. The Sedov-Taylor model is described in more detail in Chapter 3 and Chapter 4.

The final region of an ablation plume expansion is dominated by drag as the expanding plume encounters more collisions with the background gas and slows, lacking the energy to continue to plow through the gas. The plume of vaporized, ablated material from the laser interactions expands outwards into the background gas and is eventually slows to a stopping distance. The stopping distance of the plume is heavily dependent on the pressure of the background gas and decreases as pressure is increased [52]. The drag model is useful for estimating the initial expansion velocity of the plume [52]. Details and application of

the drag model are given in Chapter 3.

A common assumption in pulsed laser ablation literature is that the emissive contact front, at the leading edge of the plume, is located at or very near to the shock wave for a significant portion of the plume expansion, until the shock wave detaches from the plume as the plume slows due to collisions with the background gas [2]. The emissive plume contact front ceases to propagate in a shock-like trajectory after this point. Shock detachment is the point in the propagation where there is not enough energy left in plume to reach the Translation-Electronic energy cross section for excitation. Since the emissive plume contact front is much easier to experimentally locate than the shock wave, the emissive contact front location is used as a surrogate for the shock wave location, which requires more complexity to capture experimentally. As a result, it is more common for researchers to study the plume emissive contact front using optical emission imaging (see Section 2.3).

## **2.2 Optical Plume Imaging Techniques**

### **2.2.1 Fast Optical Emission Imaging**

Fast optical emission imaging using ICCD cameras can be used to conduct time-resolved spectroscopy and morphological examination of plume constituents [56]. ICCD camera systems use an intensifier to amplify the faint signals from emissive species, allowing them to be detectable. Some intensifiers can be gated down to picosecond time scales for ultrafast imaging [57]. A benefit of fast ICCD imaging is that the plume dynamics for kinetics and plume morphology can be captured in two-dimensional images. This allows for the imaging of the full plume at various times during the plume's propagation from the target and through the background gas or vacuum. Emissions from the excited material are captured with the camera at different time delays, enabling the capture of a plume's propagation as a function of time and allowing for the creation of plume trajectories that can be used to determine propagation speeds, stopping distances, laser-plume coupling energies, and other

plume dynamics features using various plume expansion modeling. ICCD systems allow for the visualization of shock wave formation and propagation during the ablation event when utilized with a shock imaging apparatus such as schlieren or shadowgraph optical systems.

### **2.2.2 Schlieren Imaging**

Schlieren photography or imaging, named for the German word, “schliere,” which translates to “streak,” is an optical technique for flow visualization of density changes in transparent media such as a gas or fluid [58]. Schlieren imaging is useful for pulsed laser ablation diagnostics as it allows for the visualization of the invisible ablation shock wave. Coupled with a fast-gated ICCD camera, schlieren imaging can capture the propagation dynamics of the ablation shock wave, allowing for the direct comparison of emissive plume dynamics to shock wave dynamics during a pulsed laser ablation event. Schlieren imaging exploits the fact that density differences in a gas or fluid result in a gradient in the index of refraction. Light passing through the index gradient is then deflected from its original path. In schlieren imaging, the amount of refraction of the light is proportional to the first derivative of the optical density field. Schlieren imagery is also useful in that it results in a focused optical image, allowing for the schlieren target area to form a 1:1 image of the object in question [58]. A schlieren imaging apparatus utilize mirrors or lenses to direct the light from a light source through a target area and then onto an imager, which can be a screen or a camera system.

Figure 1 shows a schematic of the schlieren setup used in this dissertation, called a dual-field-lens system, although other configurations exist [58]. For this setup, a schlieren light source is passed through a condenser lens and is focused onto a pinhole. The pinhole acts as a point source and the light exiting the pinhole enters a collimating lens, typically a cemented-asphere lens to reduce spherical aberration. The collimated light rays travel

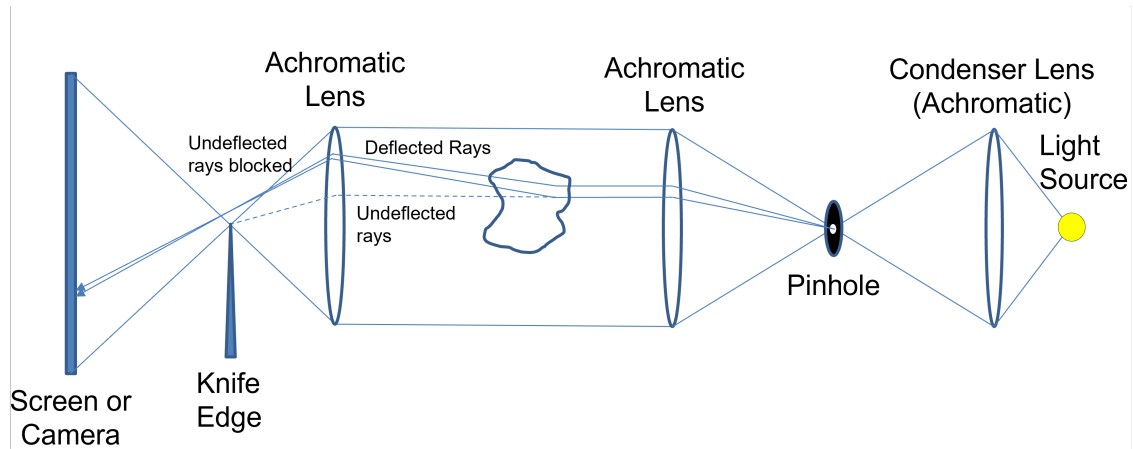


**Figure 1:** Schematic of a dual-field-lens schlieren imaging apparatus.

parallel to each other through the test cell which contains the object of interest and are deflected when they encounter a density gradient, such as occurs near a shock wave. The light is then passed to another lens and focused onto a knife edge, typically a razor blade, or a graded filter. The knife edge acts as a spatial frequency filter, blocking a portion of the light which has not been deflected. The deflected light passes above the knife edge and is imaged onto a screen or camera, resulting in the appearance of a dark schlieren object. The knife edge can be positioned vertically or horizontally, resulting in the visualization of either the vertical components of the schlieren object or the horizontal components respectively.

Typical schlieren light sources include monochromatic lasers and quasi-monochromatic or polychromatic white light emitting diodes (LED). For a white light LED source, all the lenses in the system need to be achromatic to avoid differential focusing of the extended wavelengths which will smear out the schlieren image. Laser sources are typically used in conjunction with bandpass filters at the imaging system in order to filter out any unwanted light from bright sources such as the emissive plume, allowing the schlieren object to be clearly visible. The dual-field-lens system constructed for this work allows for the imaging of both the emissive plume when the schlieren light source is turned off, and the corresponding ablation shock wave when the light source is turned on. In this way, plume and

shock wave imagery can be acquired and their propagation dynamics directly compared.

## 2.3 Previous Work

### 2.3.1 Emissive Plume Dynamics, Shock Strength, and Shock Thickness

Graphite ablation studies, and pulsed laser ablation studies of other materials, have largely focused on the formation and dynamics of neutral and ionized atomic and molecular species such as carbon [12, 17, 21, 24–27, 29, 30, 59]. Claeysens et. al. observed emission from neutral and ionized carbon only for nanosecond pulse durations [59]. In 2018, Yousfi et. al. observed  $C_2$  formation in a reflected shock and CH visible emission with methane and argon background gas [21]. More recently, Diaz and Hahn investigated the effects of background gas type on the formation of atomic and molecular species in graphite ablation plumes using time-resolved emission spectroscopy [60]. Several studies have investigated the effects of background gas pressure on graphite plume expansion dynamics ranging from vacuum to 300 Torr [12, 17, 24, 29, 30, 61]. The most recent graphite plume ablation studies were conducted by Nica et. al., who studied the dynamics of ions in graphite ablation plumes [62, 63]. The intense focus on emissive plume dynamics has been mirrored in the greater pulsed laser ablation community for other materials.

In addition to spectroscopic studies of plume species, studies have investigated graphite plume expansion dynamics using Sedov-Taylor modeling to estimate laser-plume energy coupling [17, 21, 24, 25, 61, 64]. Singh studied expansion dynamics of graphite in 760 Torr nitrogen with emission imaging and shadowgraphy, finding that the initial Sedov-Taylor energy to be 40% of the laser pulse energy, [64].

The characterization of shocks in a gas, particularly shock thickness, is largely limited to older shock tube studies where the Mach number,  $M$ , is typically less than 10 and the background pressure is high compared to typical laser ablation conditions [65–70]. Standard models for the influence of temperature dependent viscosity on shock thickness can

lead to physically unreasonable results when extrapolated to higher Mach numbers [70], such as those seen in laser ablation, and the prediction of increased shock thickness for  $M > 3$  is weakly validated only for a small range of flow speeds [68, 69]. Only two prior studies in the overall literature of pulsed laser ablation literature have specifically explored plume shock thickness and shock strength for pulsed laser ablation [52, 71]. Phelps et. al. studied pulsed shock thickness and strength of barium plumes in an oxygen background gas using emissive plume imagery [52]. George et. al. explored shock velocity and shock strength during the ablation of lithium fluoride-carbon targets in oxygen, argon, and helium gases using emissive plume imagery [71].

### **2.3.2 Shock Wave Propagation and Shock Detachment**

Shock wave propagation is commonly indirectly studied by characterizing emissive plume contact front propagation trajectories with the Sedov-Taylor blast model along with the assumption that the emissive contact front is co-located with the shock wave. The bulk of the emission in the emissive contact front of the plume is assumed to have resulted from the passing of the shock wave through the plume material, resulting in enhanced emission [17, 24, 61, 64]. In emissive plume contact front characterization, the Sedov-Taylor limits are often used to partition fitting, with the low limit used to bound the early propagation and the high limit used to bound the later propagation [72]. However, the Sedov-Taylor high limit is often many lengths further than the plume stopping distance [4, 5, 72]. The point where the emissive plume begins to slow in comparison to the shock wave is the shock detachment point [73, 74]. After the shock detachment occurs, the emissive contact front trajectory no longer follows a blast-like trajectory, and the Sedov-Taylor model is no longer sufficient to describe the propagation after this point. As a result, Sedov-Taylor fits to the emissive contact front beyond the shock detachment point will result in poorer estimates of the Sedov-Taylor blast energy and resulting laser-plume coupling efficiency.

Although a several studies have explored the shock wave produced during pulsed laser ablation in a limited fashion [64, 75], very few studies have focused on the effects of shock wave propagation in conjunction with the emissive plume in detail. In 1999, Kokai et. al. explored graphite ablation in ambient argon with shadowgraphy, fast imaging, and emission spectroscopy, focusing on darkened region in the interior of the plume [75]. In 2013, Singh, Gupta, and Thareja investigated plume and some shock wave dynamics for graphite ablation in ambient nitrogen using fast imaging, emission spectroscopy, and an interferometer to characterize the location of  $C_2$  and CN species within the plume [64]. Neither of these studies characterized detachment of the shock from the emissive plume. No prior graphite studies were found that examine the dynamics of both the emissive plume contact front and the shock front in detail, and no studies that examine shock detachment and its effects on Sedov-Taylor modeling of emissive plumes.

### **2.3.3 Plume and Shock Morphology**

There has been some prior exploration of the laser ablation shock wave in graphite [64, 75, 76], although most studies focus on emissive plume structure. Kokai et. al. explored laser ablation of graphite in argon with shadowgraphy, emission imaging, and emission spectroscopy, focusing on characterizing the formation carbon clusters near the target surface [75]. Singh, Gupta, and Thareja explored graphite ablation using fast imaging, emission spectroscopy, shadowgraphy, and interferometry [64]. They found that velocity estimates for emissive imaging were comparable to shadowgraphy estimates, and determined that the shock wave expansion was spherical from the shadowgraphy imagery. Ursu et. al. characterized a specific plasma plume morphology [25–27]. In 2021, Eliceiri and Grigoriopoulos used shadowgraphy, laser probing, and spectroscopy to explore graphite plume plasma shielding and density [76].

Plume morphology studies have been performed for other target materials including

metals such as copper [77] and aluminum [78], or to study parameters such as laser spot size [79] or the effects of background gas [80]. However most studies in the overall laser ablation literature rely only on fast imaging and optical emission spectroscopy to explore the dynamics of the emissive plume. Very few studies have been conducted for pulsed laser ablation of graphite or other target materials that directly compare the shock wave curvature and morphology to the emissive plume morphology using multiple laser footprint geometries. For graphite in particular, no prior studies have been found that examine the morphology of both the emissive plume and the shock wave in comprehensive detail for multiple gases and pressures.

### III. Shock front behavior during pulsed laser ablation of graphite

Pulsed laser ablation of pyrolytic graphite with a  $4 \text{ J/cm}^2$  KrF laser in backgrounds of air, argon, nitrogen, and helium at pressures up to 10 Torr was performed to find and validate new scaling relationships for common ablation diagnostic parameters. Optical emission imaging with a 2 ns gated ICCD camera was used to determine shock front positions and plume trajectories for characterization by free expansion, Sedov-Taylor blast and drag models. The plume expands with initial Mach numbers of  $M \sim 48$ , decreasing to  $M \sim 10$  as the emission becomes too weak to detect. The plumes begin with a planar shock front and thickness of a few mean free paths, but evolve to higher dimensionality,  $n$ , depending on pressure and mass of the background gas. The Sedov-Taylor energy released in the sudden ablation is typically 33% the laser pulse energy. Blast energy and plume dimensionality are correlated with stopping distances which are typically greater than  $10^3$  mean free paths. High estimates for the mass ablated (0.36–0.76  $\mu\text{g/pulse}$ ) and hole depth ( $\sim 37\text{--}77$  nm) are inferred from the emissive plume kinetic energy relative to laser pulse energy. The inferred hole depth ranges from 14–28 percent of the thermal diffusion length as the pressure increases from 1 to 10 Torr for these conditions where the fluence is just above twice the ablation threshold. A new scaling method was proposed and validated, enabling comparisons of laser-plume energy coupling between different target materials ablated under varying environmental and system conditions. The data analyzed in this study was acquired at the end of Dr. William Bauer’s dissertation research in 2017 [54].

#### 3.1 Introduction

Pulsed laser ablation (PLA) of graphite materials has a wide variety of useful applications including thin film and nano-material production including diamond-like carbon and carbon nitride films [2, 43], characterization of hypersonic thermal protection materials

[8], and defining laser weapon effects [9, 10]. Optical characterization of plume dynamics including trajectories, stopping distances, and kinetic energies of atomic and molecular species are essential to most material processing control strategies [1, 2, 81] and reflect ablation conditions [2, 3]. Sublimation of carbon, silicon carbide and other materials provides thermal protection for aerospace vehicles at high speed, leading to highly ionized plumes and strong emission [8, 82, 83]. The vulnerability of carbon composites to laser weapons systems also requires fundamental studies of heating and oxidation [41, 84].

The production of thin films by pulsed ablation of graphite often employs pulse durations of 10 - 100 ns in the ultraviolet (UV). More recently, ablation with shorter pulses and longer wavelengths have been studied [85–87]. Laser fluences near the ablation threshold ( $\sim 1.8 \text{ J/cm}^2$  for graphite) are often desirable for materials processing to avoid the high ion content and the long plume stopping distances observed at high fluence ( $\sim 1 \text{ kJ/cm}^2$ ) [61, 88–90].

Prior graphite ablation studies have largely focused on the formation and dynamics of neutral and ionized atomic and molecular carbon [12, 17, 21, 24–27, 29, 30, 59]. Yousfi et. al. recently observed  $\text{C}_2$  formation in a slow, reflected shock and CH visible emission with methane and argon background gases using time of flight spectrometry [21]. Claeysens et. al. observed emission from neutral and ionized carbon only for nanosecond pulse durations, with emission dominated by molecular ions for shorter pulses [59]. Al-Shboul et. al. compared the effects of femtosecond and nanosecond ablation of graphite, indicating the role of three-body recombination in the production of  $\text{C}_2$  emission [30]. Diaz and Hahn investigated the effects of background gas type on the formation of atomic and molecular species in graphite ablation plumes using time-resolved emission spectroscopy, finding that CN molecules exhibit two emission intensity local maxima as opposed to an exponential decay [60]. Several studies have investigated the effects of background gas pressure on graphite plume expansion dynamics ranging from vacuum to 300 Torr [12, 17, 24, 29, 30,

61]. Ursu et. al. characterized a specific plasma plume morphology [25–27]. The most recent graphite ablation studies were conducted by Nica et. al., who studied the dynamics of ions in graphite ablation plumes [62, 63].

A few studies have investigated plume shock front dynamics using blast wave expansion (Sedov-Taylor) modeling [17, 24, 61, 64]. Others have used blast modeling in nitrogen backgrounds to characterize ionized atomic nitrogen and CN [21, 25]. Singh studied expansion dynamics of graphite in 760 Torr nitrogen with emission imaging and shadowgraphy, finding that the initial Sedov-Taylor energy to be 40% of the laser pulse energy, [64] confirming the current preliminary result [91, 92].

Pulsed laser ablation offers an opportunity to study shock propagation under extreme conditions. Shock propagation within the solid target has been studied primarily by monitoring the defects of rear surfaces of thin films [93, 94]. These shocks are produced from the rapidly expanding plume interacting with the target surface. Through Thin Film Ablation (TTFA) is effective in the production of nanoparticles and also depends on shock propagation in the condensed phase [95]. Pulsed ablation in thin liquid films produces shock waves and cavitation bubbles [96]. The liquid film constrains the plasma plume expansion and produces stronger gas shocks. The more generalized characterization of shocks in the gas phase, particularly shock thickness, is largely limited to older shock tube studies where the Mach number ( $M$ ) is typically less than 6 and the background pressure is high [65–70]. Indeed, standard models for the influence of temperature dependent viscosity on shock thickness can lead to physically unreasonable results when extrapolated to higher Mach numbers [70]. Furthermore, the prediction of increased shock thickness for  $M > 3$  is weakly validated only for a small range of flow speeds [68, 69]. Pulsed laser ablation offers high Mach,  $M > 50$ , in evolving, three-dimensional flows. Only two prior studies of PLA plume shock thickness have been conducted [52, 71].

This work focuses on the PLA of graphite, comparing the experimental results to prior

studies of carbon, metal, superconductor, and semiconductor targets. Free expansion, drag, and Sedov-Taylor blast models are used to quantify the ablation plume dynamics. Non-dimensional hole depths are estimated from plume dynamics and compared with metals and semiconductors [11]. A correlation between blast energy and plume dimensionality with stopping distances is developed using the mean free path in the unshocked gas. An exploration of the dependence of shock thickness and shock strength on Mach number and gas pressure is compared with prior studies of YBCO and C-LiF [52, 71]. This research is part of a larger study focusing on the characterization of spatial and temporal dynamics of continuous wave and pulsed laser effects on graphite and carbon fiber targets [41, 84, 97].

### 3.2 Apparatus and Methodology

A Lambda Physik LPX 305 pulsed KrF laser ( $\lambda = 248$  nm) with a 1 Hz repetition rate was used to deliver an average energy of 170 mJ, and up to 180 mJ, per pulse onto a graphite target in a vacuum chamber backfilled with various gases and pressures as shown in Fig. 2. The average energy of 170 mJ is used in the analysis that follows. The laser energy at the target was measured using a Coherent LMP10I detector positioned inside the target chamber. The spot size of the laser on the target was approximately a 9 by 0.5 mm rectangle. The laser pulse has a full width half max of 25 ns and a rise time of 5 ns, yielding an intensity of  $151 \text{ MW/cm}^2$  and fluence of  $4 \text{ J/cm}^2$ . The plume propagates normal to the target in the z-direction with a Princeton Instruments PIMAX I gated intensified charged-coupled device (ICCD) camera recording the emissive plume in the xz-plane as shown in Fig. 3. ICCD imagery were observed with a series of band pass filters: 375 nm (CN), 394 nm ( $\text{C}^+$ ), 520 nm ( $\text{C}_2$ ), 760 nm (Ar) and 830 nm (C). Filter bandwidths varied from 8.9–10.8 nm. Spectrally integrated images without filters were also obtained.

The laser was focused onto the target inside a 25.4 cm vacuum chamber. A 300 mm focal length plano-convex fused silica lens was used to focus the beam onto the target at an

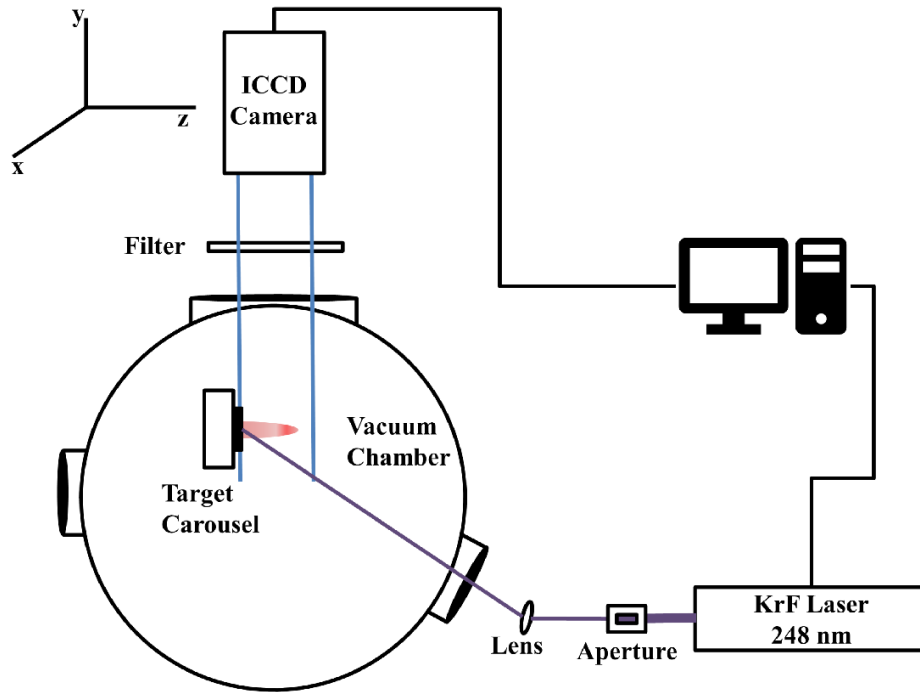


**Figure 2:** Experimental apparatus includes a vacuum chamber containing a sample target carousel, vertically mounted PIMAX I ICCD camera, and ports for other diagnostic equipment. The target is ablated using a KrF pulsed laser source ( $\lambda = 248$  nm, 25 ns pulse width, average energy 170 mJ per pulse at target).

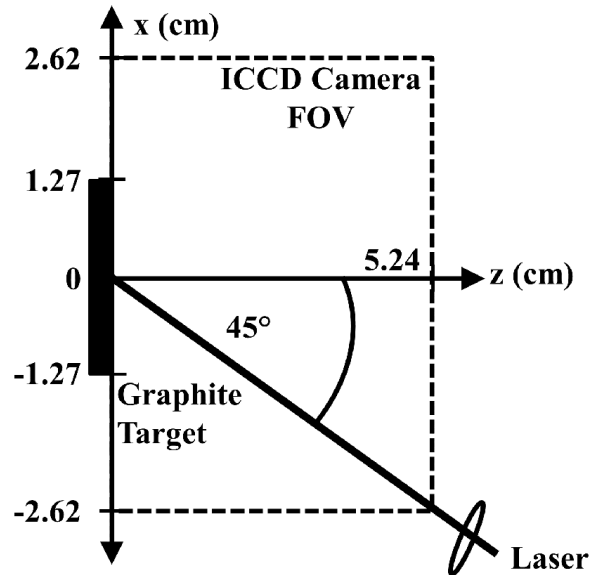


**Figure 3:** ICCD camera field of view. The ICCD camera images the xz-plane, capturing the plume's propagation from the target to a distance 5.24 cm from the target.

angle of incidence of 45 degrees to the target normal. The targets were 25.4 mm diameter by 6.3 mm thickness pyrolytic graphite sputtering target discs (99.999% C) sourced from the Graphite Store with properties provided in Table 1. A 6-target carousel was used to hold the targets and rotated at 10 rpm (z-axis) to minimize cratering on the target surface. The chamber was evacuated to a pressure of  $10^{-6}$  Torr with a turbomolecular pump and then backfilled to either 1 Torr or 10 Torr of 99.999% nitrogen, argon, helium, air, or vacuum at  $T = 298$  K. A Varian 572 ionization gauge was used for near-vacuum monitoring and an MKS model 626 capacitance manometer with a 1000 Torr range was used for higher pressures.

**Table 1:** Thermodynamic and transport properties of pyrolytic graphite samples.

Property	Value	Ref.
Density, $\rho$ (g/cm <sup>3</sup> )	2.2	[98]
Thermal Conductivity, $K$ (W/m·K) (across layers)	3.5	[98]
Specific Heat, $C_p$ (J/kg·K) ( $T = 3500$ K)	2135	[99]
Sublimation Temperature, $T$ (K)	3923	[100]
Heat of Sublimation, $h_s$ (kJ/g)	61.3	[100]
Diffusivity, $\kappa$ (cm <sup>2</sup> /s)	0.0075	calculated
Diffusion length, $l_D$ (nm)	273	calculated
Ablation Threshold Fluence, $F_{th}$ (J/cm <sup>2</sup> )	1.84	calculated

A Princeton Instruments PIMAX I with a 512 x 512 Gen III ICCD camera with a Nikon AF Nikkor 60 mm micro f/2.8 lens was used to capture fast imagery of the plume from above. The quantum efficiency of the 16-bit camera is higher than 20% from 410 to 890 nm, with a peak efficiency of approximately 40% near 700 nm. Saturation occurs at 65,536 counts with a dark signal of 68 counts. The field of view of the lens was 5.24 by 5.24 cm with 0.102 mm per ICCD pixel. The camera was gated with delays of up to 11.5  $\mu$ s after the laser shot and gate widths (integration time) from 2 to 150 ns. For each run, 100 shots were taken with nonlinearly varying gate widths and delays having 2 ns widths at the start of the collection and 150 ns widths at the end of the collection to improve signal to

noise when the plume emission significantly dimmed as it propagated away from the target surface. Four identical runs were collected and the images at each time step were averaged together to account for shot-to-shot variations. The camera was triggered using a signal from the laser electronics. For initial velocities of 2 cm/ $\mu$ s, a 2 ns integration time yields a maximum of 40  $\mu$ m motion during image integration corresponding to 0.39 pixels. At late plume propagation times where the plume speed is reduced, a 100 ns gate width typically corresponds with a maximum motion of less than 3.5 pixels, or about 0.357 mm. Images exhibited < 5% pulse-to-pulse laser flicker and < 10 ns pulse-to-pulse laser timing jitter. Shot-to-shot variation in laser pulse energy was < 1.5%.

### 3.3 Results

#### 3.3.1 Plume Imagery and Shock Front Propagation Speeds

A typical plume image with no bandpass filter at a delay of 369 ns for an air background pressure of 10 Torr is shown as an intensity contour plot in Fig. 4. The dimension of the plume parallel to the target surface is 8.3 mm, only slightly smaller than the 9 mm laser footprint. The leading edge of the plume is located at 0.354 cm, corresponding to a speed of 0.46 cm/ $\mu$ s. Most of the emission occurs near the shock front, with minimal emission from the interior of the plume. In earlier frames, the plume transverse dimension is 8.1 mm with an initial speed of 1.44 cm/ $\mu$ s. The speed of sound in the background air is 0.0346 cm/ $\mu$ s, yielding an initial Mach number of  $M \sim 42$  slowing to  $M \sim 7$  in Fig. 4. At later frames,  $t > 1 \mu$ s, the emissive plume comes to a stop at 0.5 cm, with a component of the emissive plume rebounding off the gas and reflecting backwards to the target surface. The mean free path in air at 10 Torr is  $\sim 5 \mu$ m (see Eq. 22 in Sec. 3.4.4), suggesting  $\sim 10^4$  collisions to stop the emissive plume. Two primary factors influence the stopping distance: (1) the fraction of plume kinetic energy converted to atom electronic excitation (Translational to Electronic) per collision, and (2) the fraction of the kinetic energy distribution engaged in

the shock front (the size of the velocity group in the time-of-flight spectra in the leading edge of the emissive plume).

The shock front location is identified in Fig. 5 where a 5-pixel row average of the emission intensity is plotted along the center line of the plume. The leading edge of the emission is identified where the intensity rises to 50% of the peak at  $z = 0.35$  cm. The shock front and this luminous contact front are likely coincident for most of the plume propagation, with separation generally occurring at  $t < 1 \mu\text{s}$ , as discussed below. The shock is moderately strong in Fig. 5, with a rapid rise in intensity at the leading edge. The thickness of the emissive plume shock front is defined as  $\delta$ , the distance between 25% and 75% of the maximum intensity for the leading edge of the plume. This measured thickness is influenced by instrumental limitations including pixel size and plume curvature along the line of sight, the collisional mechanism for producing atomic and molecular emission, and physical considerations such as the mean free path and viscosity, as discussed further below.

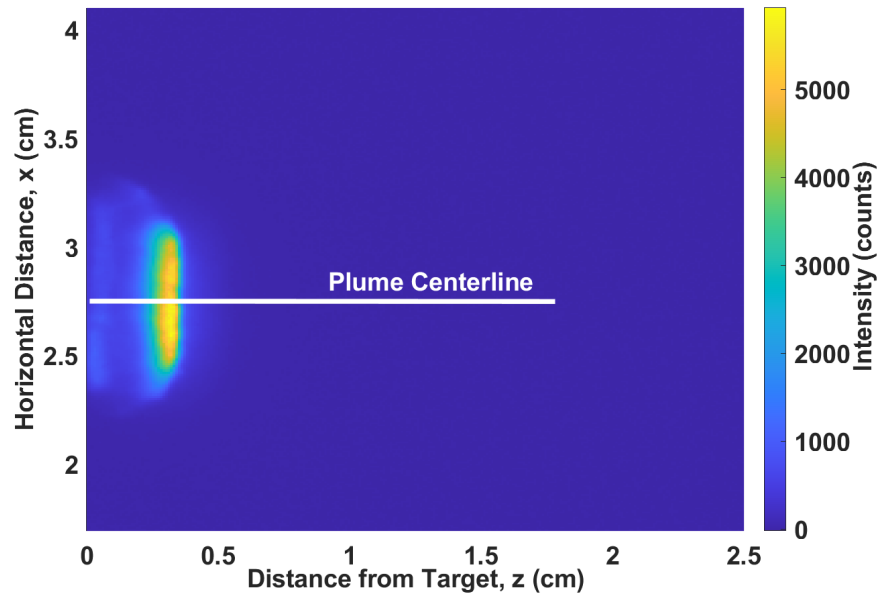


**Figure 4:** Graphite ablation plume ICCD image with 369 ns gate delay in air at 10 Torr with no spectral filter.

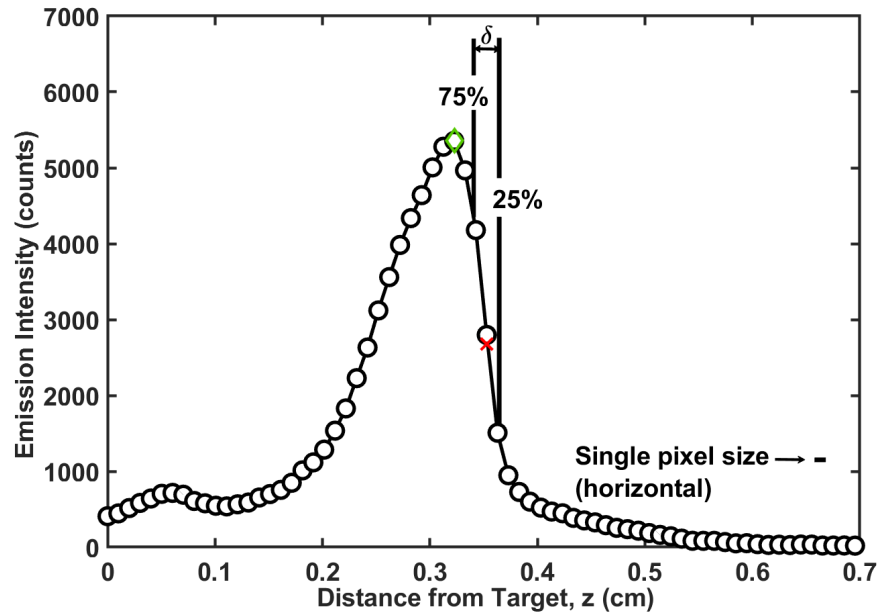


**Figure 5:** Centerline intensity profile with a 5-pixel (0.5 mm) row average corresponding to the image in Fig. 4 with peak intensity ( $\diamond$ ) and defined shock front position at 50% peak intensity ( $\times$ ) at  $t = 369$  ns with no spectral filter in air at 10 Torr.

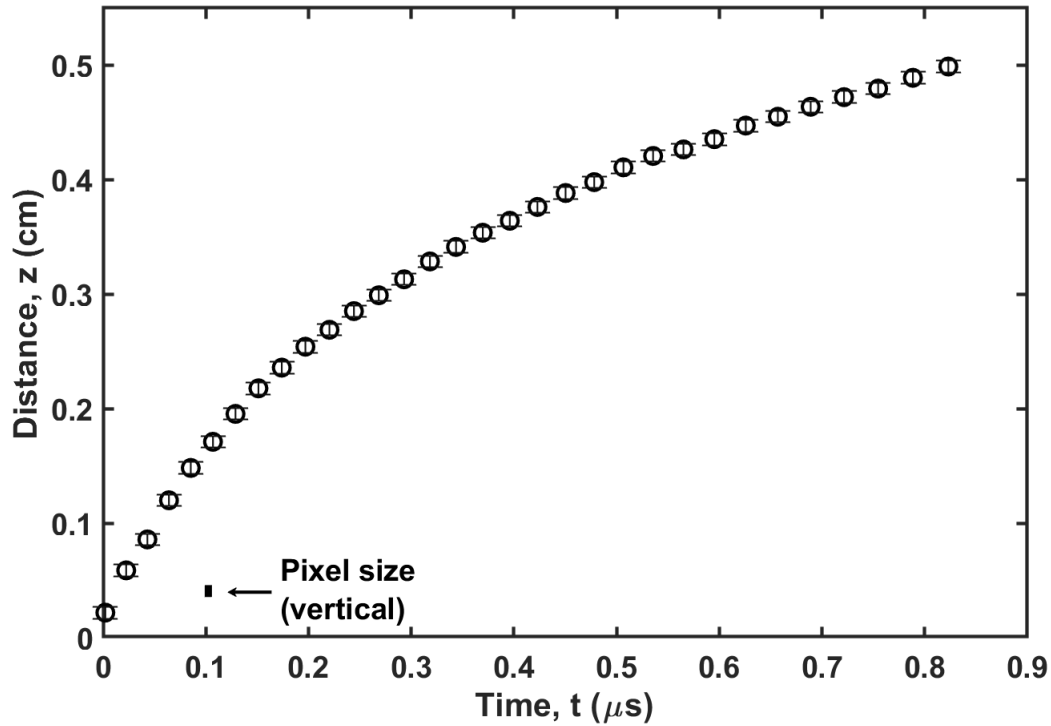


**Figure 6:** Plume shock trajectory for graphite in an air background gas at 10 Torr. The gray vertical error bars represent the  $z$  distance error resulting from the ICCD gate width size which increased from 2.2 ns at the earliest shock location to 3.1 ns for the latest shock location. An ICCD pixel size marker denoted with the arrow is included for reference to the distance axis,  $z$ .

Plume trajectories were characterized by locating the shock front for each camera gate delay as shown in Fig. 6. Instrumental limitations on identifying the shock location are minimal, with a pixel size marker and error bars corresponding to the gate width transit distance typically less than curvature in the trajectory. In Fig. 6, the variable gate widths were narrow starting at 2.2 ns at early times and expanding to 3.2 ns for the final shock image. Positional errors introduced by plume motion during the gate width integration time are  $\sim 1$  pixel for the earliest times and shrink to 0.5 pixels at the later times, due to the slowing of the plume. The dynamics of the ablation plume shock front propagation were characterized into three distinct regions including the early free expansion region, the mid-field blast wave region characterized by the Sedov-Taylor equation, and the full scale drag region characterized by the empirical drag model [5, 52, 61, 72, 101]. Figure 7 shows

an example of the fitting of data to these models.

At very early times, ablated material has not yet interacted with the background gas, and a free expansion model can be used to characterize the trajectory [52]. The free expansion exhibits a linear trajectory corresponding to a constant velocity and is given by:

$$z(t) = v_o t + z_o, \quad (7)$$

where  $z(t)$  is the distance of the shock front to the target at time  $t$ , the slope  $v_o$  is the initial plume velocity, and  $z_o$  is the initial plume position. Data sectioning for the free expansion fits was limited to the first 4 to 10 data points corresponding to the first 100–200 ns of shock propagation where there was still little to no curvature from collisions with the background gas. The small intercept,  $z_o = 0.026 \pm 0.011$  cm corresponds to a time interval of 17.8 ns, less than the laser pulse duration, and represents the uncertainty in defining  $t = 0$  relative to the peak of the laser pulse. The initial velocity for the plume propagating in air at 10 Torr is  $v_o = 1.44 \pm 0.19$  cm/ $\mu$ s, corresponding to a kinetic energy of  $12.9 \pm 3$  eV per carbon atom. The highest free expansion velocity kinetic energy was  $24.4 \pm 5$  eV in 1 Torr nitrogen, while the lowest kinetic energy was  $11.7 \pm 4$  eV in 10 Torr argon as reported in Table 2. The kinetic energy with the smallest uncertainty was the 10 Torr unfiltered argon case at  $12.0 \pm 2.2$  eV. The plume kinetic energy was 2–5 times larger than the 5 eV photon energy, suggesting moderate plume interaction with the laser pulse.

One might expect that the free expansion would not be influenced by the background gas. However, higher initial speed is observed in the lighter helium, and the highest speed for the lower pressure, 1 Torr case. A similar trend has been observed for PLA of graphite in 300 Torr rare gas backgrounds at higher fluence,  $20$  J/cm<sup>2</sup>, with the free expansion speed ranging from a somewhat lower value for helium of 1.45 cm/ $\mu$ s to 0.89 cm/ $\mu$ s for xenon [61]. The higher pressure and somewhat longer camera integration time in the prior work probably introduces some curvature in the trajectory and may have biased the speeds to

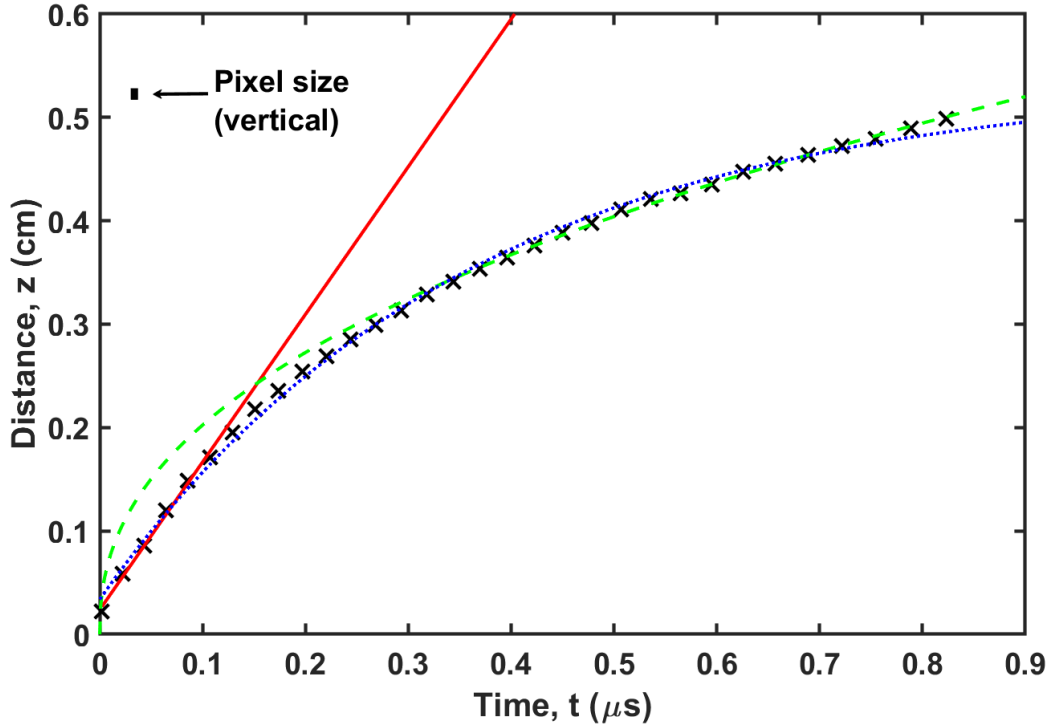


**Figure 7:** Location of graphite shock front position in air at 10 Torr with least-square fits to the free expansion (—), Sedov-Taylor (- - -), and drag (·····) models.

the low side. The laser pulse duration is sufficiently long that the dynamics of the plasma bubble formation influence the final overpressure and possibly the degree of plasma shielding. The increase in the kinetic energy of carbon atoms through the inverse-Bremsstrahlung process and a higher plume density might result in increased plume shielding and energy transfer. Other possible mechanisms for increased plume shielding may include atomic and molecular absorption of the laser energy. Regardless of the mechanism, it is clear that overall plume dynamics are driven by the extra energy deposited within the plume through interaction with the ablation laser.

The free expansion velocities are typically predicted as  $\sim 1 \text{ cm}/\mu\text{s}$  for ns ablation of most materials including graphite [102]. The expansion speed is a multiple of the initial speed of sound, depending primarily on the ratio of specific heats [103]. The weak dependence of expansion speed on target mass, leads to a significant reduction in the kinetic energy for lighter mass targets. For example, the kinetic energy under similar ultraviolet ns pulsed

**Table 2:** Free expansion and drag model fit results for plume propagation.

Gas (Torr)	Free	Drag			
	Exp.	$Z(t) = Z_s (1 - e^{-\beta t})$			
	$v_0$ (cm/ $\mu$ s)	$K.E.$ (eV)	$Z_{Stop}$ (cm)	$\beta$ ( $\mu$ s $^{-1}$ )	$v_0$ (cm/ $\mu$ s)
Air (10)	1.44 $\pm 0.19$	12.9 $\pm 3.4$	0.50 $\pm 0.01$	2.69 $\pm 0.19$	1.35 $\pm 0.12$
Ar (10)	1.39 $\pm 0.13$	12.0 $\pm 2.2$	0.51 $\pm 0.01$	2.37 $\pm 0.15$	1.21 $\pm 0.11$
Ar 520 nm (10)	1.37 $\pm 0.23$	11.7 $\pm 3.9$	0.49 $\pm 0.02$	2.95 $\pm 0.19$	1.45 $\pm 0.11$
He (10)	1.87 $\pm 0.10$	21.8 $\pm 2.3$	1.10 $\pm 0.03$	1.67 $\pm 0.11$	1.84 $\pm 0.13$
N <sub>2</sub> (10)	1.42 $\pm 0.18$	12.6 $\pm 3.2$	0.52 $\pm 0.01$	2.73 $\pm 0.17$	1.42 $\pm 0.09$
N <sub>2</sub> (1)	1.98 $\pm 0.22$	24.4 $\pm 5.4$	1.56 $\pm 0.04$	1.11 $\pm 0.07$	1.73 $\pm 0.12$

laser conditions with fluences several times ablation threshold for aluminum (45.8 eV), [72] titanium (61.1 eV), [72] and barium (284 eV) [52] increase significantly with mass. It is also worth noting that ionization potential for carbon (11.26 eV) is significantly higher, than for the metals Al (5.98 eV) and Ti (6.82 eV), likely resulting in fewer free electrons available to couple with the laser through the inverse-Bremsstrahlung process.

Ablation plume trajectories are commonly characterized using the Sedov-Taylor (ST) scaling first developed for bomb detonations [4, 5, 74, 104]. A more generalized form of the Sedov-Taylor equation than is typically employed for laser ablation is used that allows for variation in plume dimensionality and finite laser pulse duration:

$$z(t) = at^b, \quad (8)$$

where

$$b = (s + 2)/(n + 2), \quad (9)$$

$$a = \xi_n \left( \frac{E_{ST}/(\tau_o^s l_o^{3-n})}{\rho} \right)^{1/(n+2)}, \quad (10)$$

and  $\xi_n \approx 1$  depending on the ratio of specific heats of the background gas and the dimensionality factor  $n$  [74]. The assumption of instantaneous energy deposition,  $s = 0$ , has always been assumed for laser ablation and is appropriate when the plume evolution time is long relative to the laser pulse duration. The value  $s = 1$  represents a constant energy release with rate  $E_{ST}/\tau_o$  where the time scale  $\tau_o$  is defined by the laser pulse duration [74]. The plume dimensionality is often constrained to  $n = 3$  (spherical shock front, point source over-pressure) in laser ablation studies [75, 85, 105]. For this  $n = 3$  case, the length scale,  $l_o$ , is not relevant. However, at early times the plume may appear nearly one dimensional,  $n \approx 1$ , with a planar shock front, as is evident in Fig. 4. Recent studies indicate a dimensionality that decreases with increasing background density,  $\rho$ , and a typical value of  $n = 2.3$  for Al and  $n = 1.9$  for Ti targets. [72] To allow for the evolving plume curvature, Eq. 8 is employed with the average dimensionality as a fit parameter,  $n$ , but constrained to instantaneous energy release,  $s = 0$ .

The ST theory requires sufficient background gas to have been displaced that a well-established emissive shock front is observed but before separation of the shock from the emissive plumes. The ST model is applicable in the range:

$$z_{low} = \left( \frac{3m_a}{2\pi\rho} \right)^{\frac{1}{3}} \ll z \ll \left( \frac{2E_a}{P_b} \right)^{\frac{1}{3}} = z_{high}, \quad (11)$$

where  $m_a$  is the mass ablated from the target,  $\rho$  is the background gas density,  $E_a$  is the ablation energy from the laser, and  $P_b$  is the background gas pressure [104]. The ST model is valid when the mass displaced by the shock front is larger than the mass inside the plume

and when the pressure behind the shock front is still very large compared to the background gas pressure. The ST low limit for the 10 Torr air case was  $z_{low} = 0.31$  cm ( $\sim 30$  pixels) and the high limit is larger than camera field of view and beyond the emissive plume's stopping distance,  $z_{high} = 6.37$  cm. It is worth noting that the plume arrives at the low limit at about  $0.3 \mu\text{s}$ , or about 10 laser pulse durations, supporting the  $s = 0$  instantaneous release approximation. When fitting the observed trajectories to Eq. 8, the data is sectioned to  $z > z_{low}$ . The fit results are provided in Table 3. Figure 8 provides a typical fit to Eq. 9 with  $n = 2.65 \pm 0.12$  and  $a = 0.544 \pm 0.003 \text{ cm}/\mu\text{s}^{2/(2+n)}$ . The poor prediction at early times is a result of the preceding the low limit, represented by the dotted line.

The ST model was used to estimate the energy that goes into the shock wave in the initial ablation event, and are the energies are summarized in Table 3. For cases with  $n \neq 3$ , an estimate of the length scale,  $l_o$ , is required. For bomb detonations in air, the length scale is best described by the ST low limit,  $l_o = z_{low} = (3m_a/2\pi\rho)^{\frac{1}{3}}$  [74]. Using this length scale for the ablation in the air yields  $E_{ST} = 65 \pm 2$  mJ or 38% of the laser pulse energy of 170 mJ. Alternatively, a fixed length scale independent of pressure or ablated mass, possibly associated with the laser spot size, might be employed. If the length scale is fixed to  $l_o = 4.5$  mm (half of the long spot dimension), then the fraction of the laser energy used to drive the shock is less dependent on background gas with an average for all the data of  $37 \pm 5 \%$ . Prior studies of this partitioning of laser energy to the shock disagree dramatically. For a 532 nm,  $30 \text{ J}/\text{cm}^2$  ablation of graphite in argon at 1.5–15 Torr, the ST energy was 70% of the laser energy, whereas at 193 nm and  $25 \text{ J}/\text{cm}^2$  in atmospheric air only 5–7% of the laser energy drove the shock [85, 105]. In both cases, the ST fits were constrained to  $n = 3$ . The current result differs significantly from the prior UV study, suggesting that increase inverse-Bremsstrahlung at shorter wavelengths is not the explanation for the observed differences. It seems more likely that the high atmospheric pressure used in the prior ArF study reduces the coupling. These trends are discussed in context of other target

**Table 3:** Sedov-Taylor fit results.

Gas (Torr)	ST $R(t) = at^{\frac{2}{n+2}}$				ST for $n = 3$ $R(t) = at^{0.4}$	
	$n$	$a$ (cm/ $\mu\text{s}^{2/(n+2)}$ )	$E_{ST}$ $l_o = z_{low}$ (mJ)	$E_{ST}$ $l_o = 0.45$ cm (mJ)	$a$ (cm/ $\mu\text{s}^{0.4}$ )	$E_{ST}$ (mJ)
Air (10)	2.66 $\pm 0.12$	0.544 $\pm 0.004$	65 $\pm 2$	69 $\pm 2$	0.535 $\pm 0.003$	68 $\pm 2$
Ar (10)	2.82 $\pm 0.14$	0.473 $\pm 0.003$	48 $\pm 2$	50 $\pm 2$	0.468 $\pm 0.002$	49 $\pm 1$
Ar 520 nm (10)	2.29 $\pm 0.19$	0.515 $\pm 0.007$	58 $\pm 4$	70 $\pm 4$	0.495 $\pm 0.005$	63 $\pm 3$
He (10)	1.81 $\pm 0.1$	0.902 $\pm 0.005$	79 $\pm 2$	55 $\pm 1$	0.877 $\pm 0.016$	111 $\pm 10$
N <sub>2</sub> (10)	2.54 $\pm 0.19$	0.544 $\pm 0.006$	61 $\pm 3$	65 $\pm 3$	0.531 $\pm 0.004$	63 $\pm 2$
N <sub>2</sub> (1)	1.83 $\pm 0.14$	1.04 $\pm 0.008$	106 $\pm 3$	68 $\pm 2$	1.06 $\pm 0.001$	199 $\pm 1$

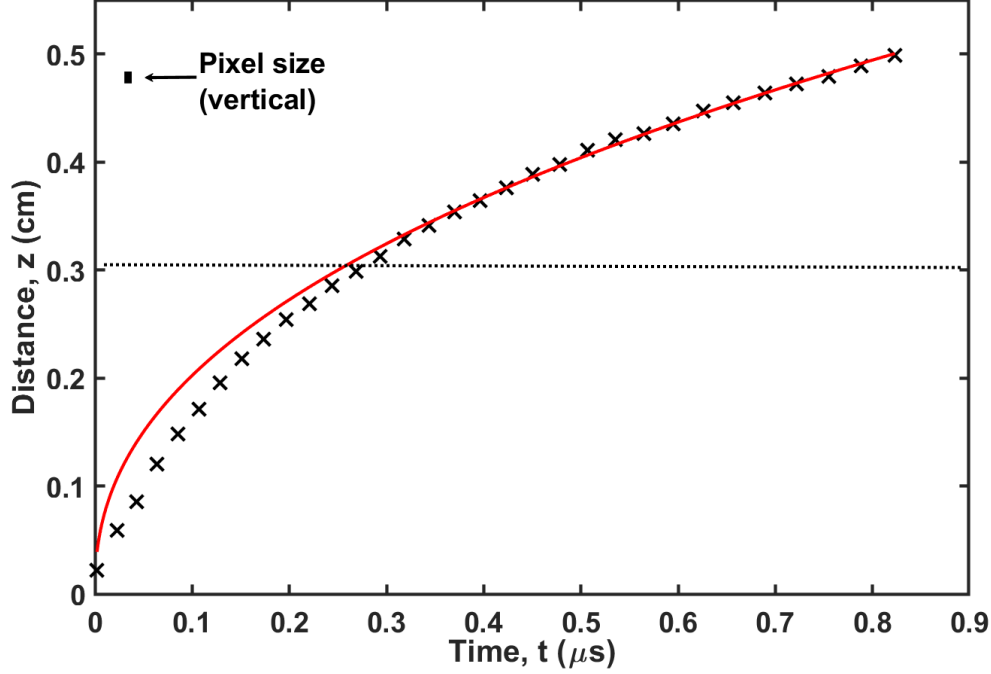


**Figure 8:** Sedov-Taylor fit for graphite in air at 10 Torr. The fit coefficients are  $a = 0.544 \pm 0.003$   $\text{cm}/\mu\text{s}^{2/(n+2)}$ , and dimensionality  $n = 2.65 \pm 0.12$ . The dotted line is the low limit,  $0.316 \pm 0.03$  cm. The high limit is 6.37 cm.

materials in the discussion below.

The final region of the emissive plume expansion is dominated by drag as the expanding plume encounters the background gas, slows and the collision excitation of emitting states declines. Late in the plume trajectory, the emissive plume separates from the shock front and comes to a maximum displacement. The empirical drag model exponentially approaches the stopping distance:

$$z(t) = z_s (1 - e^{-\beta t}) + z_o, \quad (12)$$

where  $z_s$  is the plume stopping distance and  $\beta$  is the drag coefficient [106, 107]. The stopping distance for graphite ablation in air at 10 Torr was  $z_s = 0.50 \pm 0.01$  cm and the initial velocity is  $v_o = 1.35 \pm 0.12$   $\text{cm}/\mu\text{s}$ . As with the free expansion fit, an intercept term  $z_o = 0.041 \pm 0.008$  cm was added to the drag fit to account for experimental timing uncer-

tainty. Both the free expansion and drag initial velocities agreed to within 0.1 cm/ $\mu$ s. The trajectories for the various gases and pressures are provided in Fig. 9, and fit results are summarized in Table 2.

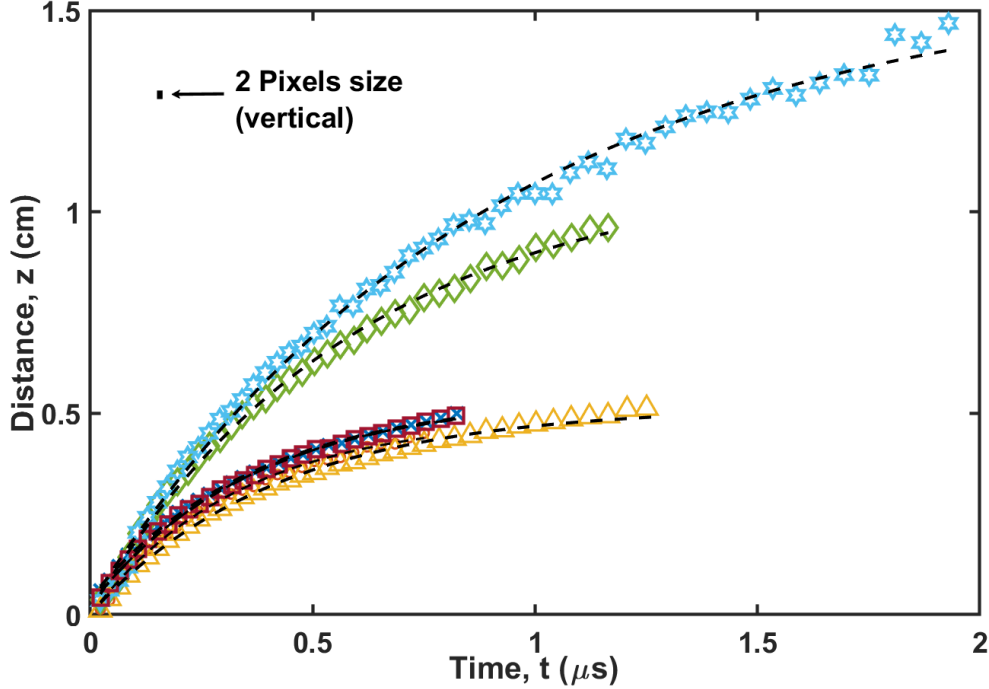


**Figure 9:** Graphite plume trajectories in air ( $\times$ ), argon ( $\Delta$ ), argon using the  $C_2$  filter ( $\circ$ ), helium ( $\diamond$ ), and nitrogen at 10 Torr ( $\square$ ) and nitrogen at 1 Torr ( $\star$ ). Drag fits are represented by dashed lines (---).

Plume stopping distances,  $z_s$ , increase at lower pressure and for the lighter He collision partner. A similar trend is observed for the drag initial velocities and Sedov-Taylor dimensionality,  $n$ , which trends towards spherical for heavier collision partners and towards planar for lighter gases. The previous study of graphite plume stopping distance with a higher fluence,  $F = 20 \text{ J/cm}^2$  excimer laser source examined He, Ne, Ar, and Xe background gases at 300 Torr [61]. Their results are about 40% of the stopping distances for He and Ar in this study, and decrease from  $z_s = 0.41 \text{ cm}$  to 0.15 cm as the mass of the background gas increases from He to Xe. Clearly, the stopping distance decreases less than linearly with pressure and more than a factor of two between He and Ar. These trends may be interpreted from a translational-to-electronic (T-E) energy transfer event that oc-

curs within the contact front to produce the electronic excitation. Momentum conservation considerations suggest the helium is rapidly pushed forward in such an interaction and the carbon atoms suffer less reduction in speed, whereas heavier collision partners are more difficult for the ablated mass to plow through. Indeed, the T-E rates are expected to be higher in background gases with a mass more similar to the carbon atoms or molecules. The higher T-E rates also imply a larger change in the time of flight velocity distributions of the dark plume.

Table 2 and Table 3 also provide results when using a band pass filter to emphasize  $C_2$  emission in the argon background. The error estimates are almost double for most parameters, due to the lower total signal. The free expansion speeds are similar, but the drag initial speeds were 19% higher than (but almost within the error bounds of) the broadband results. The Sedov-Taylor dimensionality of the broadband argon case was nearly spherical, while the  $C_2$  dimensionality was closer to cylindrical, possibly reflecting a different production mechanism. The Sedov-Taylor energy for the  $C_2$  filtered case was 17% higher than the broadband case and significantly greater than the error bounds.

### **3.3.2 Diffuse Emission at Early Times**

An area of diffuse emission was evident in the ICCD imagery at early times ( $< 150$  ns) for the 10 Torr  $C_2$ -filtered argon, 10 Torr helium and 1 Torr nitrogen cases. Early diffuse emission was not evident in the 10 Torr air, 10 Torr nitrogen, and 10 Torr unfiltered argon cases. The phenomenon was the most pronounced in the 1 Torr nitrogen case, which can be seen in Fig. 10 as an ICCD imagery sequence consisting of the first 8 frames from 2.2–150 ns after the termination of the laser pulse.

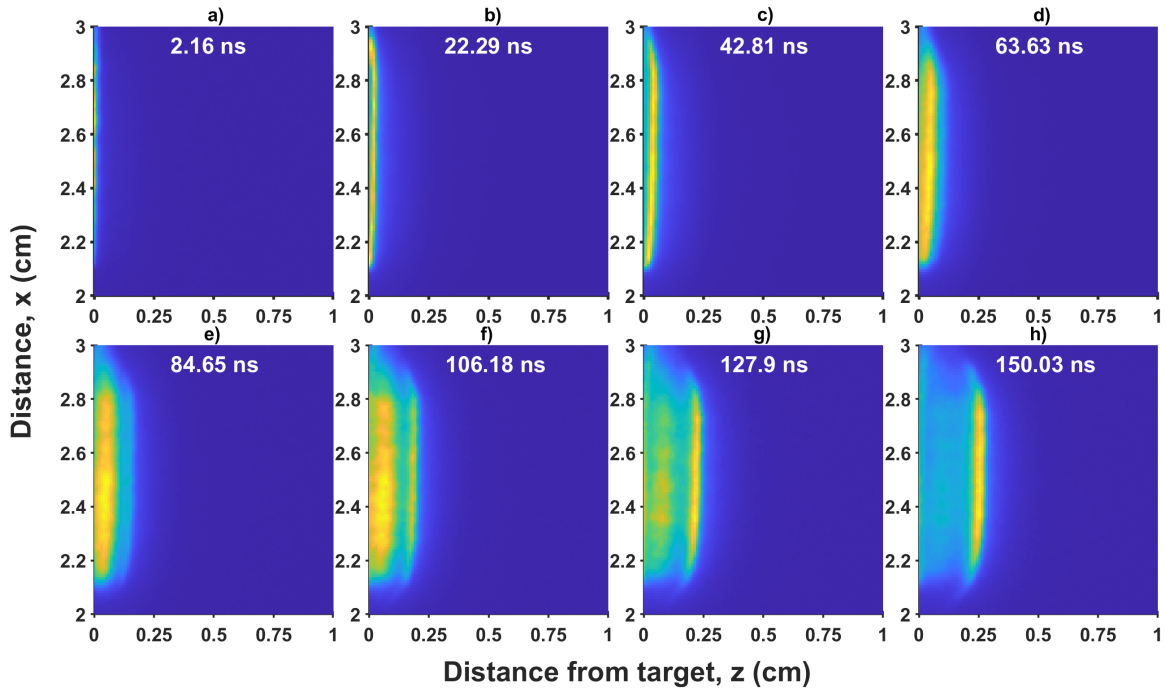


**Figure 10:** (a–h) Unfiltered ICCD images demonstrating diffuse emission at early times for graphite in nitrogen at 1 Torr. Images show gate delays from 2.2 ns to 150 ns with emission from the shock front appearing at 84.7 ns (e). The diffuse emission peak intensity occurs at 106.2 ns (f), and has faded by 150.3 ns (h).

The diffuse emission appears at 2.2 ns and then grows in intensity and size, peaking in intensity at 106.2 ns. The emissive shock front is first discernible at 84.7 ns and continues to grow in intensity while propagating away from the target surface. The area of diffuse emission begins to fade away at 128 ns, becoming much less intense than the propagating emissive shock front by 150 ns. The speed of propagation of the early diffuse emission region is relatively slow. A similar feature was seen by Yadav et. al. at  $10^{-5}$  Torr, who found that the faster component in their work was primarily composed of  $C_2$  molecules [108]. They postulated that the early emission was possibly due to collisions between the plume and background gas in the free expansion region near the Knudsen layer [108].

However, the emission in the present work is only visible in several gas/pressure cases and collisions near the Knudsen layer should be present in all the cases if that was the primary cause. A possible alternative explanation for the diffuse emission is that some

carbon atoms are produced with significant excitation before the laser pulse has terminated. These atoms ablate off the surface at relatively slow speeds and continue to emit brightly for approximately one radiative lifetime. These atoms did not stay within the confined volume of the plume where significant laser-plume absorption occurs, and their kinetic energy was not strongly boosted by inverse-Bremsstrahlung processes.

The diffuse emission also appears to obscure the emissive shock front from view due to its higher intensity and initial overlap until 84.7 ns has passed. It is possible that for times earlier than 84.6 ns, the kinetic energy of the plume might be high enough that the energy-dependent cross section for translational to electronic energy transfer is small, resulting in no emission visible from the shock front for those times. As the shock front experiences increasing collisions with the background gas and loses energy, the cross section grows resulting in the start of the shock front emission near 84.65 ns. A more likely explanation for the apparently missing shock front emission before 84.65 ns is that there have not been enough collisions with the background gas to form the shock front at those early times and the emissive shock front only forms at 84 ns.

### **3.4 Discussion**

#### **3.4.1 Sedov-Taylor Blast Energy**

In Fig. 11, the blast energies from the Sedov-Taylor fits relative to the laser pulse energy are presented as a function of stopping distance normalized to the mean free path,  $\lambda$ , using both the present results and prior literature for targets composed of titanium [72], aluminum [72], barium [52], and graphite [17, 21, 24, 85, 105]. A broad range of pressures from 0.025 to 760 Torr and various background gases including oxygen, argon, nitrogen, helium, and air are included for the diverse set of target materials. For higher pressures and lower mean free paths,  $z_s/\lambda > 400$ , the ST energy approaches the pulse energy. Below this transition value for  $z_s/\lambda$ , the ST energy generally increases with the exception of Ti in Ar. The prior

titanium results exhibit energy ratios significantly above unity, attributed by the authors as an overestimation by the ST method [72]. The results for graphite and aluminum are less sensitive to stopping distance than the Ba targets, where the energy coupling is quite low at small stopping distances. There are clearly distinctive groupings of the target materials with energy ratios for graphite tending to be larger for lighter background gases such as helium. The graphite cases also exhibited stopping distances 2 to 8 times smaller than the aluminum, titanium, and barium results in the literature. The graphite in the 1 Torr nitrogen case ablated with a KrF laser in this work exhibited a significantly higher energy ratio near 100% compared to the graphite in 0.9 Torr nitrogen case in the literature with a ratio of 10% using an Nd:YAG laser. This is mostly likely due to increased coupling of the KrF laser energy into the plume as compared to the Nd:YAG laser case.

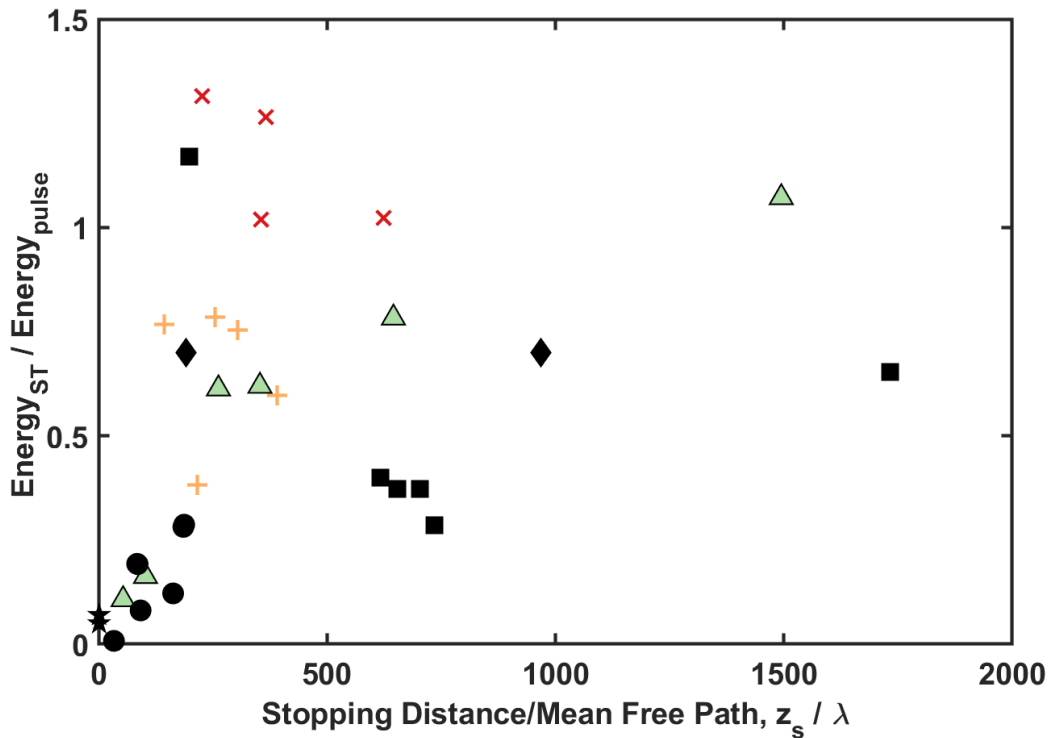


**Figure 11:** Sedov-Taylor/laser pulse energy ratio versus stopping distance normalized with mean free path for graphite results in this work (■) compared to barium [52] (△), graphite [17, 21, 24] (●), graphite from Márton et. al. [85] (★), graphite from Mahmood et. al. [105] (◆), and titanium (+) and aluminum from Bauer [72] (×).

Indeed, the proposed scaling for ST energies in Fig. 11 appears to be rather robust for a wide range of materials and conditions and explains the significant differences previously reported [85, 105]. For a doubled Nd:YAG laser ablation of graphite in argon at 1.5–15 Torr, the ST energy was 70% of the laser energy, [105] whereas for a UV excimer laser in atmospheric air only 5-7% of the laser energy drove the shock [85]. The pressure scaling suggested by the normalization to mean free paths seems to correlate the results despite the differences in wavelength, pulse duration and fluence.

### **3.4.2 High Limit Ablated Mass and Hole Depth Estimates**

Weighing targets to determine ablated mass can be problematic in graphite and other materials for several reasons including redeposition, target fragility, and oxidation. Redeposition of a portion of the ablated plume material back onto the surface of the target can result in an underestimation of ablated mass [41]. The fragility of the target material can result in mass loss during the process of handling a sample during mounting, unmounting, and any steps where the sample is physically touched or moved in order to weigh it before or after ablation. In addition, many target materials, including metals and graphite in certain conditions, can oxidize in the environment potentially influencing ablated mass measurements [56].

The graphite targets in this study were not weighed. However, an upper bound for the graphite ablated mass could be estimated using the measured free expansion initial velocity, the ablation threshold energy, the laser pulse energy, laser parameters including spot size area and pulse duration, and the physical target material parameters such as heat of vaporization and reflectivity. By removing the energy sinks from the total laser pulse energy and assuming that the remaining energy goes into the kinetic energy the assumption that all the laser pulse energy goes into kinetic energy in the plume. The equation for the

high estimate of ablated mass is:

$$m_a = \frac{E_p(1 - R) - \rho h_s \sqrt{\frac{\kappa}{C_p \rho}} \tau_p A_L}{\frac{1}{2} v_o^2}, \quad (13)$$

where  $m_a$  is the mass ablated,  $E_p$  is the laser pulse energy,  $R$  is the reflectivity,  $\rho$  is the density,  $h_s$  is the heat of sublimation,  $\kappa$  is the diffusivity,  $C_p$  is the specific heat,  $\tau_p$  is the laser pulse duration,  $A_L$  is the laser spot area, and  $v_o$  is the initial velocity. For example, an upper limit of 0.69  $\mu\text{g}$  can be removed per pulse for graphite in air at 10 Torr using the parameters in Table 1, and a reflectivity of 0.094 [109].

The ablated mass estimates can be compared with theoretical predictions using the laser pulse duration, target material thermal properties, and target density, assuming no explosive boiling or spallation occurs. If the volume of the hole is defined by laser footprint and the thermal diffusion length:

$$l_D = \sqrt{4 \frac{K}{C_p \rho} \tau_p}, \quad (14)$$

where  $\frac{K}{C_p \rho}$  is the thermal diffusivity given by the thermal conductivity  $K$ , specific heat at constant pressure  $C_p$ , and graphite density  $\rho$ , and  $\tau_p$  is the duration of the laser pulse, then the mass is defined by this volume and the graphite density [2]. The key assumption is that the laser ablates the material to a depth equal to the thermal diffusion length across the entire laser footprint, which is most appropriate for longer pulses [11]. The material properties of the graphite samples include a thermal conductivity of 3.5 W/m·K and a density of 2.19 g/cm<sup>3</sup> [98]. Assuming a specific heat of 2,135 J/kgK at 3,500 K and 25 ns pulse duration, Eq. 14 yields a thermal diffusion length of  $l_D = 273.6$  nm [99]. A 4.5 mm<sup>2</sup> laser spot size yields an ablated volume of 0.001231 mm<sup>3</sup> corresponding to a mass of 2.67  $\mu\text{g}$ . Using a similar process, an estimated hole depth can be calculated with:

$$\text{Estimated Hole Depth} = \frac{m_a}{A_L \rho}, \quad (15)$$

which yields an estimated hole depth of 70 nm for the 10 Torr air. It is clear from comparing the 0.69  $\mu\text{g}$  ablated mass estimate for the 10 Torr air case to the theoretical ablated mass of 2.67  $\mu\text{g}$  that the hole depth estimated from the free expansion velocity is 26% of the diffusion length. The current estimates agree favorably with the 300 nm depths observed in earlier KrF laser ablation of graphite at somewhat higher fluence (10  $\text{J}/\text{cm}^2$ ) [87]. In contrast, the depths in graphite with an ArF laser increase linearly with fluence to about 150 nm at 10  $\text{J}/\text{cm}^2$  [85]. The trends are similar for much shorter 120 fs pulses where the depth grows to 180 nm at 5  $\text{J}/\text{cm}^2$ . This simple model for a high limit ablated mass could be improved by adding the effects of other processes into the calculation. In addition, mass estimates could include factors including the Sedov-Taylor energy, which is not available to ablate material from the surface since the energy is absorbed by the plume. However, a contribution of the Sedov-Taylor energy is inherent in the model since the high initial velocity of the plume material is primarily a result of the laser-plume energy transfer. The overall degree of plume shielding including plume absorption and scatter of the incident laser radiation could also be included to better bound a mass ablation estimate. However, the intent here is to provide a simple, rough order of magnitude high estimate of mass ablated to allow for rapid analysis of ablation plumes.

### 3.4.3 Non-dimensional Factors for Hole Depth, Fluence, and Pulse Duration

Van Woerkom et al. recently introduced non-dimensional scaling factors for comparing materials with different pulse durations (100 ps to 100 ms) and fluences (0.004–25  $\text{kJ}/\text{cm}^2$ ) by defining a non-dimensional hole depth, a non-dimensional fluence, and a non-dimensional pulse duration [11]. They defined the non-dimensional hole depth,  $h^*$ , as

$$h^* = \frac{h}{l_D} \quad (16)$$

where  $h$  is the measured hole depth, and  $l_D$  is the thermal diffusion length defined in Eq. 14 [11]. They defined the non-dimensional fluence,  $f^*$ , given as

$$f^* = \frac{F}{F_{th}} \quad (17)$$

where  $F$  is the delivered fluence on the target and  $F_{th}$  is the material ablation threshold fluence given by:

$$F_{th} = \rho h_s \sqrt{\frac{\kappa}{C_p \rho} \tau_p}, \quad (18)$$

and  $h_s$  is the latent heat of vaporization or sublimation for the material [11]. They also defined the non-dimensional pulse duration,  $t^*$ , given by:

$$t^* = \frac{t_p}{t_\omega} = \frac{4\kappa t_p}{\omega_0^2}, \quad (19)$$

where  $t_p$  is the laser pulse duration and  $t_\omega$  is the time for heat to diffuse over a length equal to the laser spot radius,  $\omega_0$  [11]. Using the material properties in Table 1, Eq. 18 predicts  $F_{th} = 1.84 \text{ J/cm}^2$  which agrees rather well with the experimental determination of  $1.45 \text{ J/cm}^2$  [85]. Thus the fluence is just slightly above twice the ablation threshold,  $f^* = 2.06$ . Since the fluence is not significantly higher than the graphite ablation threshold, additional ablation from explosive boiling is most likely not present. Using the estimated hole depths from the free expansion velocities of Sec. 3.1, the current results are slightly less than the thermal diffusion length, and  $h^*$  ranges from 0.14 for 1 Torr nitrogen to 0.28 for 10 Torr argon.

Van Woerkom et al. examined the laser ablation of aluminum, titanium, germanium, silicon, and indium antimonide for a range of fluences and pulse durations but only for ablation in ambient air [11]. The current results at low pressure and carbon offer a further test of their scaling, as illustrated in Fig. 12. The pulse duration is short relative to the thermal diffusion time for this work, resulting in  $t^* = 1.67 \times 10^{-8}$ , and so the present data

should be compared with the results for  $t^* < 1$ . The new results lie on the low  $h^*$ ,  $f^*$  limit of the  $t^* < 1$  scaling and are consistent with an extrapolation from the bulk of the prior data.

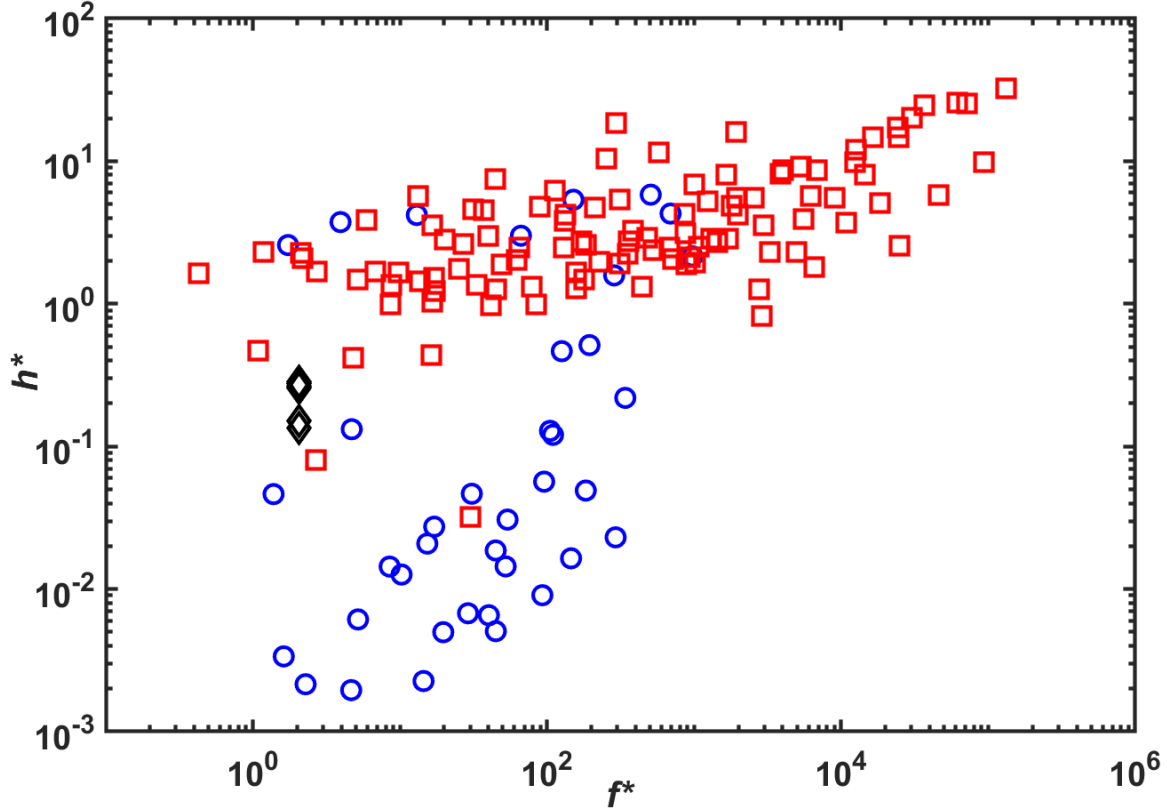


**Figure 12:** Non-dimensional hole depth,  $h^*$ , as a function of non-dimensional fluence,  $f^*$ , for graphite in this study ( $\diamond$ ), and for various materials  $t^* < 1$  ( $\square$ ),  $t^* > 1$  ( $\circ$ ) from Van Woerkom et al. [11]

### 3.4.4 Shock Thickness and Strength in Graphite and Barium

Pulsed laser ablation offers an opportunity to explore shock thickness at very high Mach numbers. The older shock tube studies of shock thickness are generally limited to 1-D flow into high pressure backgrounds at  $M < 9$  [65–70, 110]. The prediction of increasing shock thickness at higher speeds due to the temperature dependent viscosity appears to be inconsistent with the two prior pulsed ablation studies [52, 71]. However, imagery of the emissive plumes from laser ablation are difficult to interpret for shock strength due

to several complications: (1) a dynamic, 3D expansion with shock curvature along the imaging axis, (2) a possibly complex relationship between emission and pressure profiles due to the kinetic excitation mechanism.

Thickness of the emissive plume contact front is defined here as  $\delta$ , the distance between 25% and 75% of the maximum intensity for the leading edge of the plume as illustrated in Fig. 5 and as previously recommended [52, 71]:

$$\delta = \frac{I_m - I_b}{I_m / (z_{75} - z_{25})}, \quad (20)$$

where  $I_m$  is the peak intensity,  $I_b$  is the pre-shock intensity, and  $z_{25,75}$  is the distance from the target where the leading edge intensity is 25% or 75% of the peak [52]. The use of Eq. 20 depends on the assumption that emission at the plume contact front resulting from collisions with the background gas adequately represents shock front structure, and that the thickness of the contact front intensity profile is analogous to shock thickness. Several definitions of shock strength are used in the study of shock waves. However, this work adopts the definition of shock strength as the reciprocal of shock thickness,  $S = 1/\delta$ , typically used in hydrodynamic modeling with Navier-Stokes equations [68, 110–112]. Shock thickness is usually based on the pre-shock flow velocity or density:

$$\delta_v = \frac{v_1 - v_2}{\left(\frac{dv}{dz}\right)_{max}}, \quad (21)$$

where  $v_1$  is the post-shock velocity and  $v_2$  is the pre-shock velocity [70, 92]. The pre-shock velocity is near zero and the pre-shock intensity is near zero, so if the intensity gradient is proportional to the velocity gradient, then Eq. 20 and Eq. 21 yield similar results. The shock speed and thickness vary with plume propagation time as illustrated in Fig. 13.

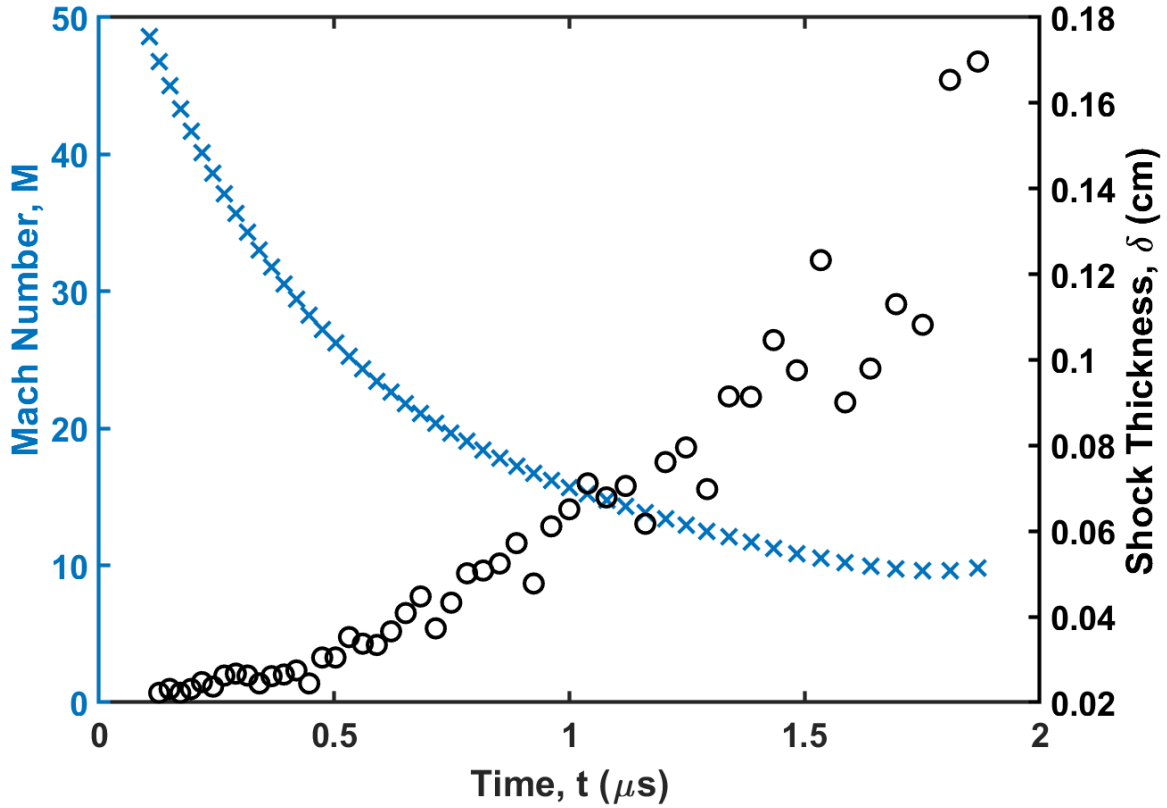


**Figure 13:** Evolving shock speed ( $\times$ ) and thickness ( $\circ$ ) for nitrogen at 1 Torr.

The spatial resolution is at best limited by the imaged pixel size of  $102 \mu\text{m}/\text{pixel}$  and a shock strength of greater than  $S = 1/\delta > 100 \text{ cm}^{-1}$  clearly cannot be discerned. Prior studies employed a slightly poorer spatial resolution with strengths limited to  $30\text{--}40 \text{ cm}^{-1}$  [52, 71]. The mean free path, as evaluated below, in the background helium at 1 Torr is only slightly smaller than a pixel,  $\lambda = 63 \mu\text{m}$ , and shock thickness is usually a few mean free paths. The situation is further complicated by curvature in the emissive contact front along the imaging line of sight. Near the target the contact front is rather planar ( $n \approx 1$ ) and the Mach number is high ( $M \sim 48$ ). Under these conditions at 1 Torr, the shock thickness is able to be discerned. To compare shock strengths in different background gas and pressure conditions, the shock strength was normalized by multiplying it by the mean free path for

the specific conditions. The mean free path is defined as:

$$\lambda = \frac{1}{\sqrt{1 + \frac{m_1}{m_2}} \frac{P}{k_b T} \pi (r_a + r_b)^2}, \quad (22)$$

where  $m_{1,2}$  are the masses of the graphite and gas molecules respectively,  $P$  is the gas pressure,  $k_b$  is Boltzmann's constant,  $T$  is the temperature of the gas, and  $\pi (r_a + r_b)^2$  is the collision cross section using  $r_{a,b}$ , the radii of the graphite and gas molecules [113]. Molecular radii for the background gases were calculated from viscosity values from Jordan, while the Van der Waals radius was used for graphite [113, 114]. The resulting collision cross sections are  $0.32 \text{ nm}^2$  for air,  $0.33 \text{ nm}^2$  for  $\text{N}_2$ ,  $0.24 \text{ nm}^2$  for He,  $0.39 \text{ nm}^2$  for Ar,  $0.38 \text{ nm}^2$  for  $\text{O}_2$ , and  $0.60 \text{ nm}^2$  for graphite. Using the collision cross section for  $\text{N}_2$  with Eq. 22, the resulting mean free path for 1 Torr  $\text{N}_2$  is  $\lambda = 78 \text{ }\mu\text{m}$ , while the mean free path for 10 Torr  $\text{N}_2$  is  $\lambda = 7.8 \text{ }\mu\text{m}$ .

Figure 14 shows normalized shock strengths versus Mach number from a variety of sources. Three older shock tube studies reported shock thickness up to  $M = 9$  [69, 110, 115]. The normalized shock strength rises quickly to  $\sim 0.35$  near  $M \sim 4$ , and then decreases to lower strength as the Mach number increases. The analytic theory developed by Kremer and Müller agrees favorably with the previous observations, particularly for a temperature dependent viscosity  $\mu \sim T^s$  when  $s = 0.64$  [68]. The two prior results from pulsed laser ablation and the present results extend the observations to  $M = 33\text{--}50$ . The shock thickness remains about 3 mean free paths. The analytic theory for  $s = 0.82$  and  $s = 0.64$  is extrapolated to  $M = 60$  in Fig. 14. Both theory predictions show a decreasing mean free path to shock thickness ratio while the pulsed laser ablation observations reveal an increasing trend to a ratio of  $\sim 0.3$  to  $0.35$ . The extrapolated model does not hold for  $M > 33$ , with significant deviation for higher Mach numbers. The effects of viscosity and thermal conduction are usually ignored for weak shocks but become important in the strong shock regime [70]. A common model that incorporates temperature dependent viscosity does not

extrapolate well for  $M > 2.5$  [70]. Further ablation experiments allowing for the differences in gas viscosities and thermal properties to include Reynolds numbers may be needed to further collapse dimensionality of the shock strength magnitude versus Mach relationship and allow for a clearer comparison between different target materials and conditions.

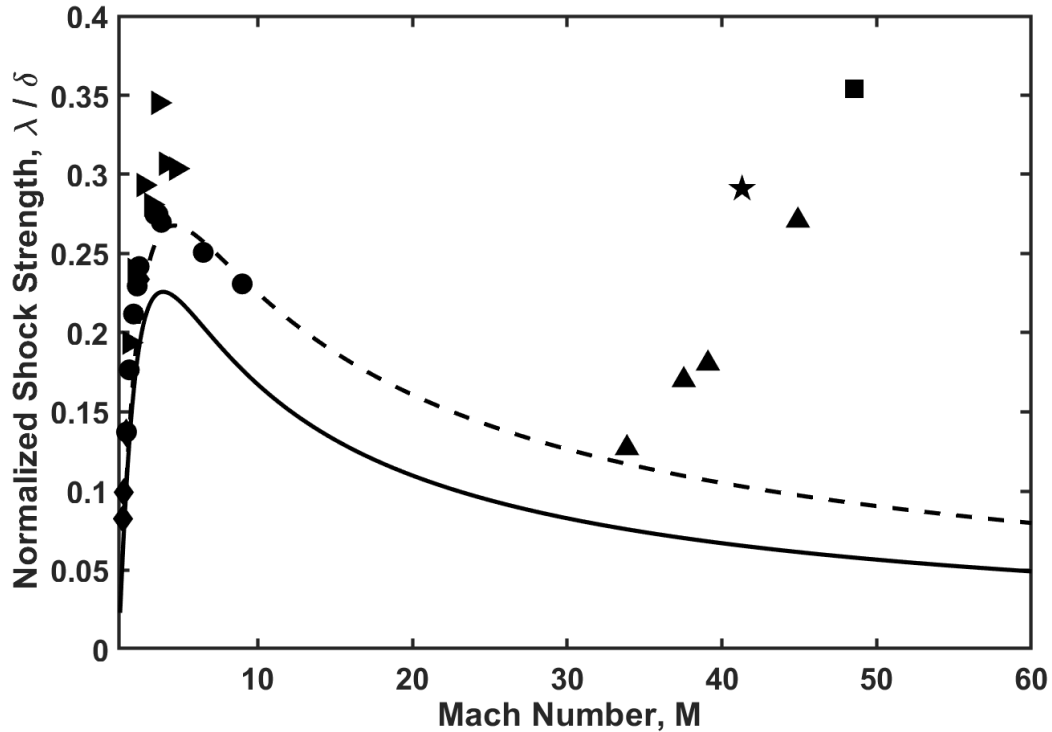


**Figure 14:** Normalized shock strength from shock tube experiments: in  $N_2$  (▶) [69], in Ar (◆) [115] and (●) [110], and pulsed laser ablation: Ba in  $O_2$  at 0.05–0.4 Torr (▲) [52], C in Ar at 0.3 Torr (★) [71], and the present results in  $N_2$  at 1 Torr (■). Predictions from the analytic theory [68] for  $s = 0.82$  (—) and  $s = 0.64$  (- - -).

### 3.5 Conclusions

Plume propagation dynamics resulting from 25 ns UV ablation of graphite at  $4 \text{ J/cm}^2$ , slightly above twice the ablation threshold, have been studied using fast gated imaging. Initial plume expansion speeds are  $v_o = 1.37\text{--}1.98 \text{ cm}/\mu\text{s}$  with Mach numbers as high as  $M = 48$ . The corresponding kinetic energies are 12–25 eV/atom corresponding to 2–5 laser photons. The plumes start with a nearly planar shock front, evolving to higher

dimensionality as the plume evolves. An improved Sedov-Taylor blast wave analysis allows for an estimate of the average plume dimensionality which ranges from  $n = 1.8$  at 1 Torr of nitrogen to nearly hemispherical at  $n = 2.8$  for 10 Torr of argon. The initial energy released is typically  $\sim 33\%$  of the initial laser pulse energy, depending on the choice of length scale. The shock wave energies ranged from a high of 0.106 J for 1 Torr nitrogen to a low of 0.048 J for 10 Torr argon. At longer propagation times, the emissive plume separates from the shock front and reaches a stopping distance of  $z_s = 0.5$  cm for heavier background gases to  $z_s = 1.1$  cm for helium at 10 Torr and further yet,  $z_s = 1.6$  cm, for nitrogen at 1 Torr. For the drag model, predicted initial velocities were consistent within  $\pm 6\%$  of free expansion initial velocities.

The fraction of laser pulse energy released in the blast wave scales with plume stopping distance relative to the mean free path. The energy fraction approaches unity for stopping distances of  $\sim 600$  mean free paths. This proposed scaling is validated from a broad range of studies despite differences in wavelength, pulse duration, fluence and target material.

A recent scaling of hole depths relative to the thermal diffusion length (normalized  $h^*$ ) as a function of fluence relative to threshold conditions (normalized  $f^*$ ) has been tested with the graphite results in this work and validated. The current results lie on the low  $h^*$ ,  $f^*$  limit for  $t^* < 1$  and are consistent with an extrapolation from the majority of the prior data, despite the larger laser footprint in this work.

Pulsed laser ablation offers an opportunity to study shock propagation for high Mach number flows. Shock thickness remains near several mean free paths at the very high Mach numbers encountered near the target,  $M = 48$ . The shock thickness at these high speeds due to the temperature dependent viscosity appears to be underpredicted by analytic theory. Further exploration of shock thickness in pulsed ablation plumes under 1-D expansion conditions is suggested to validate theoretical expectations.

## IV. Shock front detachment during pulsed laser ablation of graphite

Pulsed laser ablation of pyrolytic graphite with a  $5.7 \text{ J/cm}^2$  frequency-doubled Nd:YAG laser in backgrounds of argon, nitrogen, and mixed gas at pressures from 3 to 180 Torr was performed to study the dynamics of the ablation shock wave and plume emissive contact front. White light schlieren shock wave imaging and optical emission imaging with a 2.88–40 ns gated ICCD camera was used to determine shock wave and emissive plume trajectories to find the location of shock detachment from the plume and for blast energy characterization by Sedov-Taylor theory. The shock detachment points are used to limit emissive contact front Sedov-Taylor fits to the portion of the plume which exhibits a shock-like trajectory, resulting in improved laser-plume coupling energy estimates compared to standard fits. The emissive plume expands with initial Mach numbers up to  $M \sim 54$  at  $t = 62 \text{ ns}$ , decreasing to  $M \sim 7$  as the emission becomes too weak to detect after several microseconds. The shock wave expands with initial Mach numbers up to  $M \sim 55$  at  $t = 62 \text{ ns}$ , decreasing to  $M \sim 1$  at  $t = 20 \text{ }\mu\text{s}$ . The shock waves exhibit spherical shock fronts, but the dimensionality,  $n$ , decreases as pressure and mass of the background gas increase, while the plumes exhibit an opposite trend. The Sedov-Taylor energy released in the sudden ablation is typically 55–75% of the laser pulse energy. The detachment-limited blast energy calculations for the emissive plume agree to within 3–5% of the shock wave energy values. Shock detachment points are nearer the target at higher pressure and scale with the mean free path.

### 4.1 Introduction

Pulsed laser ablation (PLA) of graphite materials has a wide variety of applications including thin film and nano-material production including silver and fullerene nanoparticles [43, 116, 117] and superconducting films [19, 118], characterization of hypersonic thermal

protection materials [8, 119], and characterization of laser weapon effects [9, 10]. Optical characterization of emissive plume dynamics includes trajectories, kinetic energies of atomic and molecular species, and laser-plume coupling and are essential to most material processing quality control strategies [1, 2] as they reflect the conditions of ablation and inform the state of the final product [2, 3, 43].

Prior laser ablation studies of graphite have primarily focused on the formation and dynamics of neutral and ionized atomic and molecular constituents in the emissive plume [12, 17, 21, 24–27, 29, 59]. Although a couple of studies have included some exploration of the actual shock wave [64, 75], most focus on the emissive plume contact front, and no studies have focused on the effects of shock wave propagation in conjunction with the emissive plume. In 1999, Kokai et. al. explored graphite ablation in ambient argon with shadowgraphy, fast imaging, and emission spectroscopy [75]. Their shadowgraphy identified a darkened region in the slower, interior of the plume attributed to ablated carbon species. Neither of these studies characterized detachment of the shock from the emissive plume. In 2013, Singh, Gupta, and Thareja investigated plume and some shock wave dynamics for graphite ablation in ambient nitrogen using fast imaging, emission spectroscopy, and a Nomarski interferometer to characterize the location of  $C_2$  and CN species within the plume [64]. They observed a bifurcation in the emissive plume associated with different dynamics for carbon clusters and molecular species.

Pulsed laser ablation offers an opportunity to explore shock wave propagation under extreme conditions. Shock wave propagation is often indirectly studied by characterizing the emissive plume contact front propagation trajectories with blast wave expansion (Sedov-Taylor) modeling using the assumption that the emissive contact front is approximately located with the shock wave, resulting in the enhanced emission of the plume [17, 24, 61, 64]. In emissive plume contact front characterization, the Sedov-Taylor low limit is often used to partition fitting at early times, but the Sedov-Taylor high limit is often many

lengths further than the plume propagation stopping distance since the emissive contact front experiences drag in the background gas and slows to a stop [4, 5, 72]. The point where the emissive plume begins to slow in comparison to the shock wave is the shock detachment point [73, 74]. After the shock detachment occurs, the emissive contact front trajectory no longer follows a blast-like trajectory, and the Sedov-Taylor model is no longer sufficient to describe the propagation after this point. As a result, Sedov-Taylor fits to the emissive contact front beyond the shock detachment point will result in poorer estimates of the Sedov-Taylor blast energy and resulting laser-plume coupling efficiency. Very few studies have been conducted that compare the actual shock wave dynamics to the emissive plume contact front dynamics for PLA of graphite. No prior graphite studies were found that examine the dynamics of both the emissive plume contact front and the shock front in detail. In addition, no studies were found that examine shock detachment and its effects on the Sedov-Taylor modeling of emissive plumes.

This work focuses on the PLA of graphite, examining the location where the shock detaches from the plume emissive contact front by using emissive fast-gated imagery and schlieren shock wave imagery, and exploring the subsequent effects of limiting the upper portion of the Sedov-Taylor fit by the shock detachment point to improve the blast energy estimation. Free expansion, drag, and Sedov-Taylor models are used to quantify the propagation dynamics for the emissive plume contact front, and the Sedov-Taylor model is used to quantify the shock wave for comparison.

This research is part of a larger study focusing on the characterization of spatial and temporal dynamics of continuous wave and pulsed laser effects on graphite and carbon fiber targets [41, 84, 97].

## 4.2 Apparatus and Methodology

A Quantel EverGreen2 EVG00145 frequency-doubled Nd: YAG laser ( $\lambda = 532$  nm) used in single pulse mode with a 1 Hz repetition rate was used to deliver an average energy of 90 mJ per pulse onto a graphite target in a vacuum chamber backfilled with various gases and pressures as shown in Fig. 15. The laser energy was measured using an Ophir Nova II PE50BF-C detector positioned inside the target chamber. The spot size of the laser on the target was approximately circular with an area of  $1.578 \text{ mm}^2$ . The laser pulse has a full width half max of 12.5 ns and a rise time of 6.6 ns, yielding an intensity of  $0.456 \text{ GW/cm}^2$  and fluence of  $5.70 \text{ J/cm}^2$ . The ablation plume propagates normal to the target in the z-direction with a Princeton Instruments PIMAX 4 gated intensified charged-coupled device (ICCD) camera recording the shock wave and emissive plume in the xz-plane as shown in Fig. 16.

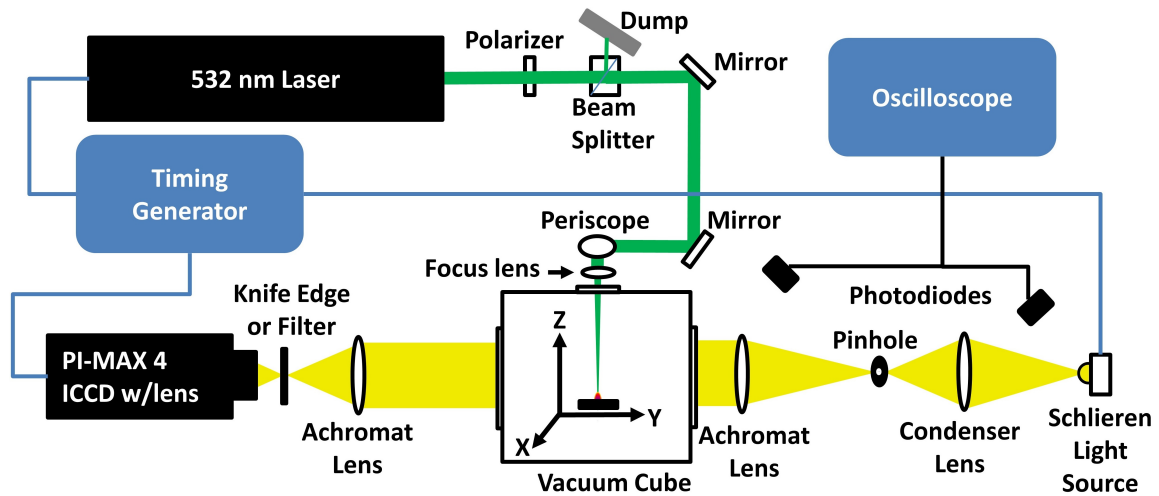


**Figure 15:** Schematic of the experimental apparatus which includes a vacuum chamber containing a sample target, PIMAX 4 ICCD camera, schlieren light source, and schlieren optics. The target is ablated using a Nd:YAG pulsed laser source ( $\lambda = 532$  nm, 12.5 ns pulse width, average energy 90 mJ per pulse at target).

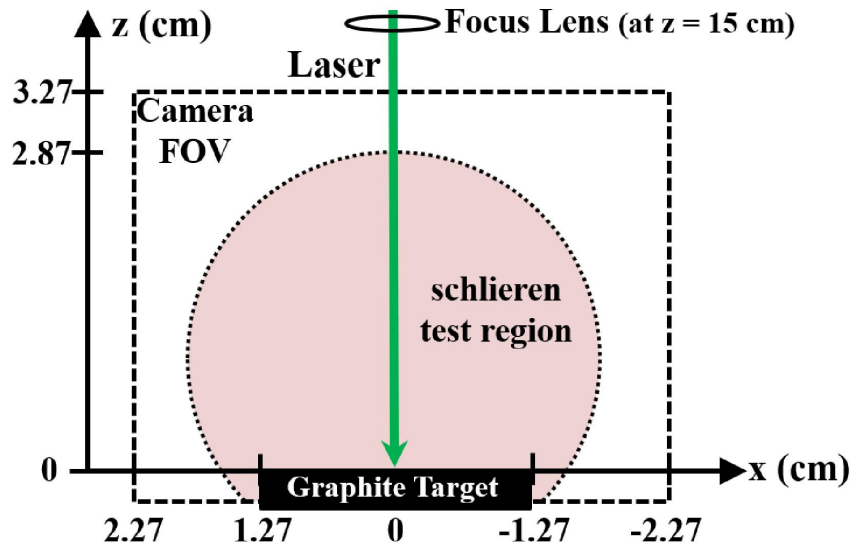


**Figure 16:** ICCD camera field of view. The ICCD camera views the  $xz$ -plane and images the shock wave and emissive plume propagation from the target out to a distance 2.81 cm from the target along the  $z$ -axis. The camera field of view is denoted by the dashed lines while the schlieren test region is denoted by the circular shaded area.

The laser was focused onto the target inside a 15.24 cm (6") modular vacuum cube through a vertical 3.8 cm diameter viewport. A 25.4 mm  $f = 150$  mm AR-coated plano-convex fused silica lens was used to focus the beam onto the target at an angle of incidence normal to the target. The targets were 25.4 mm diameter by 6.3 mm thickness pyrolytic graphite sputtering target discs (99.999% C) sourced from the Graphite Store with several thermodynamic properties previously determined by others as shown in Table 4. The chamber was evacuated to a pressure of  $10^{-3}$  Torr with a turbomolecular pump and then backfilled to 3–180 Torr of 99.999% nitrogen, argon, or a mixed gas of 70%  $\text{CO}_2$  and 30%  $\text{N}_2$ , at  $T = 298$  K. An MKS model 626 capacitance manometer with a 1000 Torr range was used to monitor pressure.

A white light fast-response LED from the University of Tennessee Space Institute was used as the schlieren light source. The LED was pulsed on for 30  $\mu\text{s}$  per laser shot to enable high intensity illumination and it was synchronized to overlap the full camera gate delay

**Table 4:** Properties of pyrolytic graphite samples.

Property	Value	Ref.
Density, $\rho$ (g/cm <sup>3</sup> )	2.2	[98]
Conductivity, $K$ (W/m·K) (across layers)	3.5	[98]
Conductivity, $K$ (W/m·K) (within layers)	400	[98]
Specific Heat, $C_p$ (J/kg·K) (T = 3500 K)	2135	[99]
Sublimation Temperature, T (K)	3923	[100]
Heat of Sublimation, $h_s$ (kJ/g)	61.3	[100]
Diffusivity, $\kappa$ (cm <sup>2</sup> /s)	0.0075	calculated
Diffusion length, $l_D$ (nm)	194	calculated
Ablation Threshold Fluence, $F_{th}$ (J/cm <sup>2</sup> )	1.29	calculated

period from 0 to 20  $\mu$ s. The LED exhibited several microseconds of rise before stabilizing to a steady intensity and the LED timing delay was set so that the steady intensity region overlapped the camera gate delay region. Since the LED light source was polychromatic, 50.8 mm spherical cemented achromatic doublet lenses were used for all schlieren optics. The LED light was collected and focused with an  $f = 75$  mm condenser lens onto an iris pinhole to create a pseudo-point source. The light was then collimated using an  $f = 300$  mm lens and the collimated light was passed horizontally along the y-axis through the vacuum chamber and target region through large 12.7 cm flat windows. The collimated light and plume emission was then focused with an  $f = 300$  mm lens onto a horizontally mounted razor blade as the schlieren knife-edge. A 50.8 mm 532 nm notch filter was used at the camera lens to protect the camera from oversaturation from pulse laser radiation.

A Princeton Instruments PI-MAX4 1024i with a 1024 x 1024 Gen III fast gate ICCD camera with a Nikon AF Nikkor 85 mm  $f/1.8$  lens was used to capture schlieren shock wave imagery and emissive imagery of the ablation event. The quantum efficiency of the 16-bit camera is higher than 15% from 430 to 880 nm, with a peak efficiency of approximately 31% near 650 nm. Saturation occurs at 65,536 counts with a dark signal of 600 counts. The field of view (FOV) of the lens was 4.55 by 4.55 cm with a circular schlieren-illuminated FOV of 3.17 cm by 2.85 cm and a resolution of 0.044 mm, or 44  $\mu$ m, per pixel.

Each schlieren test series consisted of two sets of 50 laser shots with corresponding images, one image per laser shot, and imagery were taken with fixed gate widths of 40 ns to improve signal and linearly varying time delays from 800 ns to 20  $\mu$ s. One image set was taken with the schlieren LED and pulsed laser on to capture the ablation shock wave, while the other set used only the schlieren LED to provide baseline or tare imagery. Each series was then repeated up to 10 times and the resulting schlieren images were averaged together by timestep to build a final time series of shock wave images. Tare imagery was averaged in a similar manner. The tare imagery was then subtracted from the schlieren shock wave imagery. For early plume times,  $t = 30\text{--}800$  ns, when the plume emission overwhelmed the white light schlieren signal, a Newport Velocity TLB-6712 tunable diode laser at 766 nm was used along with a 766 nm 10 nm FWHM bandpass filter to image the shock wave.

Emissive plume imagery was collected with linearly varied gate widths and delays with 3 ns gate widths at the start of the collection and 10 ns widths at the end of the collection to improve signal to noise when the plume emission significantly dimmed as it propagated away from the target surface. Emissive plume images began at the onset of the laser pulse (defined as  $t = 0$ ) and out to a delay of 1200 ns after the pulse. Each emissive plume series was repeated up to 4 times and the images at each time step were averaged together to account for shot-to-shot variations. Timing imagery was collected to verify laser pulse timing incidence on the target. All imagery was corrected for dark current background and flat fielded to correct for varying pixel intensity response. For initial velocities of 4 cm/ $\mu$ s, a 3 ns integration time yields a maximum of 116  $\mu$ m motion during image integration corresponding to 2.6 pixels. At late plume propagation times where the plume speed is reduced, a 10 ns gate width corresponds with a maximum motion of  $\sim 1$  pixel. Images exhibited  $< 1\%$  pulse-to-pulse laser flicker and  $< 2$  ns laser timing jitter. Shot-to-shot variation in laser pulse energy was  $< 1\%$ , and the laser energy on target was corrected as necessary using a polarizer and polarizing beam splitter to maintain the baseline.

The ICCD camera, schlieren light source, and pulsed laser were triggered using a Berkeley Nucleonics Corporation Model 577 pulse generator. A LeCroy WavePro 7300 3-GHz fast oscilloscope was used to monitor the gate signal from the PI-MAX 4 camera and signals from two ThorLabs DET10A silicon photodiodes observing the laser pulse and the white light LED pulse to verify experiment timing. Laser pulse rise time, pulse width, and intensity were also monitored with the oscilloscope using the photodiode.

### 4.3 Results

#### 4.3.1 Shock wave Propagation Imagery

A typical schlieren shock wave image at a delay of 7.9  $\mu\text{s}$  for a nitrogen background pressure of 10 Torr is shown in Fig. 17a. The image was taken with a gate width of 40 ns and has been processed with background and flat corrections in Fig. 17b to enhance the visibility of the shock wave. The shock front location is identified in Fig. 17c where a 5-pixel row average of the intensity is plotted along the center line of the plume and shock. The shock wave position is defined as the lowest point of the intensity profile, which occurs at  $z = 1.47$  cm in Fig. 17c and corresponds to a speed of 0.079 cm/ $\mu\text{s}$ . The shock exhibits a speed of 1.96 cm/ $\mu\text{s}$  in earlier frames. The speed of sound in the background nitrogen is 0.0353 cm/ $\mu\text{s}$ , yielding an initial Mach number of  $M \sim 55$  at  $t = 60$  ns, slowing to  $M \sim 1$  in later frames. A typical progression of processed schlieren shock front images for graphite ablation in 10 Torr nitrogen is shown in Fig. 18. The images span gate delays from 1.6  $\mu\text{s}$  to 17.3  $\mu\text{s}$  with the dark shock front nearly obscured by the emissive plume in the earliest image and then propagating outwards from the target in later images. Nitrogen, argon, and a mixture of 70%  $\text{CO}_2$  and 30%  $\text{N}_2$  ( $\text{CO}_2/\text{N}_2$ ) were chosen as the background gases due to similarity in mass. This choice allows for the exploration of the effects of pressure and mean free path as opposed to variations in momentum transfer.

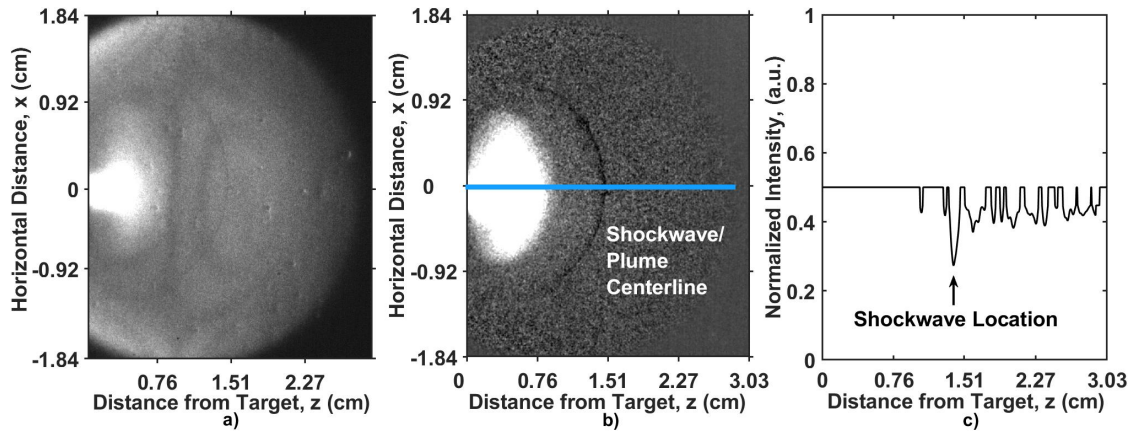


**Figure 17:** a) Unprocessed graphite ablation schlieren shock wave image for  $7.9 \mu\text{s}$  gate delay in nitrogen at 10 Torr with shock wave and plume visible in the LED illuminated region, b) Image processed with background and flat corrections, c) Centerline intensity profile with a 5-pixel (0.22 mm) row average with shock wave position approximately 1.5 cm from the target surface at  $t = 7.9 \mu\text{s}$ .

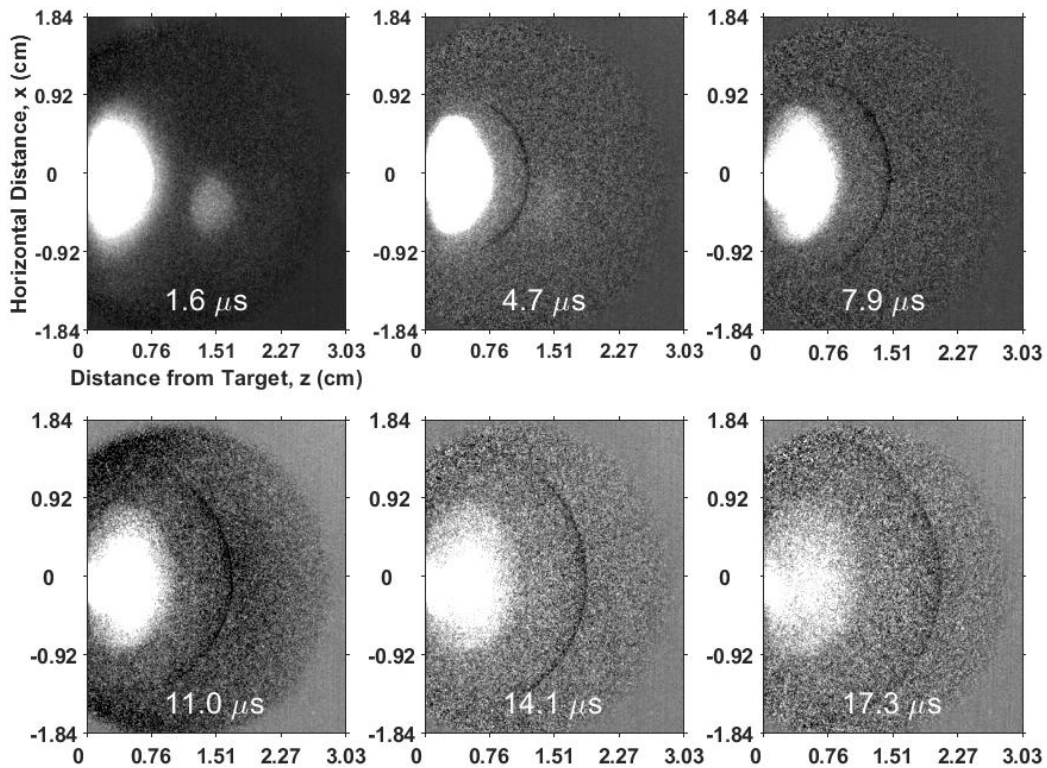


**Figure 18:** Schlieren shock wave image series for graphite in 10 Torr nitrogen from  $1.6 \mu\text{s}$  to  $17.3 \mu\text{s}$  after the laser pulse. Both the emissive plume and the shock wave (dark band) are visible in the early images with the emissive plume fading at later times.

Shock front trajectories and Mach numbers were characterized by plotting the shock

wave location for each camera gate delay as shown in Fig. 19. Instrumental limitations on identifying the shock front location are minimal. Experimentation with gate widths from 2.88 ns to 100 ns showed no discernible change in position or apparent thickness of the dark shock front shadow, and a 20 ns gate width was chosen to provide sufficient white light LED signal to noise to clearly define the shock front in the accumulated ICCD image. Positional uncertainty introduced by shock front motion during the gate width integration ranges from  $\sim 8.7$  pixels for the earliest times and shrink to less than 1 pixel at later times.

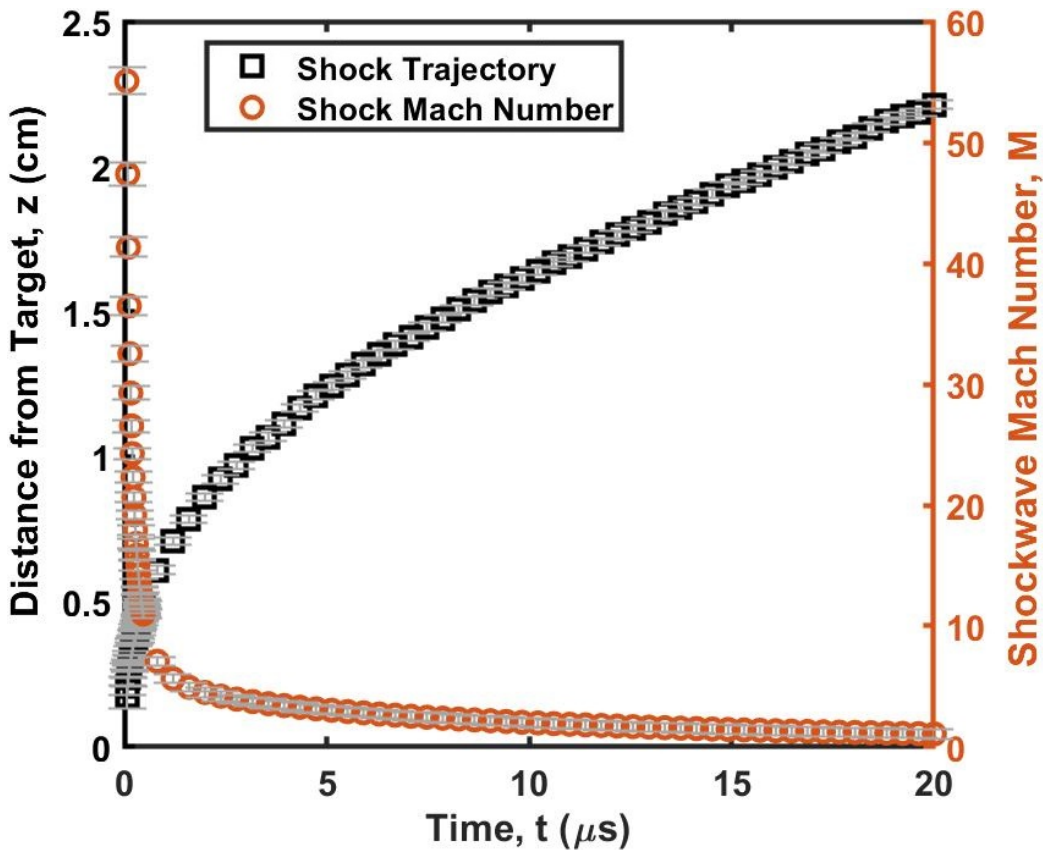


**Figure 19:** Shock wave trajectory and corresponding Mach numbers for graphite in a nitrogen background gas at 10 Torr. Gray vertical error bars for each series represent the  $z$  distance error and Mach error resulting from the ICCD 20 ns gate width.

Figure 20a shows shock trajectories for graphite in nitrogen gas at four pressures from 3 Torr to 180 Torr. As expected, the higher pressures exhibited shorter shock wave distances and lower shock speeds while lower pressures allowed for increased shock speed

and propagation distance away from the target surface. The long-time speeds of the shock trajectories for 10, 30, and 180 Torr were similar while the 3 Torr case exhibited a slightly greater speed. At the earliest times, the 3 Torr shock wave was still hidden by the emissive plume due to the plume extending a further distance into the lower density background gas. Shock trajectories for all the gas and pressure cases in this study can be seen in Fig. 20b. Argon and nitrogen showed similar shock trajectories at 10 and 30 Torr, while nitrogen and the  $\text{CO}_2/\text{N}_2$  mix exhibited similar trajectories at 180 Torr. The mixed gas consistently exhibited the lowest shock speeds for all pressures, with increasing separation of the trajectories from the nitrogen and argon cases as pressure was decreased. This is likely due to the  $\text{CO}_2/\text{N}_2$  gas mixture having the shortest mean free path among all the gases tested. Similarly, the trajectories for argon, which had the longest mean free path, consistently demonstrated faster speeds and distance traveled at all pressures. There was also significant separation of shock speeds between all three gases at 3 Torr with nitrogen and  $\text{CO}_2/\text{N}_2$  exhibiting similar speeds while argon propagated through the background gas more quickly.

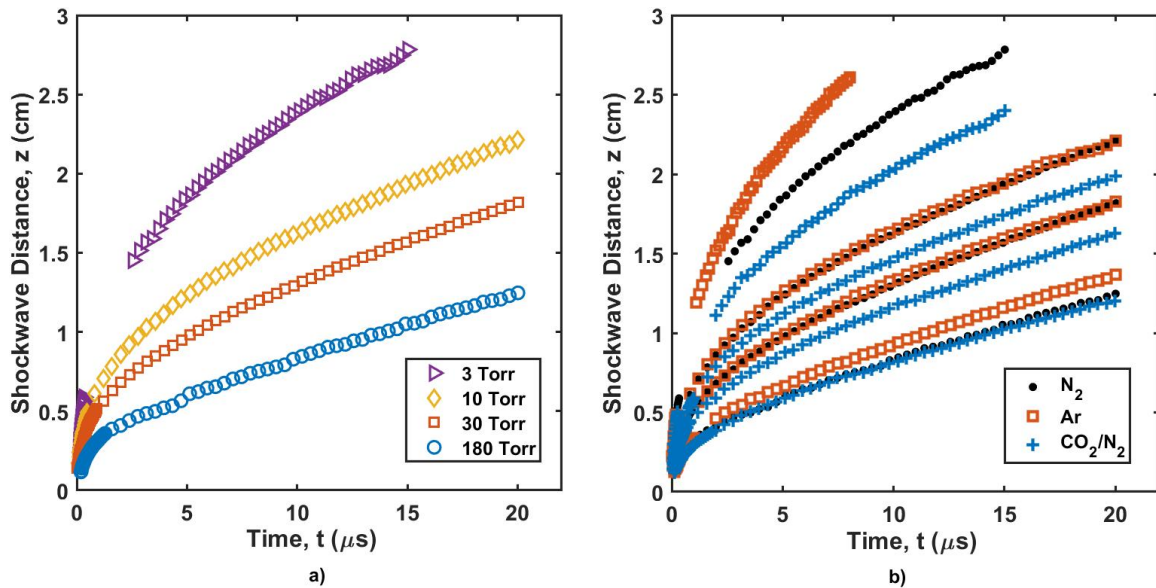


**Figure 20:** a) Shock wave trajectories for graphite in nitrogen gas at 3–180 Torr, b) Shock wave trajectories for graphite in nitrogen, argon, and  $\text{CO}_2/\text{N}_2$  for background pressures of 3–180 Torr.

### 4.3.2 Emissive Contact Front Imagery and Propagation

A typical emissive plume image at a delay of 175.2 ns for a nitrogen background pressure of 10 Torr is shown as an intensity contour plot in Fig. 21a. The leading edge of the plume is located at 0.312 cm, corresponding to an average speed of 0.71 cm/ $\mu$ s. Most of the emission occurs near the shock front, with minimal emission from the plume interior.

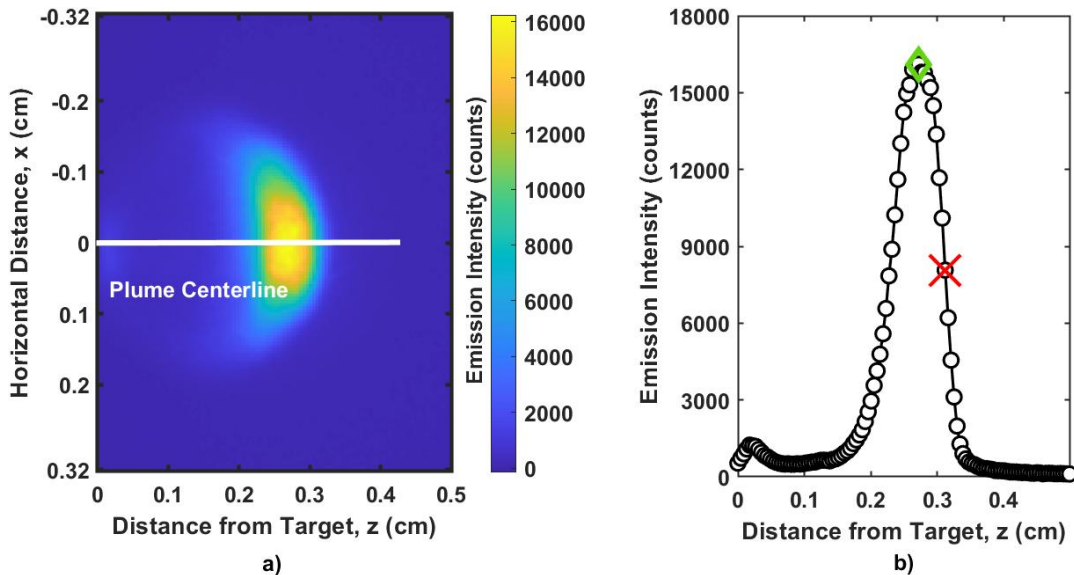


**Figure 21:** a) Graphite ablation plume ICCD image with 175.2 ns gate delay in nitrogen at 10 Torr, b) Centerline intensity profile with a 5-pixel (0.22 mm) row average corresponding to the image in Fig. 21a with peak intensity and defined contact front position at 50% peak intensity for  $t = 175.2$  ns in nitrogen at 10 Torr.

The plume emissive contact front location is identified in Fig. 21b where a 5-pixel row average of the emission intensity is plotted along the center line of the plume. The leading edge of emission is identified where the intensity rises to 50% of the peak at  $z = 0.312$  cm. Plume emissive contact front trajectories for 3–180 Torr were characterized by locating the contact front location for each camera gate delay as shown in Fig. 22a. The plume data was taken with 50 datapoints for the first 150 ns of propagation to capture early plume dynamics with higher resolution, and then additional datapoints were taken for later plume expansion times to capture overall plume propagation. The gate width was fixed at 2.88 ns.

Instrumental limitations on identifying the shock location are minimal, with positional error corresponding to the gate width transit distance typically less than curvature in the trajectory. Positional errors introduced by plume motion during the gate width integration time amounts to  $\sim 1.98$  pixels for the earliest times and 0.3 pixels at later times, due to the slowing of the plume in the background gas.

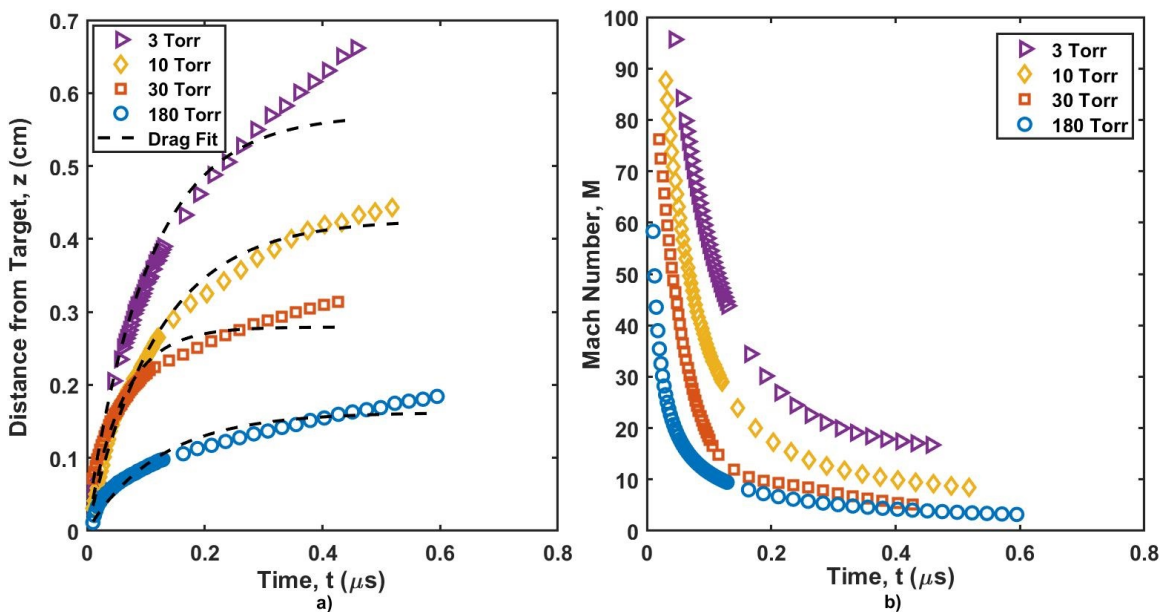


**Figure 22:** a) Emissive plume contact front trajectory for graphite in a nitrogen background gas at 3–180 Torr. Drag model fits are represented by dashed lines, b) Emissive plume contact front Mach numbers for graphite in a nitrogen background gas at 3–180 Torr.

Mach numbers for the emissive plume contact front in 3–180 Torr nitrogen are displayed in Fig. 22b. The plume in 10 Torr nitrogen has an initial speed of  $3.06 \text{ cm}/\mu\text{s}$ . Using a speed of sound of  $0.0353 \text{ cm}/\mu\text{s}$  in nitrogen yields an initial Mach number of  $M \sim 87$  slowing to  $M \sim 6.8$  for 10 Torr. At  $t = 60 \text{ ns}$ , the plume is traveling at  $M \sim 54$ . As expected, the lowest pressure case of 3 Torr exhibited the highest starting Mach number,  $M \sim 97$ , falling to  $M \sim 16$  at later times. The 30 Torr case exhibited a starting Mach number of  $M \sim 76$ , falling to  $M \sim 5$  at later times. The 180 Torr case showed the smallest starting Mach number,  $M \sim 58$ , falling to  $M \sim 3$  at later times. The velocities and Mach numbers seen in this study were significantly higher than previous studies in other materials and in

the study presented in Chapter 3. In Chapter 3, Mach numbers up to  $M \sim 55$  were observed for graphite plumes in nitrogen at 1 Torr using a 248 nm excimer laser, and Bauer et. al. [72] observed  $M \sim 34$  for titanium plumes in argon at 500 mTorr using a 248 nm excimer laser. However, velocities and Mach numbers for several other graphite studies were consistent with the current results: Roberts et. al. [91] observed graphite plumes with  $M \sim 70$  in argon at 1 Torr using a 248 nm excimer laser at  $17 \text{ J/cm}^2$ , and Singh et. al. [64] observed  $M \sim 40$  for graphite plumes in nitrogen at 760 Torr using a 1064 nm doubled Nd: YAG laser at  $160 \text{ J/cm}^2$ . Increased inverse-Bremsstrahlung coupling between the graphite plume and the ablation laser could explain the higher Mach numbers observed in this work, which is supported by the findings of Hussein et. al. [50] who found that inverse-Bremsstrahlung coupling efficiency increased with increasing wavelength.

At very early times, the ablated plume material has not yet interacted with the background gas, and a free expansion model was used to characterize the initial velocity of the plume trajectory [52]. The free expansion was characterized by Eq. 7 in Sec. 3.2. Data sectioning for the free expansion fits was limited to the first  $\sim 20$  data points corresponding to the first 60 ns of plume propagation where there was no trajectory curvature from collisions with the gas background. The very small intercept,  $z_o = 0.0024 \pm 0.0019 \text{ cm}$  corresponds to a time interval  $\sim 1 \text{ ns}$ . The initial velocity for the plume propagating in nitrogen at 10 Torr is  $v_o = 3.06 \pm 0.1 \text{ cm}/\mu\text{s}$ , corresponding to a kinetic energy of  $58.3 \pm 4 \text{ eV}$  per carbon atom. The greatest free expansion kinetic energy was  $73.9 \pm 3.8 \text{ eV}$  in 3 Torr nitrogen, while the lowest kinetic energy was  $22.5 \pm 3.1 \text{ eV}$  in 180 Torr  $\text{CO}_2/\text{N}_2$ . Kinetic energies for all test cases are reported in Table 5. The kinetic energy with the smallest uncertainty was  $50.6 \pm 2.1 \text{ eV}$ , found in the 10 Torr  $\text{CO}_2/\text{N}_2$  case. Plume kinetic energies were 10–30 times larger than the 2.34 eV laser photon energy, suggesting significant plume interaction with the 532 nm laser pulse.

Contrary to the assumption that the free expansion would not be influenced by the

**Table 5:** Free expansion velocity and kinetic energy for the emissive plume.

Gas	Pressure (Torr)	$v_0$ (cm/ $\mu$ s)	Kinetic Energy (eV)
N <sub>2</sub>	180	$2.08 \pm 0.20$	$26.9 \pm 5.2$
N <sub>2</sub>	30	$2.80 \pm 0.15$	$48.8 \pm 5.2$
N <sub>2</sub>	10	$3.06 \pm 0.10$	$58.3 \pm 3.8$
N <sub>2</sub>	3	$3.45 \pm 0.10$	$74.1 \pm 4.3$
Ar	180	$1.90 \pm 0.14$	$22.5 \pm 3.3$
Ar	30	$2.56 \pm 0.12$	$40.8 \pm 3.8$
Ar	10	$2.85 \pm 0.06$	$50.6 \pm 2.1$
Ar	3	$3.41 \pm 0.08$	$72.4 \pm 3.4$
CO <sub>2</sub> /N <sub>2</sub>	180	$2.04 \pm 0.20$	$25.9 \pm 5.1$
CO <sub>2</sub> /N <sub>2</sub>	30	$2.62 \pm 0.16$	$42.7 \pm 5.2$
CO <sub>2</sub> /N <sub>2</sub>	10	$2.90 \pm 0.09$	$52.3 \pm 3.2$
CO <sub>2</sub> /N <sub>2</sub>	3	$3.36 \pm 0.12$	$70.3 \pm 5.1$

background gas, a higher initial speed is observed in the lighter nitrogen gas. The highest speed was observed for the lower pressure 3 Torr case. This is consistent with the study in Chapter 3 with helium at 10 Torr at a lower fluence of  $4 \text{ J/cm}^2$  with a KrF laser at 248 nm, and with another study of PLA of graphite in 300 Torr xenon and helium gas backgrounds at a higher fluence of  $20 \text{ J/cm}^2$  [61]. These results are interesting in that one would expect that the increased plume confinement at higher pressures would lead to an increase in the carbon kinetic energy through the inverse-Bremsstrahlung process as more of the plume is able to interact with the laser. However, increased plume shielding and laser-plume coupling will also lead to a decrease in mass ablated as fewer laser photons are able to reach the target surface. A previous study found that laser coupling to the plume and the target decreased at higher pressures [54]. This would lead to lower kinetic energies and less ablated mass, and is likely due to the plume becoming opaque to the laser as the plasma scatters the laser energy away from the plume surface and the target. As a result, free expansion velocity fitting and subsequent kinetic energy calculation are somewhat oversimplified as plume diagnostics. Another issue is that the free expansion fitting is conducted at very early times

in the propagation, and the trajectories are typically tracked using the forward emissive contact front only. There is evidence that plume splitting can occur with both faster and slower plume components propagating away from the target after the ablation [120]. This could bias standard free expansion measurements depending on which plume component is being used to create the trajectory for analysis. Plume splitting was not evident in the imagery for this study.

The 3 Torr cases also exhibit similar free expansion velocities for all three gases, and this could reflect similar laser-plume coupling at that pressure due to the similarity in mass of the background gases. Hussein et. al. found that inverse-Bremsstrahlung coupling increased with longer wavelengths [50]. With increased inverse-Bremsstrahlung coupling at 532 nm compared to 248 nm ablation in Chapter 3, a greater fraction of the laser pulse energy is being used to accelerate each carbon atom, resulting in higher plume velocities. In addition, the fluence in this work is 4.5 times the ablation threshold, while the fluence in Chapter 3 was  $\sim 2$  times ablation threshold, and as a result there is more energy per unit area of the laser available for coupling with the plume, resulting in an increase in plume velocity.

The shock front and emissive plume were characterized using the Sedov-Taylor (ST) scaling first developed for bomb detonations [4, 5, 61, 104]. As in Chapter 3, a more generalized form [121] of the shock trajectory is utilized than is typically employed for laser ablation. The general form allows for variation in shock/plume dimensionality and a finite laser pulse duration, as follows:

$$z(t) = at^b, \quad (23)$$

where

$$a = \xi_n \left( \frac{E_{ST} / (\tau_o^s l_o^{3-n})}{\rho} \right)^{1/(n+2)}, \quad (24)$$

$$b = (s + 2)/(n + 2). \quad (25)$$

In Eq. 24 and Eq. 25,  $E_{ST}$  is the ST energy,  $\tau_0$  is the laser pulse duration,  $l_o$  is the length scale,  $n$  is the dimensionality factor,  $s$  is the energy release ( $s = 0$  for instantaneous release,  $s = 1$  for a constant release with rate  $E_{ST}/\tau_0$ ),  $\rho$  is the background gas density, and  $\xi_n \approx 1$  depending on the ratio of specific heats of the background gas and the dimensionality factor  $n$  [4, 5, 121]. Energy deposition is assumed to be instantaneous for laser ablation, which is appropriate when the plume evolution time is long relative to the laser pulse duration. The dimensionality factor is often constrained to  $n = 3$  in laser ablation studies, corresponding to a spherical shock front [75, 85, 105]. The length scale,  $l_o$ , is not relevant for the spherical case of dimensionality, but becomes important for dimensionality less than  $n = 3$ . It is important to note that plume dimensionality is a function of time and can vary depending on how much of the plume trajectory is used for the fit: the plume trajectory fit yields an average dimensionality value over the included data. Plume dimensionality can depend on the laser spot: with a rectangular laser spot, the plume may appear nearly one dimensional,  $n \approx 1$ , with a planar shock front at early times, and later evolve to more spherical dimensionality at later times [56]. Recent studies indicate a dimensionality that decreases with increasing background density,  $\rho$ , and this was supported by the study in Chapter 3 as well [72]. Equation 23 is employed with the average dimensionality  $n$  and the  $a$ -coefficient as fit parameters, constrained to instantaneous energy release,  $s = 0$ , and ST low limit given in Eq. 26 is used as the length scale for determining ST energies from the plume and shock wave trajectory data.

The ST model is applicable in the range:

$$z_{low} = \left( \frac{3m_a}{2\pi\rho} \right)^{\frac{1}{3}} \ll z \ll \left( \frac{2E_a}{P_b} \right)^{\frac{1}{3}} = z_{high}, \quad (26)$$

where  $m_a$  is the mass ablated from the target,  $\rho$  is the background gas density,  $E_a$  is the

ablation energy from the laser, and  $P_b$  is the background gas pressure [104]. The ST model is valid when the mass displaced by the shock front is larger than the mass inside the plume and when pressure behind the shock front is still very large compared to background gas pressure. The ST low limit for the 10 Torr nitrogen case was  $z_{low} = 0.176 \pm 0.003$  cm ( $\sim 40$  pixels) and the high limit is beyond the ICCD camera field of view. When fitting the observed shock and emissive plume contact front trajectories to Eq. 23, the data is sectioned to  $z > z_{low}$ . The ST model was used to estimate the energy,  $E_{ST}$ , that goes into the shock wave in the initial ablation event, and the results are summarized for the shock wave and the emissive contact front in Table 7 and discussed in Section 4.4.2.

The emissive plume was also characterized by the drag model. The emissive plume expansion is dominated by drag at later times as the expanding plume collides with the background gas and slows, resulting in the decrease in collisional excitation of emitting states. The slowing of the emissive plume results in the detachment of the shock wave from the emissive plume contact front. The empirical drag model exponentially approaches the stopping distance and is given as:

$$z(t) = z_s \left(1 - e^{-\beta t}\right) + z_o \quad (27)$$

where  $z_s$  is the plume stopping distance and  $\beta$  is the drag coefficient [106, 107]. As with the free expansion fit, an intercept term,  $z_o = 0.0021 \pm 0.003$  cm, was found for the drag fit to account for experimental timing uncertainty. The drag fits to the plume trajectories for the various pressures in nitrogen are provided in Fig. 22a above. The emissive plume drag fits are utilized in the shock detachment analysis in Section 4.4.1.

## 4.4 Discussion

### 4.4.1 Shock Detachment from Emissive Plume

Shock detachment is the point where the emissive contact front and shock wave trajectories begin to diverge. The emissive plume slows while encountering drag from the background gas and eventually reaches a stopping distance, whereas the shock wave continues its overall trajectory approaching  $M = 1$  at long distances. Up until the shock detachment point, the emissive contact front and plume trajectories are expected to be similar and can be modeled using the Sedov-Taylor blast model. After shock detachment from the emissive plume, the emissive plume becomes more drag-like while the shock wave continues along a Sedov-Taylor trajectory. As a result, the Sedov-Taylor model is no longer valid for the emissive contact front after the shock detachment, and including post-detachment plume data in ST fits will bias the plume ST fit results and laser-plume energy calculations.

Determining the appropriate high cutoff point for emissive plume modeling is important to ensure accurate fit results when shock wave data is unavailable. In order to determine the shock detachment point, the schlieren shock wave trajectory Sedov-Taylor model fits are utilized in conjunction with the emissive plume contact front drag model fits. The point of shock detachment is defined here as the intercept point,  $z_D$ , between the two expansion model fits for the shock wave and plume trajectories. In several cases there was a small difference between the model crossing point and the point where the plume data diverged from the shock wave data, however, the difference was within the error bounds for shock detachment distance. Figure 23a shows the Sedov-Taylor fit to a graphite shock wave in nitrogen at 10 Torr with data sectioned to beyond the low limit at  $z_{low} = 0.176 \pm 0.003$  cm. Unlike an emissive plume ST fit that typically overestimates the trajectory at early time and underestimates at late time with significant residuals, the ST fit to the schlieren shock wave trajectory is extremely good out to very long times on the order of 20  $\mu$ s. The shock wave

ST trajectory is compared to the emissive plume drag trajectory in Fig. 23b. The resulting shock detachment point occurs at  $z_D = 0.39 \pm 0.05$  cm. The shock detachment points for all test cases are given in Table 6.

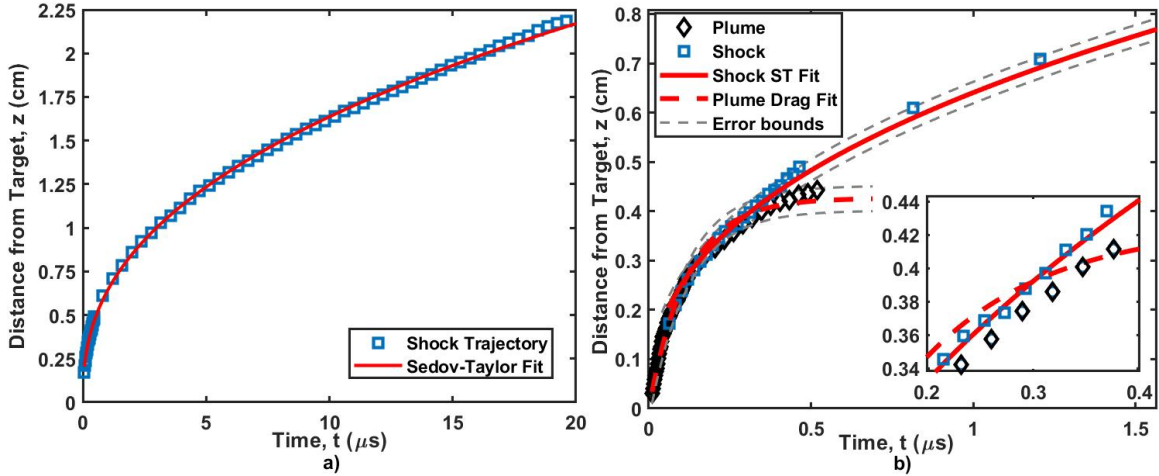


**Figure 23:** a) Sedov-Taylor fit to shock wave trajectory of graphite in a nitrogen background gas at 10 Torr with the fit extending to the Sedov-Taylor low limit  $z_{low} = 0.176 \pm 0.003$  cm, b) Expanded view of shock detachment between emissive contact front and shock wave for graphite in a nitrogen background gas at 10 Torr along with a zoomed inset of the detachment point. The shock detachment point,  $z_D = 0.39 \pm 0.05$  cm, occurs near the crossing point of the shock wave ST fit and emissive contact front drag fit. 95% confidence intervals for the ST and drag fits are provided.

As expected, shock detachment occurs closer to the target surface as pressure is increased. The ablation plume in  $\text{CO}_2/\text{N}_2$  exhibited the smallest shock detachment distance of  $0.12 \pm 0.03$  cm from the target surface, while a plume in 3 Torr argon had the largest shock detachment of  $0.65 \pm 0.03$  cm.

**Table 6:** Shock Detachment locations for graphite ablation in N<sub>2</sub>, Ar, and 70% CO<sub>2</sub> 30% N<sub>2</sub> gases from 3–180 Torr.

Gas	Pressure (Torr)	Shock Detachment Location, $z_D$ (cm)
N <sub>2</sub>	180	$0.13 \pm 0.03$
N <sub>2</sub>	30	$0.27 \pm 0.05$
N <sub>2</sub>	10	$0.39 \pm 0.05$
N <sub>2</sub>	3	$0.52 \pm 0.06$
Ar	180	$0.14 \pm 0.02$
Ar	30	$0.31 \pm 0.05$
Ar	10	$0.41 \pm 0.06$
Ar	3	$0.65 \pm 0.10$
CO <sub>2</sub> /N <sub>2</sub>	180	$0.12 \pm 0.03$
CO <sub>2</sub> /N <sub>2</sub>	30	$0.22 \pm 0.05$
CO <sub>2</sub> /N <sub>2</sub>	10	$0.36 \pm 0.05$
CO <sub>2</sub> /N <sub>2</sub>	3	$0.42 \pm 0.13$

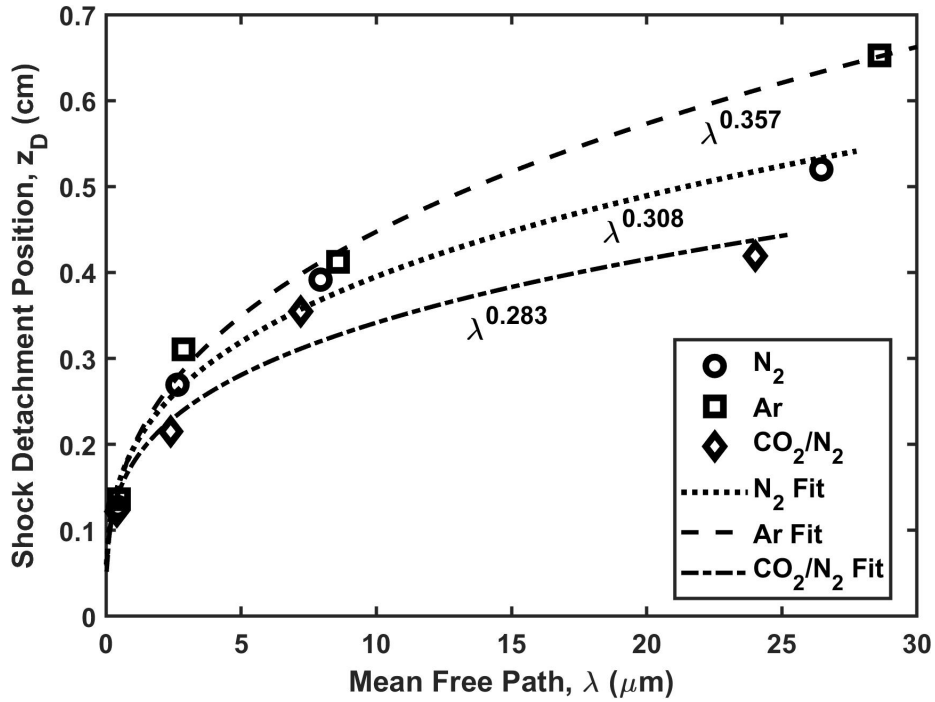


**Figure 24:** Shock detachment compared to mean free path in nitrogen, argon, and CO<sub>2</sub>/N<sub>2</sub> for background pressures of 3–180 Torr along with power law fit curves. Fit exponents are 0.357 for Ar, 0.308 for N<sub>2</sub>, and 0.283 for 70% CO<sub>2</sub> 30% N<sub>2</sub>.

Figure 24 displays the shock detachment distance as compared to mean free path (MFP),

$\lambda$ , for nitrogen, argon, and CO<sub>2</sub>/N<sub>2</sub> at pressures ranging from 3–180 Torr. MFP collision cross sections used in calculations for graphite in the background gases are 0.327 nm<sup>2</sup> in N<sub>2</sub>, 0.317 nm<sup>2</sup> in Ar, and 0.397 nm<sup>2</sup> for CO<sub>2</sub>. The variation of MFP between the three background gases is clear in Fig. 24, with longer MFP typically resulting in an increase in shock detachment position. Argon exhibits the furthest shock detachment position corresponding to the longest MFP. These longer shock detachment points correspond with the lowest pressure 3 Torr cases. In Fig. 24, the longest MFP cases exhibit a wider shock detachment spread than the shortest MFP cases at 180 Torr. The shock detachment point versus MFP for a given gas appears to follow a fractional power law in all cases, with exponent fit coefficients as follows: 0.357 for Ar, 0.308 for N<sub>2</sub>, and 0.283 for CO<sub>2</sub>/N<sub>2</sub>.

#### **4.4.2 Sedov-Taylor Blast Energy Comparison: Shock wave and Emissive Contact Front**

Shock detachment is critical in the estimation Sedov-Taylor blast energy, which gives an estimate of laser-shock efficiency, or the energy coupled from the laser into the plume. An improved understanding of where shock detachment occurs between the emissive contact front and the shock wave can allow for better partitioning of emissive plume trajectories for Sedov-Taylor model fitting and subsequent plume energy estimations. In this section, the shock wave and emissive contact front trajectories are analyzed with Sedov-Taylor modeling and then the shock detachment point data is used to inform improved plume contact front data sectioning to exclude the portion of the plume trajectory after the shock has detached.

Table 7 (upper) gives the Sedov-Taylor fit results and blast wave energies for the graphite ablation schlieren-imaged shock waves in the various gas and pressure test cases. Values for shock wave dimensionality and a-coefficient as fit parameters to Eq. 23 are provided, and Sedov-Taylor blast energy values for both varying and constrained dimensionality  $n$

are provided. For cases with  $n \neq 3$ , an estimate of the length scale,  $l_0$  is required. As in Chapter 3, a length scale is chosen as  $l_o = z_{low} = (3m_a/2\pi\rho)^{\frac{1}{3}}$ , which has been found previously to be suitable [121]. Using this length scale for the ablation in the nitrogen yields a blast energy  $E_{ST} = 72 \pm 2$  mJ or 80% of the laser pulse energy of 90 mJ coupled into the shock wave.

Shock wave dimensionality in the present data generally trends towards  $n = 3$  at the lower pressure cases and becomes less spherical as pressure increases. The circular laser spot is expected to result in an initially spherical shock wave that becomes somewhat less spherical as it expands into the surrounding background gas, especially at higher pressures. The 180 Torr cases exhibited dimensionality values between  $2.35 \pm 0.06$  for argon, and  $2.44 \pm 0.08$  for nitrogen. At 3 Torr, the Sedov-Taylor model fitting overestimates dimensionality for  $\text{CO}_2/\text{N}_2$ , giving  $n = 3.24 \pm 0.05$ . Across the gases and pressures tested in this study, the blast energy and the laser-shock wave coupling efficiency drop as pressure increases. At 180 Torr,  $\text{CO}_2/\text{N}_2$  and nitrogen exhibit nearly the same blast energy at  $E_{ST} \sim 18$  mJ, while the 10 Torr cases in all three gases yield  $E_{ST} \sim 72\text{--}83$  mJ. When the dimensionality constant is constrained to  $n = 3$ , the Sedov-Taylor model appears to significantly overestimate blast energy, especially at higher pressures. For all 3 Torr cases with both fixed and dynamic dimensionality  $n$ , blast energy was significantly overestimated by the Sedov-Taylor model with calculated energies ranging from 2–5 times the total energy of the laser pulse. This is most likely due to increased positional error of the identified shock wave locations at 3 Torr, which tended to be extremely faint in the schlieren imagery and more difficult for the shock tracking algorithm to track due to the low signal to noise ratio of the schlieren at those pressures.

Table 7 (lower) gives the Sedov-Taylor fit results and blast energies for the plume emissive contact front, also using the low limit to partition the fits. Graphite ablation in 10 Torr nitrogen yields a blast energy  $E_{ST} = 54 \pm 6$  mJ or 60% of the laser pulse energy coupled

**Table 7:** Sedov-Taylor fit results for schlieren shock wave and emissive plume in N<sub>2</sub>, Ar, and 70% CO<sub>2</sub> 30% N<sub>2</sub> gases.

Case	Gas	P (Torr)	Sedov-Taylor			Sedov-Taylor $n = 3$	
			$z(t) = at^{\frac{2}{n+2}}$	$z(t) = at^{0.4}$	$n$	$a$ (cm/ $\mu$ s <sup>2/(n+2)</sup> )	ST Energy, $E_{ST}$ (mJ)
Shock	N <sub>2</sub>	180	2.44 ± 0.08	0.304 ± 0.006	18 ± 1	0.336 ± 0.004	58 ± 4
	N <sub>2</sub>	30	2.92 ± 0.05	0.518 ± 0.005	75 ± 3	0.525 ± 0.002	90 ± 2
	N <sub>2</sub>	10	2.91 ± 0.03	0.641 ± 0.004	72 ± 2	0.651 ± 0.002	88 ± 1
	N <sub>2</sub>	3	3.02 ± 0.09	0.957 ± 0.014	184 ± 14	0.954 ± 0.004	178 ± 4
	Ar	180	2.35 ± 0.06	0.330 ± 0.005	31 ± 2	0.374 ± 0.005	141 ± 9
	Ar	30	2.64 ± 0.04	0.495 ± 0.004	59 ± 2	0.532 ± 0.003	136 ± 4
	Ar	10	2.86 ± 0.03	0.630 ± 0.004	88 ± 3	0.659 ± 0.002	132 ± 2
	Ar	3	2.83 ± 0.10	1.114 ± 0.015	419 ± 28	1.137 ± 0.006	609 ± 16
	CO <sub>2</sub> /N <sub>2</sub>	180	2.35 ± 0.06	0.290 ± 0.004	17 ± 1	0.329 ± 0.004	73 ± 5
	CO <sub>2</sub> /N <sub>2</sub>	30	2.87 ± 0.06	0.457 ± 0.005	53 ± 3	0.468 ± 0.002	71 ± 2
	CO <sub>2</sub> /N <sub>2</sub>	10	2.98 ± 0.03	0.586 ± 0.003	71 ± 2	0.588 ± 0.001	74 ± 1
	CO <sub>2</sub> /N <sub>2</sub>	3	3.24 ± 0.05	0.844 ± 0.006	183 ± 7	0.813 ± 0.003	112 ± 2
	Plume	N <sub>2</sub>	180	3.46 ± 0.08	0.219 ± 0.003	7 ± 0.1	0.220 ± 0.001
N <sub>2</sub>		30	3.12 ± 0.21	0.528 ± 0.022	109 ± 23	0.525 ± 0.002	90 ± 2
N <sub>2</sub>		10	2.92 ± 0.16	0.602 ± 0.013	54 ± 6	0.597 ± 0.006	57 ± 3
N <sub>2</sub>		3	2.37 ± 0.10	0.967 ± 0.018	81 ± 7	0.835 ± 0.012	91 ± 6
Ar		180	3.07 ± 0.04	0.297 ± 0.002	48 ± 2	0.300 ± 0.003	47 ± 0.3
Ar		30	2.82 ± 0.12	0.463 ± 0.008	54 ± 4	0.453 ± 0.004	61 ± 2
Ar		10	2.59 ± 0.09	0.633 ± 0.010	63 ± 4	0.598 ± 0.006	73 ± 4
Ar		3	2.10 ± 0.08	1.076 ± 0.016	114 ± 7	0.955 ± 0.023	254 ± 31
CO <sub>2</sub> /N <sub>2</sub>		180	3.06 ± 0.09	0.266 ± 0.008	27 ± 4	0.293 ± 0.006	41 ± 4
CO <sub>2</sub> /N <sub>2</sub>		30	3.03 ± 0.16	0.457 ± 0.014	65 ± 10	0.459 ± 0.002	64 ± 1
CO <sub>2</sub> /N <sub>2</sub>		10	2.98 ± 0.21	0.578 ± 0.022	66 ± 12	0.576 ± 0.005	60 ± 2
CO <sub>2</sub> /N <sub>2</sub>		3	1.99 ± 0.12	0.939 ± 0.029	55 ± 7	0.763 ± 0.013	81 ± 7

into the plume, about 20% less coupling efficiency than the schlieren shock wave at the same conditions. Unlike the shock wave, plume contact front dimensionality in the data generally trends towards  $n = 3$  for the higher pressure cases and becomes less spherical as pressure decreases. The 180 Torr cases exhibit dimensionality that approaches spherical with  $n = 3.07 \pm 0.04$  for argon, and  $n = 3.06 \pm 0.09$  for  $\text{CO}_2/\text{N}_2$ . At 3 Torr, the Sedov-Taylor model fitting yields  $n = 1.99 \pm 0.12$  for  $\text{CO}_2/\text{N}_2$  and  $n = 2.37 \pm 0.10$  for nitrogen. Similar to the shock wave data, the blast energy and laser-shock wave coupling efficiency drop for the emissive plume as pressure increases. The 10 Torr cases in all three gases yield  $E_{ST} \sim 54\text{--}66$  mJ. The blast energies given by the emissive contact front fits are consistently lower than those of the shock wave fits.

With the dimensionality constant constrained to  $n = 3$ , the Sedov-Taylor model also appears to significantly overestimate blast energy, especially at higher pressures. The only case where blast energy was significantly overestimated by the Sedov-Taylor model was 3 Torr argon as the 30 Torr nitrogen energy error bound falls within the laser pulse energy. For the fixed  $n$  cases, the Sedov-Taylor model still results in increased energy estimations compared to the dynamic dimensionality cases, however, the magnitudes of the energy differences are less than those encountered in the shock wave analysis. From the dimensionality of the emissive contact fronts, it appears that the plumes exhibit more cylindrical dimensionality at lower pressures and increase to more spherical dimensionality at greater pressures. Similarly, the dimensionality in heavier gases tends to be more spherical compared to the lighter gases, which is a trend seen in Chapter 3 as well.

Unlike the previous analyses where the emissive contact front data was only partitioned using the Sedov-Taylor low limit, the shock detachment points found in Section 4.4.1 are used to provide an upper bound to fit the Sedov-Taylor model and estimate laser-plume coupling energies. The results of the detachment point-limited fits are compared in Fig. 25, which includes Sedov-Taylor energy in Fig. 25a and dimensionality in Fig. 25b for the

emissive plumes and the shock waves. The Sedov-Taylor energies are compared in Table 8 as well. Apart from the 3 Torr cases, the emissive contact front energies fall within 3–20 mJ of the shock wave energy estimates. Several cases including 180 and 30 Torr nitrogen exhibit only 3 mJ difference between the shock detachment-limited emissive plume results and the shock wave results. Clearly, fit partitioning of the emissive contact front plumes using the shock detachment points improves the Sedov-Taylor fits and subsequent blast energy calculations, resulting in a more accurate estimation of the energy deposited in the ablation plume by the ablation laser which directly impacts the dynamics of the emissive plume.

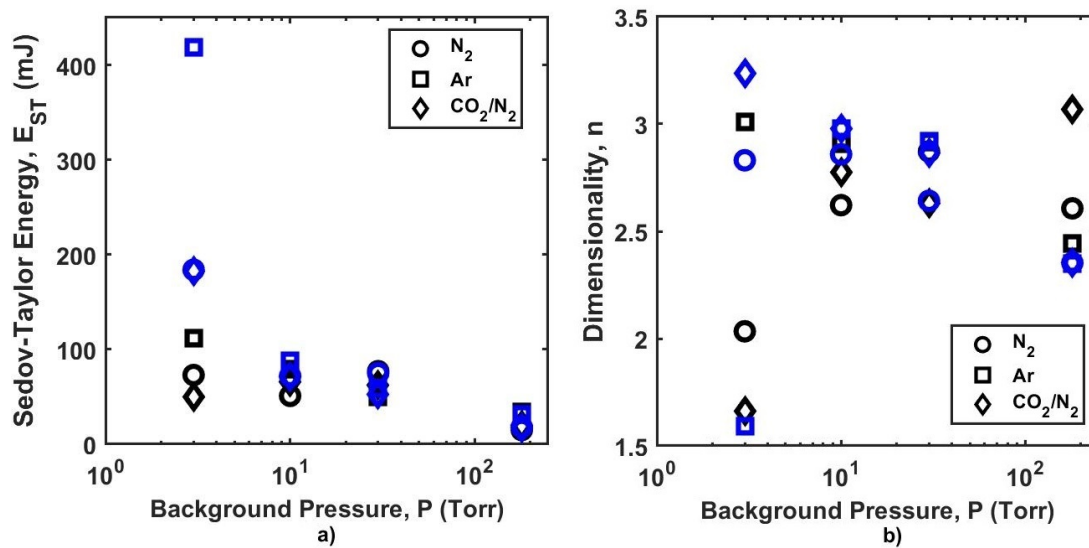


**Figure 25:** a) Sedov-Taylor energy,  $E_{ST}$ , and b) dimensionality,  $n$ , for shock detachment-limited emissive plume (black markers) and schlieren-imaged shock wave (blue markers) for 3–180 Torr in N<sub>2</sub>, Ar, and CO<sub>2</sub>/N<sub>2</sub>.

Although the Sedov-Taylor analysis of laser ablation plumes and shock waves is useful for characterizing plume dynamics and laser-plume energy transfer, ST is not a full replacement for detailed computational fluid dynamics calculations. The outcome of a ST energy analysis is significantly influenced by the dimensionality factor and the chosen length scale. The dimensionality factor used in ST energy calculations is an average for a time-dependent dimensionality that evolves as the plume and shock trajectories evolve in time. Choosing

**Table 8:** Sedov-Taylor energy for shock detachment-limited emissive plume and schlieren shock wave in N<sub>2</sub>, Ar, and 70% CO<sub>2</sub> 30% N<sub>2</sub> gases.

Gas	Pressure (Torr)	Emissive Plume ST Energy, $E_{ST}$ (mJ)	Shock wave ST Energy, $E_{ST}$ (mJ)
N <sub>2</sub>	180	15 ± 1	18 ± 1
N <sub>2</sub>	30	77 ± 6	75 ± 3
N <sub>2</sub>	10	47 ± 7	72 ± 2
N <sub>2</sub>	3	73 ± 11	184 ± 14
Ar	180	34 ± 1	31 ± 2
Ar	30	50 ± 6	59 ± 2
Ar	10	79 ± 5	88 ± 3
Ar	3	112 ± 11	419 ± 28
CO <sub>2</sub> /N <sub>2</sub>	180	20 ± 2	17 ± 1
CO <sub>2</sub> /N <sub>2</sub>	30	62 ± 10	53 ± 3
CO <sub>2</sub> /N <sub>2</sub>	10	66 ± 12	71 ± 2
CO <sub>2</sub> /N <sub>2</sub>	3	50 ± 6	183 ± 7

to fit all the points in a plume trajectory will result in a different average dimensionality value than limiting the data fit to near the shock detachment point. In addition, an analysis where  $n \neq 3$  is dependent upon the choice of an appropriate length scale in order to obtain a more accurate blast energy from the plume data and infer the energy deposited into the plume by the ablation laser.

## 4.5 Conclusions

Emissive plume and shock wave propagation dynamics resulting from 12.5 ns, 532 nm ablation of graphite at 5.7 J/cm<sup>2</sup> in nitrogen, argon and CO<sub>2</sub>/N<sub>2</sub> background gases at various pressures have been compared. Initial plume expansion speeds are  $v_0 = 1.90\text{--}3.45$  cm/ $\mu$ s with Mach numbers as high as  $M = 97$ . The corresponding kinetic energies are 26–74 eV/atom corresponding to 11–31 laser photons.

It has been shown that sectioning emissive plume data using shock detachment improves the interpretation of Sedov-Taylor blast analysis technique. Limiting sectioning

between the Sedov-Taylor low limit and the shock detachment point provides a more accurate constraint than has been previously used for these calculations. The procedure enables improved estimates of the laser-plume energy coupling. In this work, plume blast energies ranged from 55–75% of the laser pulse energy, and matched shock wave blast energies within 3–5% when sectioned using shock detachment. Average plume dimensionality ranges from  $n = 1.99$  at 3 Torr of  $\text{CO}_2/\text{N}_2$  to hemispherical at  $n = 3$  for 180 Torr in argon, nitrogen, and  $\text{CO}_2/\text{N}_2$ . The shock waves exhibit spherical shock fronts, but evolve to lower dimensionality as pressure and mass of the background gas increase, while plumes exhibit an opposite trend, increasing towards  $n = 3$  as pressure rises.

Further experimental studies need to be performed to better characterize the processes involved in laser-plume coupling and shock detachment from the emissive plume for graphite and other materials. An examination of plume and shock morphology for differing laser footprints and plume viewing angles would improve understanding of shock wave dimensionality and its effects on plume propagation and laser coupling energy via Sedov-Taylor analysis. In addition, further exploration of the effects of varying laser wavelength and temporal plume-laser coincidence on graphite plume propagation would better establish the conditions leading to laser-plume energy coupling and its effects on overall plume dynamics. An improved understanding of underlying mechanisms driving shock detachment could result in a more nuanced understanding of where the detachment occurs under any conditions, allowing for shock detachment point predictions to further improve plume Sedov-Taylor laser-shock coupling estimates when shock visualization techniques are unavailable or undesirable. The present survey of plume and shock wave dynamics is necessary for a detailed study of shock detachment, emissive contact front propagation dynamics, and improving understanding of laser-plume energy coupling.

## V. Plume and shock morphology of pulsed laser ablation of graphite

Pulsed laser ablation of pyrolytic graphite with a  $5.7 \text{ J/cm}^2$  frequency-doubled Nd:YAG laser was performed to explore the morphology of the emissive plume and ablation shock wave in backgrounds of argon, nitrogen, and mixed gas at pressures from 3–180 Torr. An analysis comparing laser rectangular and circular spot geometries was explored using white light schlieren shock wave imaging and optical emission imaging with a 2.88–40 ns gated ICCD camera. The fast-gated imagery is used to determine the emissive plume structure and the shock wave curvature for each case. In addition, the plumes and shock waves from the rectangular spot are imaged along both the short and long axes of the laser footprint and compared to the shock and plume from the circular spot geometry cases. Radii of curvature ratios are developed using the shock wave imagery for each geometry and compared to the Sedov-Taylor model dimensionality fit parameter,  $n$ . The emissive plume from the rectangular spot shows evidence of uneven ablation when viewed along the long axis, while the circular spot plume shows evidence of a reflected shock propagating back towards the target surface at later times. The 10 Torr shock waves for both geometries exhibit mostly spherical shock fronts, but the Sedov-Taylor dimensionality decreases to planar-cylindrical for the rectangle geometry and cylindrical-spherical for the circular geometry as pressure and mass of the background gas increase. The radii of curvature ratios for both spot geometries exhibit the opposite trend where the shock wave appears to be closer to spherical as pressure increases to 180 Torr.

### 5.1 Introduction

Pulsed laser ablation (PLA) of materials has a wide variety of applications including representative analysis of hypersonic thermal protection materials [122], synthesis of nano-scale composites such as gold-graphene nano-colloidal solutions [123], and simulating

micrometeorite bombardment craters [124]. Optical characterization of emissive plume dynamics and relevant laser-target interactions are essential to most material processing quality control strategies [1, 2] as they can directly reflect ablation conditions, allowing for the state of the final product to be characterized in near real-time and adjustments made to the process as required [125].

Prior laser ablation studies of graphite have focused on the characterizing formation and dynamics of neutral and ionized constituents in the emissive plume as opposed to plume and shock morphology [21, 24, 29, 126]. Although a several studies have included some exploration of the laser ablation shock wave for graphite [64, 75, 76], most focus on the emissive plume structure. Ursu, Nica, and Focsa explored graphite ablation in vacuum and argon with fast imaging and emission spectroscopy [27]. They identified a v-shaped structure in the emissive plume for pressures below 0.0075 Torr, that propagated outwards along the target normal. Ursu et. al. further explored the v-shaped plume structure with fast imaging and fractal modeling [25, 26]. They concluded that the v-shaped structure was related to increased carbon dimer formation and cooling at the edges of the plume. More recently, Eliceiri and Grigoropoulos used shadowgraphy, laser probing, and spectroscopy combined with normal and side imaging, to explore graphite plume plasma shielding and density distribution [76]. Some plume morphology studies have been performed for other target materials including metals such as copper [77] and aluminum [78], or investigate varying parameters such as spot size [79] or background gas [80]. However most studies rely only on fast imaging and optical emission spectroscopy to explore the dynamics of the emissive plume.

Schlieren fast imaging of pulsed laser ablation offers an opportunity to explore shock wave morphology as it relates to the emissive plume. Shock wave propagation is often indirectly studied by characterizing the emissive plume contact front propagation trajectories along with an assumption that the emissive contact front is co-located with the shock wave.

With schlieren shock wave imaging and fast-gated emission imaging, both the shock wave and the emission plume structures can be studied in the same experimental setup. By using different focusing lenses, laser spot footprint geometries can be changed and the effect of footprint shape on ablation shock and plume propagation can be explored. Shock wave and emissive plume shape or dimensionality is often approximated using the Sedov-Taylor blast model to fit the trajectory, yielding the Sedov-Taylor dimensionality factor,  $n$  [4, 5]. In addition, shock wave imagery can be examined to infer shock morphology and curvature by leveraging the shape of the shadow in the image caused by the change in the refractive index due to a pressure or density gradient from a passing shock wave [58]. By adding imagery of the rectangular geometry laser spot plume dynamics along both the short and long axes, plume and shock morphology in two dimensions can be obtained.

Very few studies have been conducted that directly compare shock wave to emissive plume morphology for PLA of graphite using multiple laser footprint geometries. There are no prior graphite studies available that examine the morphology of both the emissive plume and the shock wave in detail.

This work focuses on the PLA of graphite, examining emissive plume and shock wave morphology resulting from different laser spot geometries including a rectangular spot along both long and short axes, and a circular spot. This research is part of a larger study focusing on the characterization of spatial and temporal dynamics of continuous wave and pulsed laser effects on graphite and carbon fiber targets [41, 84, 97].

## **5.2 Apparatus and Methodology**

A schematic of the experimental apparatus is shown in Fig. 26. This study is part of a larger program and further details of experimental setup have been provided previously [1]. Briefly, pyrolytic graphite samples purchased from the Graphite Store [98] were irradiated with a Quantel EverGreen2 EVG00145 Nd:YAG laser at 532 nm used in single pulse mode

to deliver an average energy of 90 mJ per pulse onto a graphite target in a vacuum chamber backfilled with various gases and pressures. The laser pulse exhibited a full width half max of 12.5 ns and a rise time of 6.6 ns. The ablation plume propagates normal to the target in the z-direction.

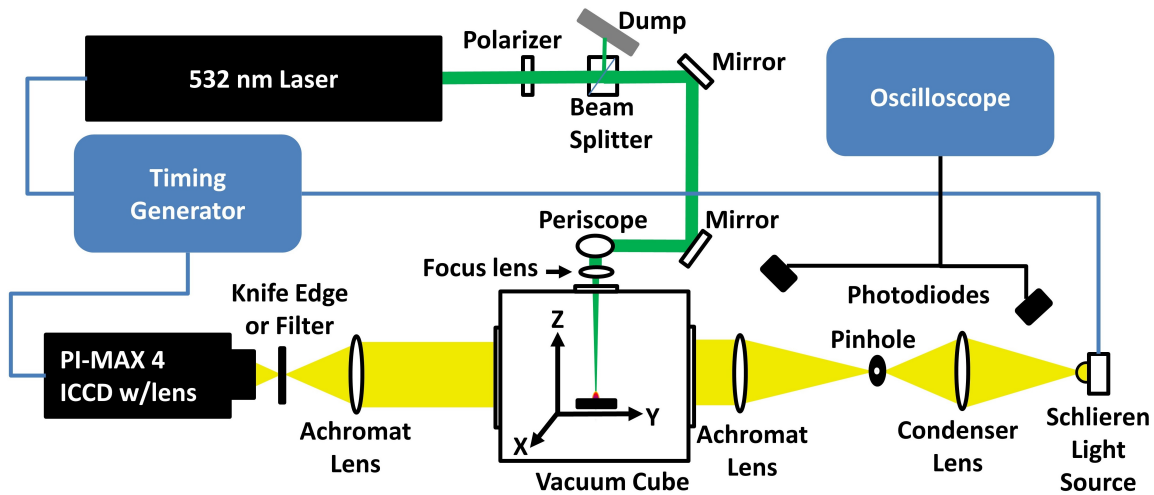


**Figure 26:** Experimental apparatus includes a vacuum chamber containing a sample target, PIMAX 4 ICCD camera, white light LED, and schlieren optics. The target is ablated using a Nd:YAG pulsed laser source ( $\lambda = 532$  nm, 12.5 ns pulse width, average energy 90 mJ per pulse at target).

Two different focusing lenses were used to compare the effects of laser spot. The laser was focused onto the target at normal incidence using a 1"  $f = 150$  mm AR-coated plano-convex fused silica lens yielding an intensity of  $0.456 \text{ GW/cm}^2$  and fluence of  $5.7 \text{ J/cm}^2$  onto an approximately circular  $1.578 \text{ mm}^2$  area spot. The focusing lens was then replaced with a 1"  $f = 150$  mm AR-coated cylindrical fused silica lens to shape the pulse laser beam into a roughly rectangular spot on the target, approximately  $4.2 \times 0.4 \text{ mm}$  with a measured area of  $1.6 \text{ mm}^2$ , yielding an intensity of  $0.450 \text{ GW/cm}^2$  and a fluence of  $5.62 \text{ J/cm}^2$ . The cylindrical lens was rotated into two different orthogonal orientations, allowing the ICCD camera to view the long axis of the spot in one orientation and the short axis of the spot in the other orientation. The targets were 1" diameter by 0.25" thickness pyrolytic graphite sputtering target discs (99.999% C) sourced from the Graphite Store with properties provided in Table 9. The chamber was evacuated to a pressure of  $10^{-3}$  Torr

with a turbomolecular pump and then backfilled to 3 Torr to 180 Torr of 99.999% nitrogen, argon, air, or a mixed gas of 70% CO<sub>2</sub> and 30% N<sub>2</sub> (CO<sub>2</sub>/N<sub>2</sub>), at T = 298 K.

**Table 9:** Properties of pyrolytic graphite samples.

Property	Value	Ref.
Density, $\rho$ (g/cm <sup>3</sup> )	2.2	[98]
Conductivity, $K$ (W/m·K) (across layers)	3.5	[98]
Conductivity, $K$ (W/m·K) (within layers)	400	[98]
Specific Heat, $C_p$ (J/kg·K) (T = 3500 K)	2135	[99]
Sublimation Temperature, T (K)	3923	[100]
Heat of Sublimation, $h_s$ (kJ/g)	61.3	[100]

A Princeton Instruments PI-MAX4 1024i with a 1024 x 1024 Gen III fast gate intensified charged-coupled device (ICCD) camera with a Nikon AF Nikkor 85 mm f/1.8 lens was used to capture schlieren shock wave imagery and emissive imagery of the ablation event. The field of view (FOV) of the lens was 4.55 by 4.55 cm with a circular schlieren-illuminated FOV of 3.17 cm by 2.85 cm and a resolution of 0.044 mm, or 44  $\mu$ m, per pixel. The camera was gated with delays of up to 20  $\mu$ s after the laser shot and gate widths (integration time) from 2.88 ns to 50 ns. Emissive plume imagery was collected with linearly varying gate widths and delays with 2 ns gate widths at the start of the collection and 10 ns widths at the end of the collection. Emissive plume images began at the onset of the laser pulse (defined as t = 0) and out to a delay of 1200 ns after the pulse. Images exhibited < 1% pulse-to-pulse laser flicker and < 2 ns pulse-to-pulse laser timing jitter. Shot-to-shot variation in laser pulse energy was < 1%, and the laser energy on target was corrected day to day by using a polarizer and polarizing beam splitter to maintain the baseline.

A white light fast-response LED was used as the schlieren light source. The LED was pulsed on for 30  $\mu$ s per laser shot to enable high intensity illumination and was synchronized to overlap the full camera gate delay period. 2" spherical cemented achromatic doublet lenses were used for all schlieren optics. The LED light was collected and focused with an f = 75 mm condenser lens onto an iris pinhole. The light was then collimated using

an  $f = 300$  mm lens and passed horizontally along the  $y$ -axis through the vacuum chamber and target region through large 5" flat windows. The collimated light and plume emission was then focused with an  $f = 300$  mm lens onto a horizontally mounted razor blade as the schlieren knife-edge. A 2" 532 nm notch filter was used at the camera lens to protect the camera from oversaturation due to the laser radiation. Each schlieren test series consisted of two sets of 50 laser shots with corresponding images, one image per laser shot, and imagery were taken with fixed gate widths of 40 ns to improve signal and linearly varying time delays from 800 ns to 20  $\mu$ s.

### **5.3 Results and Discussion**

#### **5.3.1 Rectangular Spot Plume Morphology**

The temporal evolution of the ablation plume morphology was imaged with the short side of the rectangular spot ( $x$ -axis) parallel to the FOV as seen in Fig. 27a–f, and then the long side of the rectangular spot ( $y$ -axis) parallel to the FOV as seen in Fig. 27h–l. The plumes evolve in 10 Torr nitrogen background gas with gate delays from 107–822 ns, and linearly increasing gate widths from 2.88–10 ns. At early times, the short axis view of the emissive plume approximately matches the 0.4 mm laser spot dimension.

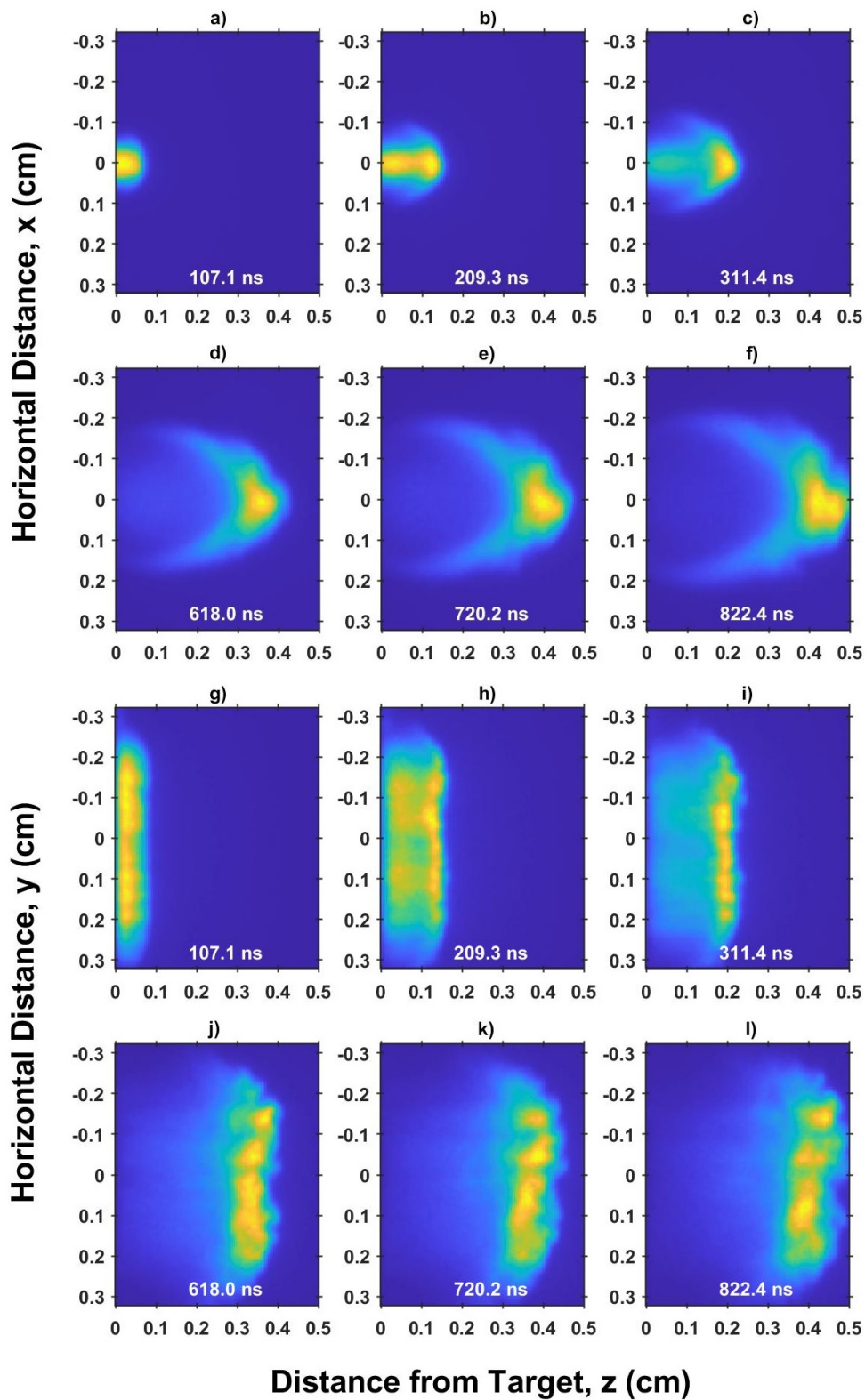


**Figure 27:** Emissive ICCD image series demonstrating plume morphology for ablation of graphite in nitrogen at 10 Torr for the rectangular laser footprint viewed along the short x-axis (a–f), and long y-axis (g–l), with gate delays from 100 ns to 820 ns.

In Fig. 27a–f The ablation plume contact front appears between 100 and 200 ns and is slightly larger than the small spot size dimension of 0.4 mm. Before the contact front develops, a faint area of emission is present within the first 0.05 cm from the target surface, fading away before ~ 300 ns. The diffuse emission was also present in the Chapter 3 study and is most likely due to the plume material not having experienced enough collisions with the background gas to form a significant contact front during very early propagation times. The emissive contact front propagates away from the target surface leaving a crescent-like trail of emission in its wake.

In Fig. 27g–l, the emission at early times approximately matches the long spot dimension of 5.5 mm. The emissive contact front along this view shows fairly linear propagation along the leading edge of the plume, with little curvature evident as time progresses. The emissive contact front exhibits gradual broadening along the direction of propagation as times increase, most likely due to plume materials with different velocities experiencing drag in the background gas and slowing. The plume also exhibits areas of varying emission intensity along the contact front, giving it a mottled appearance. As the regions of brighter emission can be identified in each successive image, each of which represents a single and completely separate laser ablation event, the structure must be due to an ablation process and not due to random variation within a single plume event. The mechanism for the mottled appearance of the plume is likely not due to a hydrodynamic instability or turbulence since the structures in the images persist between separate ablation events. The mottled appearance could be driven by uneven ablation of the target surface along the y-axis resulting in locally denser regions within the plume which lead to increased local emission from the excited plume material in those regions.

The images in Fig. 28 show the short x-axis views of the plume at a gate delay of 618 ns in nitrogen, argon, and CO<sub>2</sub>/N<sub>2</sub> with pressures ranging from 3–180 Torr. The center of the emissive contact front region is triangular at lower pressures, while exhibiting an arc-like

shape at higher pressures. The arc-shaped tails of the plume are wider at the lowest pressures, becoming more confined by the background gas at higher pressures. Other than the shape of the plume core and the fainter wings, no other significant morphological structures are evident from the x-axis orientation.

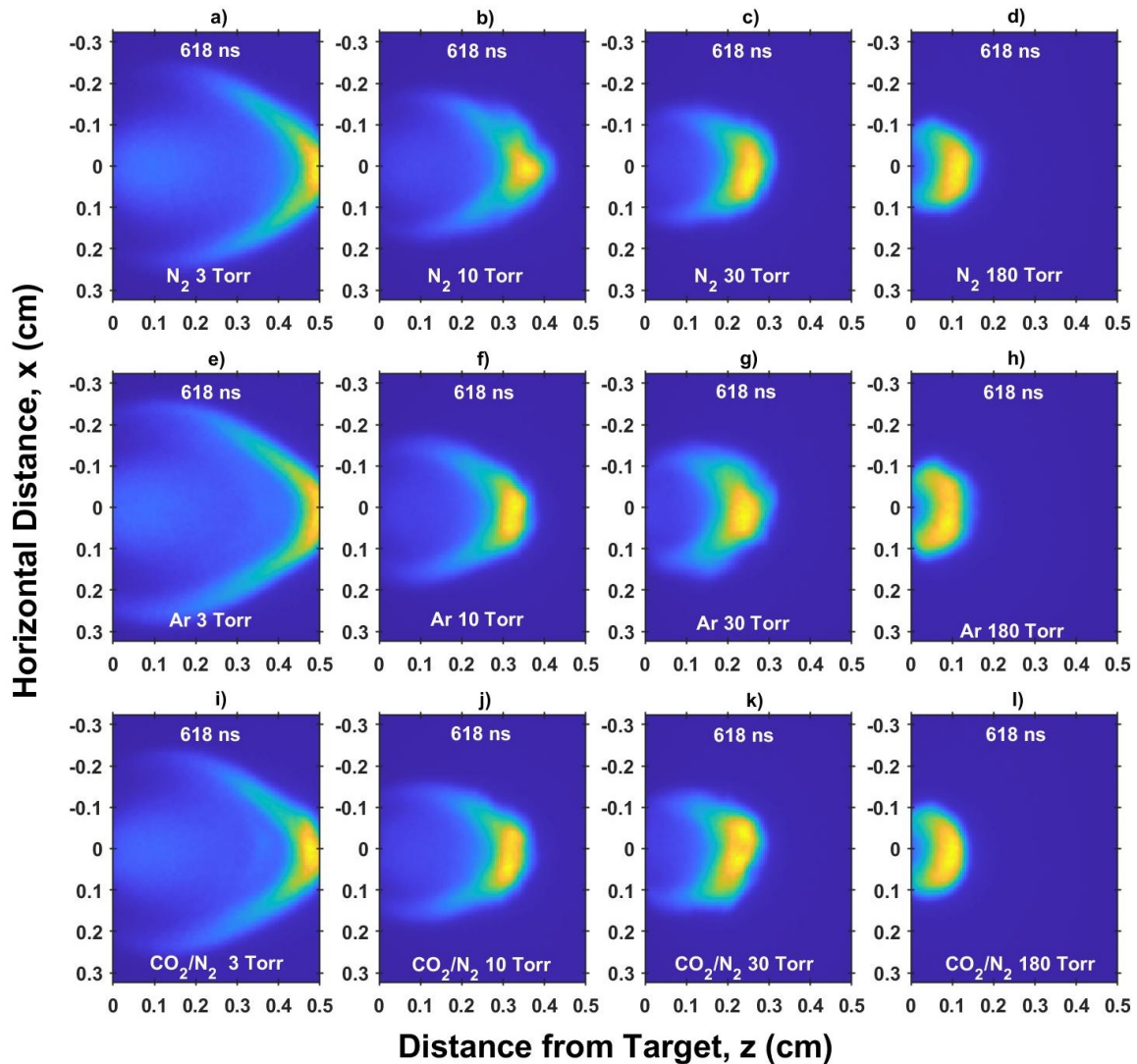


**Figure 28:** Emissive ICCD image series at  $t = 618$  ns demonstrating plume morphology for ablation of graphite in nitrogen (a–d), argon (e–h), and 70%  $CO_2$ /30%  $N_2$  (i–l), for a rectangular laser footprint viewed along the short x-axis, in pressures ranging from 3 to 180 Torr.

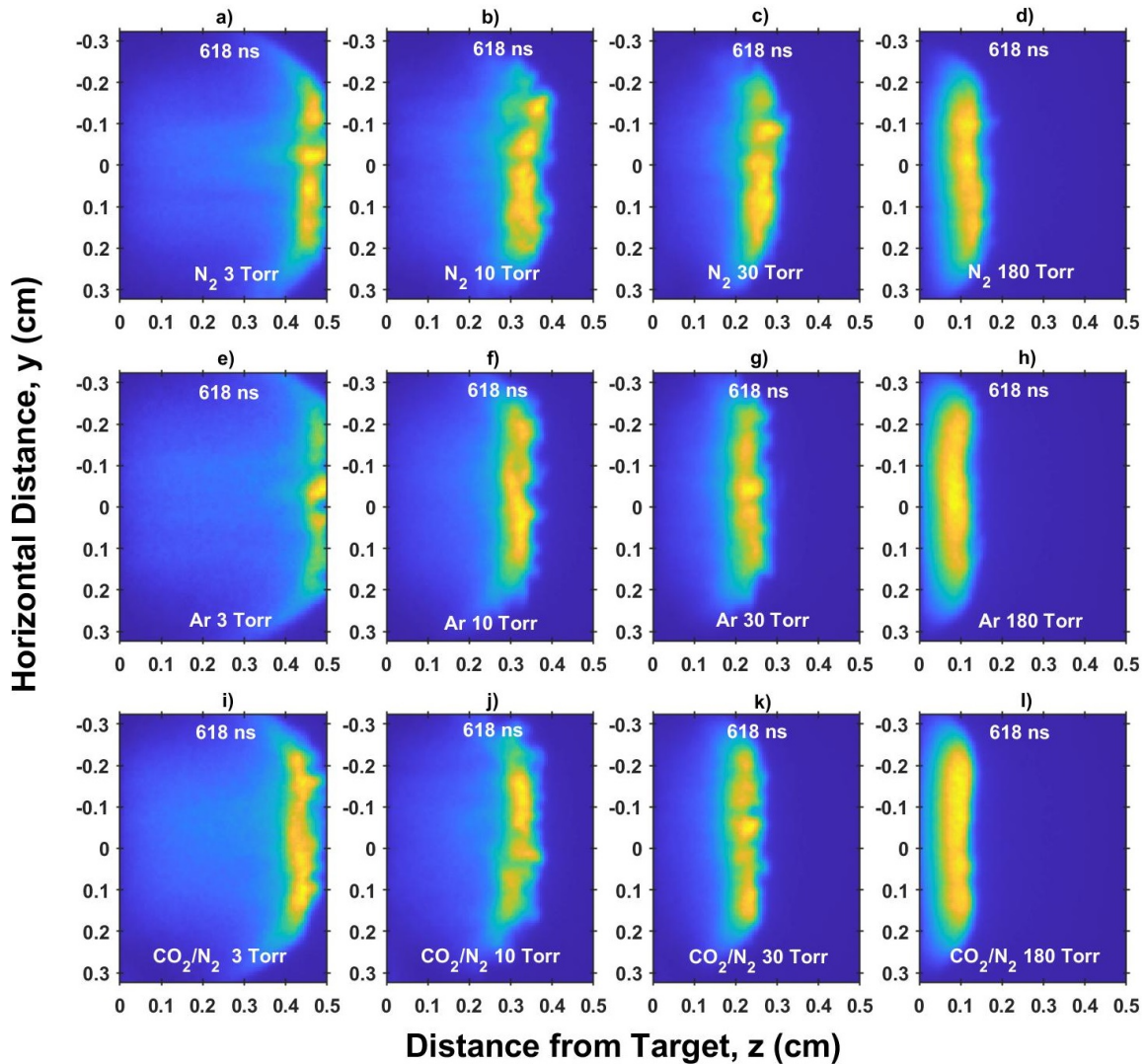


**Figure 29:** Emissive ICCD image series at  $t = 618$  ns demonstrating plume morphology for ablation of graphite in nitrogen (a–d), argon (e–h), and 70%  $\text{CO}_2/30\%$   $\text{N}_2$  (i–l), for a rectangular laser footprint viewed along the long  $y$ -axis, in pressures ranging from 3 to 180 Torr.

The images in Fig. 29 show the long  $y$ -axis views of the plume at a gate delay of 618 ns in nitrogen, argon, and  $\text{CO}_2/\text{N}_2$  with pressures ranging from 3–180 Torr. As with Fig. 28, the plumes show a similar morphology with the wings of the plumes extending further along the  $y$ -axis as pressure is decreased. The emission for the 180 Torr cases is significantly increased and less mottled in appearance. The more uniform appearance of the plumes for these cases supports the possibility that plume density is higher and more

evenly spread out within the plume. Unlike the plume trajectories from the circular laser spot, the plume propagated with a slightly higher velocity in argon than in the nitrogen case at low pressures, with the CO<sub>2</sub>/N<sub>2</sub> plume propagating more slowly. At 180 Torr, the nitrogen exhibited a slightly further progression at 618 ns. The long axis view of the plume revealed a distinctly planar shape as compared to the short axis view, especially in the higher pressures cases. For the low pressure cases in Fig. 29, plume curvature starts to become evident at the sides of the plume near  $y = \pm 0.2\text{--}0.3$  cm.

The view of the long y-axis plume is the same viewing geometry used by Ursu et. al. when they explored a v-shaped structure in the emissive plume for a particular focusing of their laser spot [26, 27]. The v-shape was not evident in the emissive plume imagery for the current study. However, the Ursu et. al. experimental apparatus utilized a pulsed KrF laser at 248 nm with nearly twice the pulse width as the laser in the current study, and the pressures were much lower, ranging from  $10^{-7}$  Torr to 0.0675 Torr. Further exploration with more matching experimental parameters needs to be completed in order to properly validate and explore the morphology seen by Ursu et. al. No other unexpected morphological features were present in the current y-axis imagery.

### **5.3.2 Circular Spot Plume Morphology**

The evolution of the ablation plume from a circular laser spot footprint is demonstrated in Fig. 30, for 10 Torr nitrogen and gate delays from 120 ns to 830 ns. The camera gate width was increased linearly from 2.88 ns to 30 ns for this set of images. At early times, the emissive plume approximately matches the 1.4 mm diameter of the laser spot.

The ablation plume contact front is well established by 120 ns. Visually, the circular plume is most similar to the short x-axis rectangular plume in Fig. 27. The emissive contact front in the circular spot size plume leaves a crescent-like trail of faint emission in its wake, similar to the rectangle x-axis imagery. However, the circle emissive plume is much

rounder in appearance than the rectangular crescent. The emissive contact front exhibits minor gradual broadening both along and perpendicular to the direction of propagation as times increase.

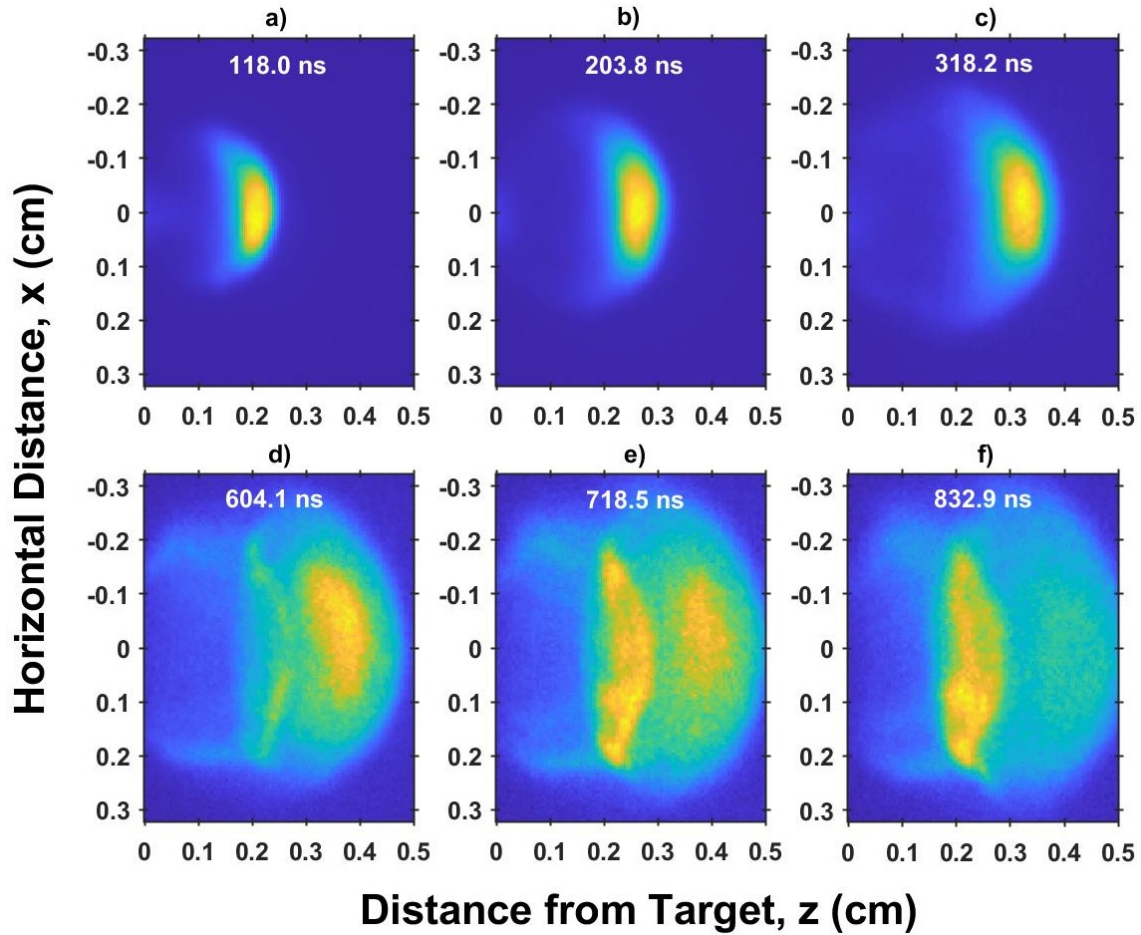


**Figure 30:** Emissive ICCD image series demonstrating plume morphology for ablation of graphite in nitrogen at 10 Torr for a circular laser footprint with gate delays from 120 ns to 830 ns.

The velocity of the circle plume is much greater than the rectangular plume in Fig. 27, with the circular plume traveling approximately 15 mm further than the rectangular plume for the same time delay of  $t \sim 318$  ns. Although a portion of the increased velocity could be due to the slightly larger fluence ( $\sim 0.08$  J/cm<sup>2</sup> higher) for the circular spot, the bulk of the increased velocity is likely due to an increase in the laser-plume energy coupling due to the tighter spot profile. The lower aspect ratio of the circular plume likely enables the

plume to obtain a more hydrodynamic, bullet-like shape, allowing it to punch through the background gas with less drag than the stretched out plume in the rectangular spot case.

The circular plume exhibits a prominent emission feature that propagates backwards towards the target surface at later times as seen in the last three images in Fig. 30. The feature was not evident in the rectangular plume imagery. The emission feature appears to be a reflected shock, and is possibly due to plume splitting with a late fast plume component colliding with and then rebounding off an earlier slow component. The rebounding component experiences collisions with the interior of the plume, resulting in the region of increased emission propagating backwards towards the target surface. At even later times, the rebounded shock appears to impact the target, resulting in further emission at the surface of the target. A similar rebounded emissive plume feature was recently seen by Pierce who explored pulsed ablation of graphite with a 248 nm KrF laser [127]. The corresponding circular spot shock wave imagery was examined, but no rebounded shock wave was visible in the imagery in the vicinity of the reflected emissive plume. However, the emissive plume in this region showed significantly brightness in the schlieren shock wave imagery, potentially obscuring the motion of the shock wave near the target. It is also possible that the rebounded shock was too weak to be detected by the schlieren apparatus. The feature cannot be from a shock wave that has rebounded off the vacuum chamber walls as the main shock wave from the laser ablation is visible in the camera field of view out to 20  $\mu$ s.

Figure 31 shows the circular spot plume at gate delay of  $\sim 330$  ns in nitrogen, argon, and CO<sub>2</sub>/N<sub>2</sub> with pressures ranging from 3–180 Torr. The plumes show a similar morphology with the plumes exhibiting increased velocity as the pressure is decreased, while the plumes are more spatially confined by the background gases as pressure is increased. The propagation distances for different gases at similar pressures are similar with the exception of the CO<sub>2</sub>/N<sub>2</sub> cases at all pressures which are visibly slowed with less distance traveled for

the same time periods. The  $\text{CO}_2/\text{N}_2$  cases also showed significantly more overall spatial plume confinement at all tested pressures, most likely due to the heavier background gas.

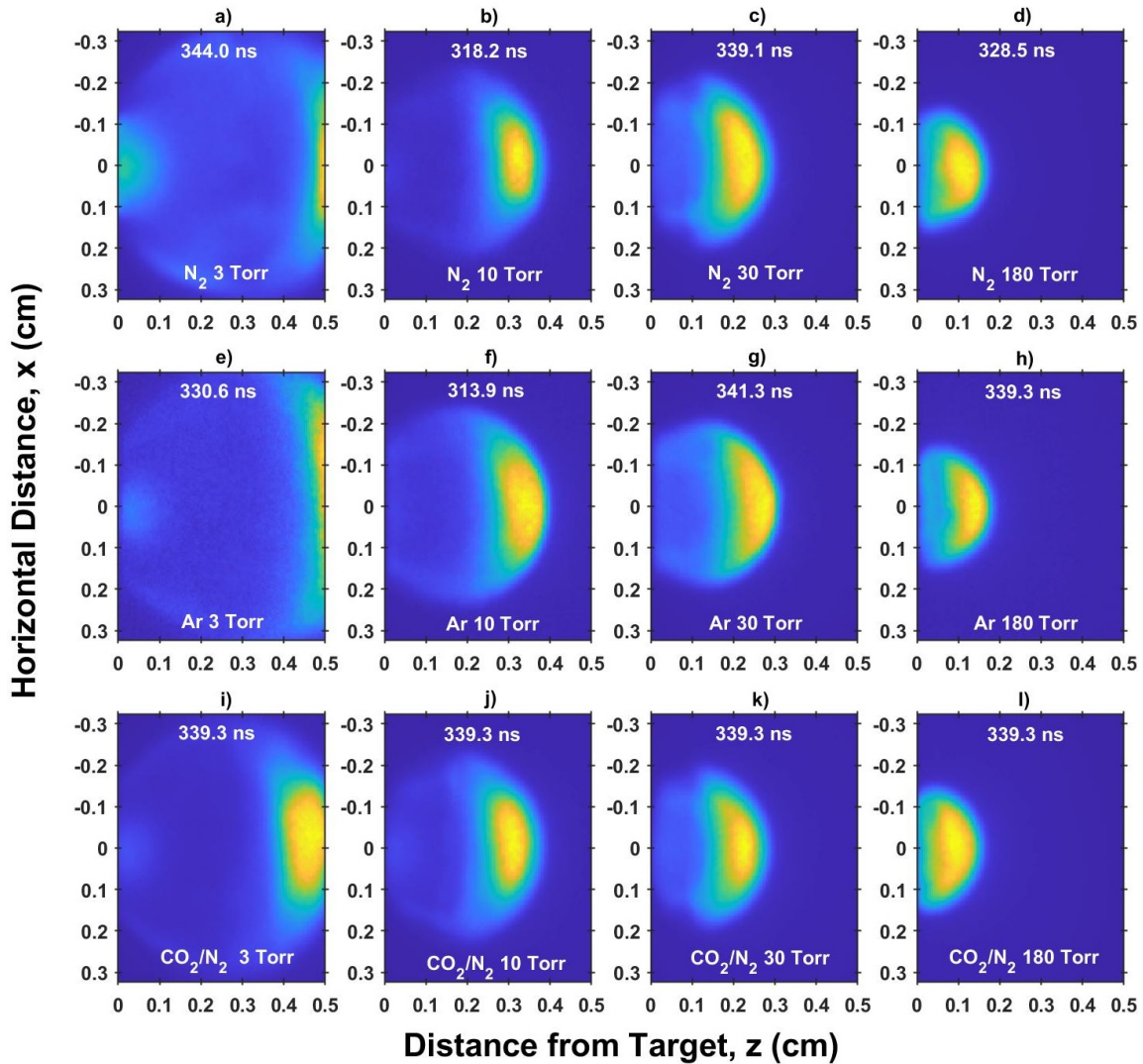


**Figure 31:** Emissive ICCD image series at  $t \sim 330$  ns demonstrating plume morphology for ablation of graphite in nitrogen (a–d), argon (e–h), and 70%  $\text{CO}_2/30\%$   $\text{N}_2$  (i–l), for a circular laser footprint in pressures ranging from 3 to 180 Torr. The slightly different delays are due to minor gate width differences between each series.

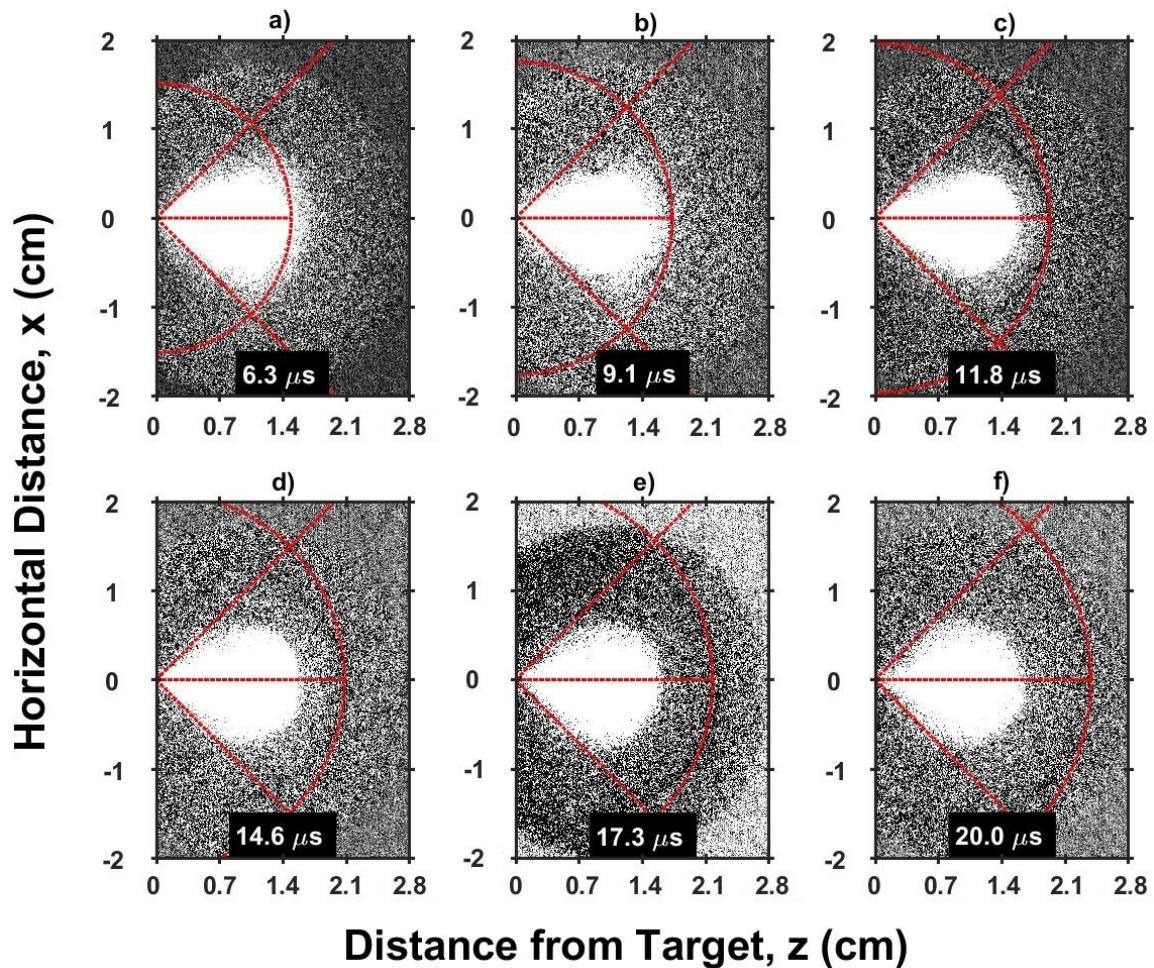
### 5.3.3 Rectangular Spot Shock Morphology

Schlieren imaging was used to produce the images in Fig. 32 and Fig. 33, which show the shock wave morphology for ablation of graphite in nitrogen at 10 Torr for a rectangular

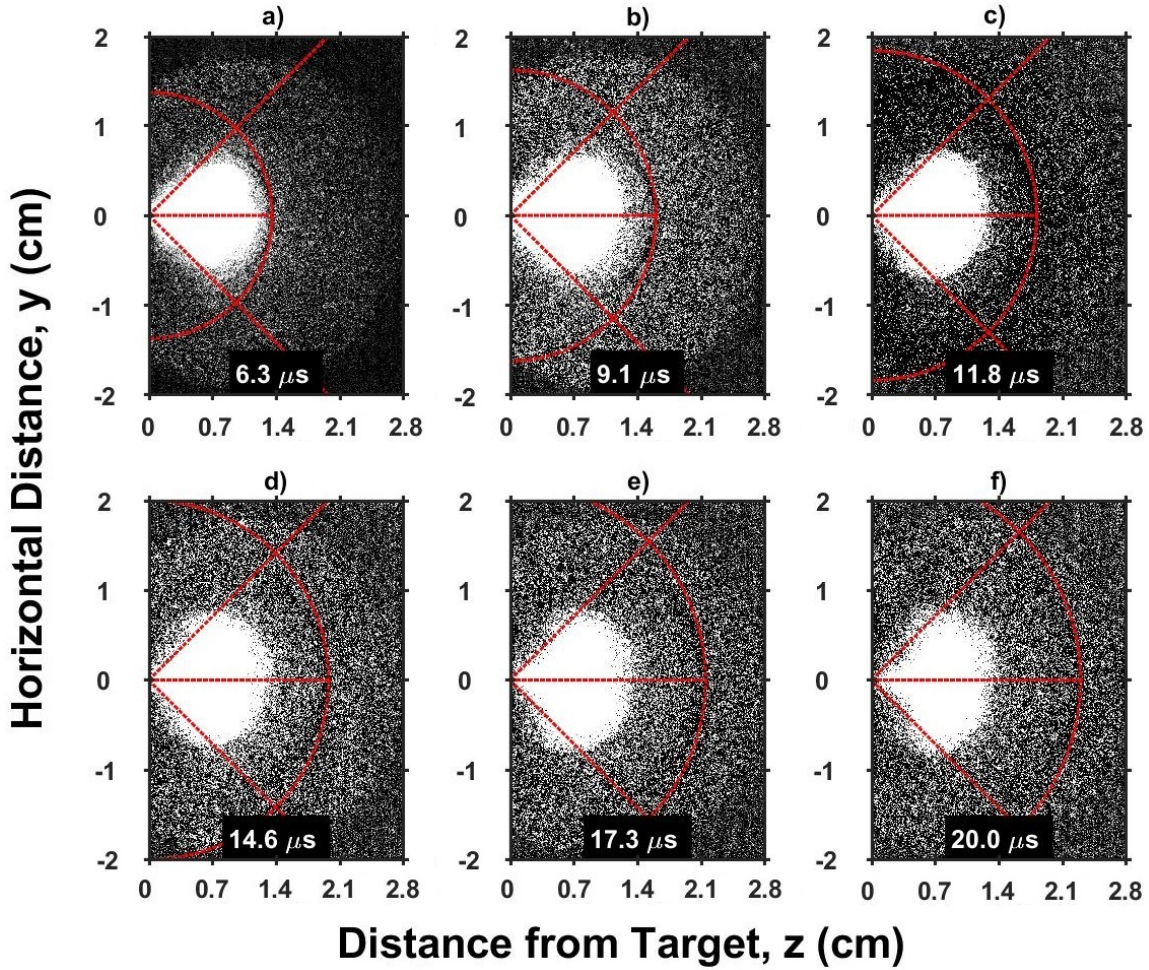
laser footprint viewing the short x-axis and the longer y-axis respectively, for gate delays from 6.3  $\mu\text{s}$  to 20  $\mu\text{s}$ . The shock wave is evidenced by the dark shadow in the images as the passing shock wave caused a localized gradient in the index of refraction. The bright emissive plume is visible in the images as a white central region above the target surface. Note that the times for the schlieren imagery figures are significantly later than the plume imagery in the plume morphology section. The time differences are especially notable between the y-axis plume and shock imagery, where the schlieren imagery show significant curvature in the shock waves, while the y-axis plume imagery is still planar in appearance. The difference in curvature is expected as initially planar plumes are expected to experience increasing curvature towards cylindrical or spherical as time progresses, which has been noted in previous studies [50, 101]. Essentially, at later times and propagation distances the initial ablation event appears to be more point-source like, resulting in increasing curvature of the shock and plume as time progresses. No shock wave was visible in the 3 Torr rectangular schlieren imagery for any of the background gases, most likely due to the higher aspect ratio of the rectangular spot size spreading out the shock energy over a larger area thus reducing the strength of the index gradient below the detection limits of the schlieren system. A brighter schlieren light source would improve the schlieren sensitivity to weaker shocks.

In order to better visualize and analyse the curvature of the shock wave, hemispheres were superimposed on the images centered at the target, corresponding to the shock distance normal to the target surface at the respective time delay. A completely spherical shock wave would closely match the hemisphere with more or less constant radii of curvature from all points extending outwards from the origin. Two 45 degree guide lines and a 90 degree (normal) guide line were overlaid in order to estimate radii of curvature ratios for the shock waves. The radii of curvature ratio was calculated by dividing the distance from the target to the shock wave along 45 degrees by the distance of the target to the shock

wave along the normal 90 degree guide line. A ratio of 1 results from equal radii of curvature to the shock wave and suggests a spherical dimensionality. A ratio less than 1 implies a shock wave less than spherical in dimensionality. A purely planar shock would result in a ratio greater than 1. The shock curvature at 45 degrees in Fig. 32 and Fig. 33 are similar at each gate delay, with minimal change to the curvature for the shock wave propagation out to 20  $\mu\text{s}$ .



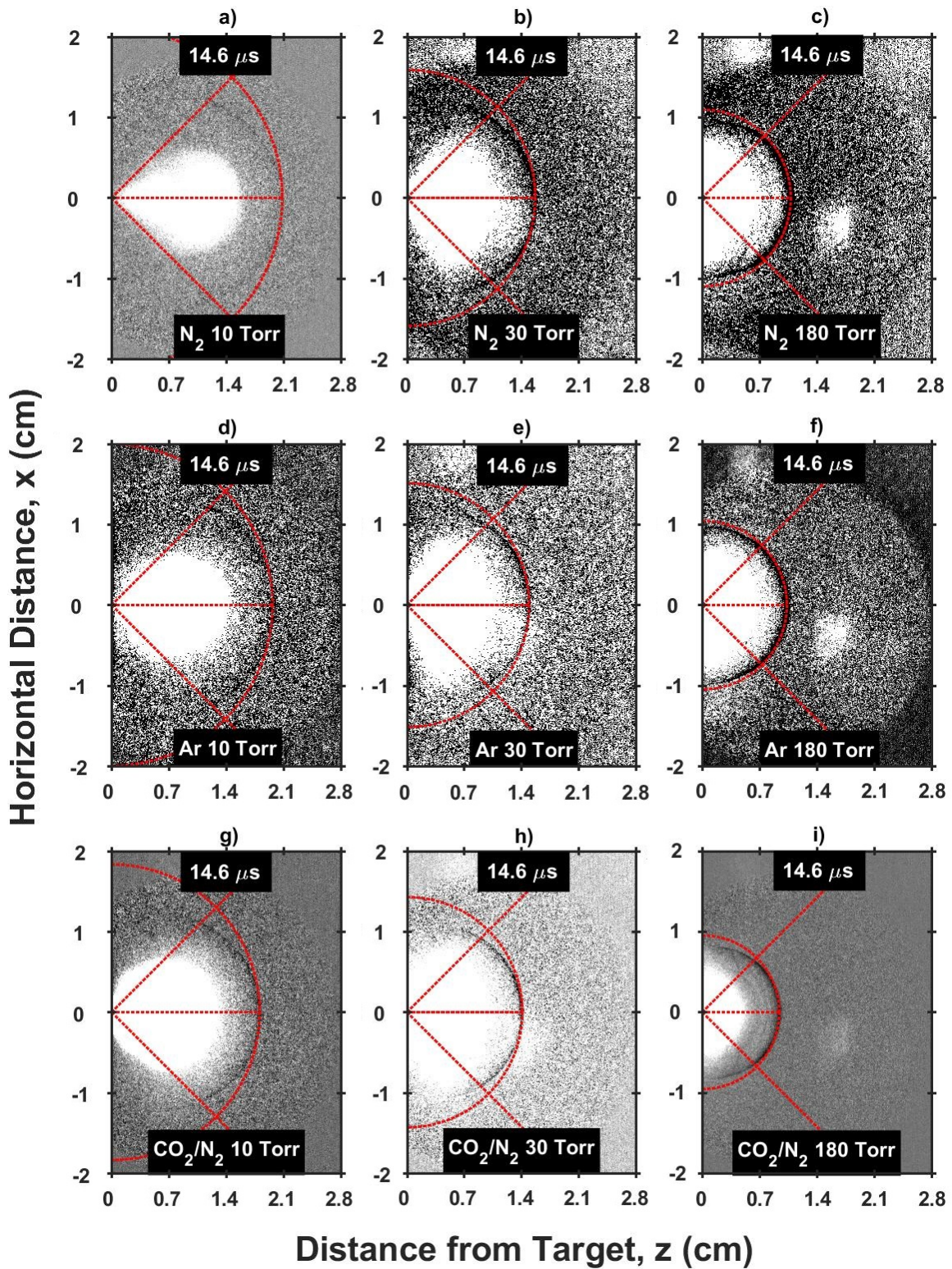
**Figure 32:** Schlieren ICCD image series demonstrating shock wave morphology for ablation of graphite in nitrogen at 10 Torr for a rectangular laser footprint viewing the short x-axis with gate delays from 6.3  $\mu\text{s}$  to 20  $\mu\text{s}$ . Hemispheres are superimposed on the images, corresponding to the shock location normal to the target surface, along with two 45 degree guidelines and a 90 degree (normal) guideline used to estimate radii of curvature ratios.



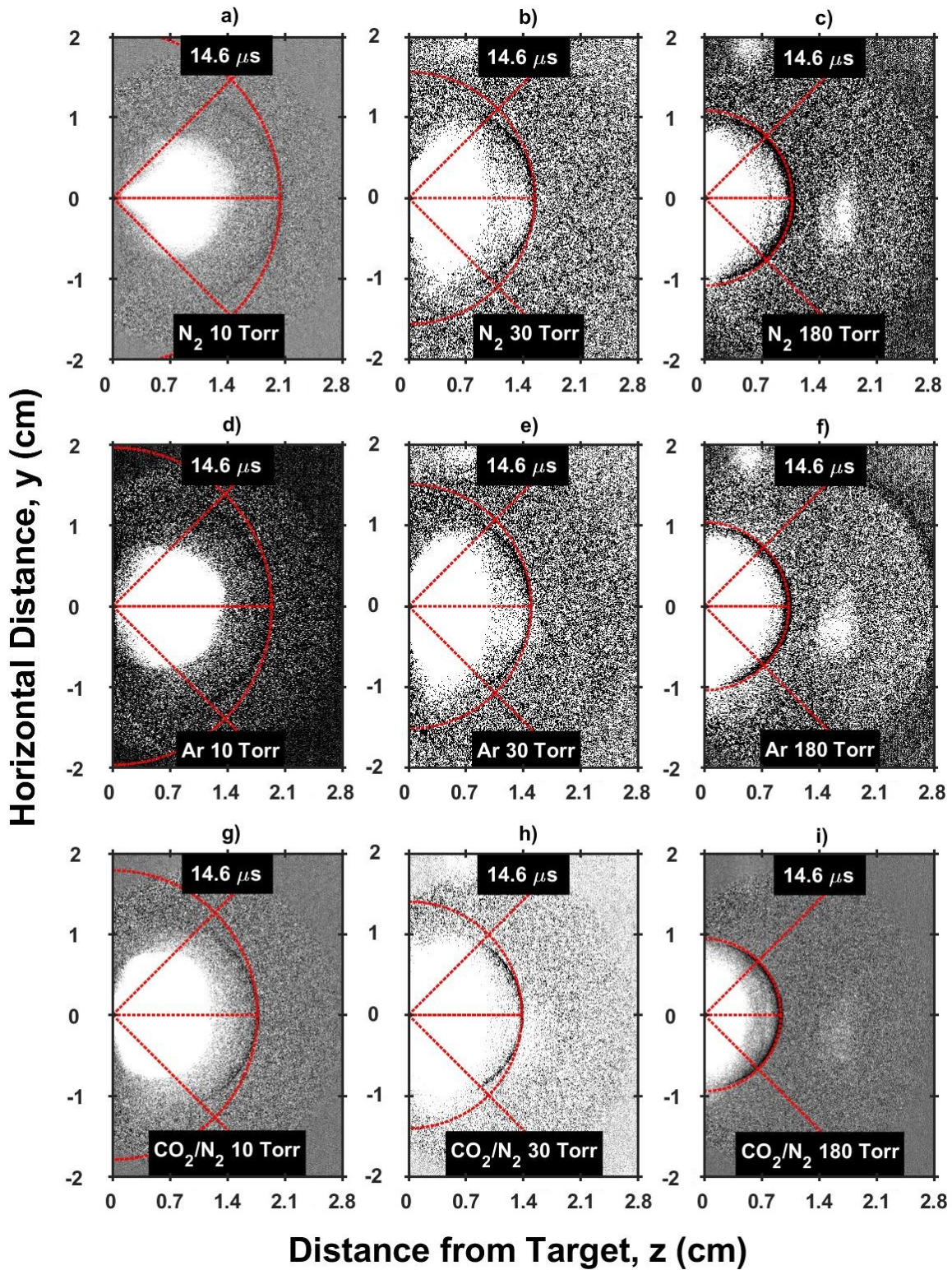
**Figure 33:** Schlieren ICCD image series demonstrating shock wave morphology for ablation of graphite in nitrogen at 10 Torr for a rectangular laser footprint viewing the long y-axis with gate delays from 6.3  $\mu\text{s}$  to 20  $\mu\text{s}$ .

Figure 34 and Fig. 35 show the rectangular spot schlieren imagery for the short and long axes, respectively, at gate delay of  $t = 14.6 \mu\text{s}$  in nitrogen, argon, and  $\text{CO}_2/\text{N}_2$  with pressures ranging from 3–180 Torr. The shock wave is visibly darker in the 180 Torr gas cases, with the refractive index gradient fading in magnitude as pressure is decreased. This is likely due to a sharper pressure change between the background gas and the shock wave, leading to an increased index of refraction gradient at higher pressures. Similar to the plume imagery, the shock imagery shows a slower shock wave propagation for the higher pressure gas cases with the least progression evident in the  $\text{CO}_2/\text{N}_2$  gas, especially at 180 Torr. The

propagation in nitrogen and argon background gases is similar at like pressures, as is the curvature of the plume at the 45 degree angle points. At angles less than 45 degrees, the shock waves continue to deviate from a spherical, with the deviation increasing closer to the surface. The trend is visible in both the long axis shock wave imagery and the short axis shock wave imagery. The appearance of the shock wave structures could be a result of increased forward motion or expansion of the shock wave compared to expansion outwards away from the target normal.



**Figure 34:** Schlieren image series at  $t = 14.6 \mu\text{s}$  demonstrating plume morphology for ablation of graphite in nitrogen (a–c), argon (d–f), and 70%  $\text{CO}_2$ /30%  $\text{N}_2$  (g–i), for a rectangular laser footprint viewing the short x-axis in pressures ranging from 10 to 180 Torr.



**Figure 35:** Schlieren image series at  $t = 14.6 \mu\text{s}$  demonstrating plume morphology for ablation of graphite in nitrogen (a–c), argon (d–f), and 70%  $\text{CO}_2$ /30%  $\text{N}_2$  (g–i), for a rectangular laser footprint viewing the long y-axis in pressures ranging from 10 to 180 Torr.

Table 10 gives the curvature ratio from the rectangular spot shock wave imagery and compares it to the Sedov-Taylor dimensionality parameter,  $n$ , which was found by fitting the shock wave trajectories to a generalized Sedov-Taylor blast equation [4, 5, 74]. The error values given in the table are 95% confidence intervals for both the dimensionality and the curvature ratio. The details of the Sedov-Taylor fit process are provided in detail in Chapter 4. Since the Sedov-Taylor dimensionality factor is actually an average over time, the curvature ratios in Table 9 were calculated by finding the ratio for each time delay and then averaging the resulting curvature ratios for the entire propagation of the shock wave.

**Table 10:** Rectangular laser spot Sedov-Taylor dimensionalities and radius of curvature ratios for ablation shock waves.

Gas	Pressure (Torr)	Sedov-Taylor Dimensionality, $n$	Curvature Ratio
N <sub>2</sub>	180	1.62 ± 0.01	0.95 ± 0.01
N <sub>2</sub>	30	2.47 ± 0.05	0.87 ± 0.03
N <sub>2</sub>	10	2.81 ± 0.04	0.83 ± 0.04
Ar	180	1.70 ± 0.06	0.96 ± 0.01
Ar	30	2.42 ± 0.04	0.92 ± 0.02
Ar	10	2.77 ± 0.03	0.85 ± 0.03
CO <sub>2</sub> /N <sub>2</sub>	180	1.60 ± 0.04	0.93 ± 0.01
CO <sub>2</sub> /N <sub>2</sub>	30	2.49 ± 0.05	0.89 ± 0.02
CO <sub>2</sub> /N <sub>2</sub>	10	2.87 ± 0.04	0.83 ± 0.03

The Sedov-Taylor dimensionality factors for the rectangular laser spot geometry show a trend where dimensionality decreases as pressure increases. This trend has been seen in a study of ablation of aluminum and titanium in argon which used rectangular laser ablation spot geometry [101]. The highest pressure cases show a dimensionality between planar ( $n = 1$ ) and cylindrical ( $n = 2$ ) geometry, tending towards a cylindrical shock wave. The lower pressures progress towards a mix of spherical ( $n = 3$ ) dimensionality and cylindrical dimensionality with the 10 Torr cases trending closer to spherical. A planar dimensionality component is expected since the elongated rectangular plume in the emissive imagery is planar in appearance in the long axis imagery.

Interestingly, the curvature ratio appears to show the opposite trend to the Sedov-Taylor dimensionality as the shock is appears to become less spherical as pressure decreases. There are several possible explanations for the inconsistency in the shock wave morphology between the Sedov-Taylor model dimensionality factor and the curvature ratio. Two previous studies have indicated that Sedov-Taylor modeling of side transmission imaging for ablation plumes, such as schlieren imaging in this study, does not perform as well due to the ideal density distribution assumptions used in the original Sedov-Taylor model [76, 128]. The issue could be related to the cosine-power angular distribution ( $\cos^P \theta$ ) of the ablation plume material which has been experimentally found to govern the plume angle and spread [2, 129]. It is also possible that the Sedov-Taylor fit model is affected by the weighting of the data in the model fit, since the dimensionality factor is know to be a function of time and is variable over the overall fit. Since the Sedov-Taylor model only takes into account the forward motion of the shock wave in that the shock points that form the fitted trajectory are only described by the points normal to the target surface, it is possible that using the Sedov-Taylor model to approximate shock wave dimensionality in the case of a non-spherical ( $n \neq 3$ ) shock wave is too rough an approximation to characterize the actual dimensionality of the shock structure in the experimental cases.

#### **5.3.4 Circular Spot Shock Morphology**

Schlieren imaging was used to produce the images in Fig. 36, which reveals the shock wave morphology for ablation of graphite in nitrogen at 10 Torr for a circular laser footprint, for gate delays from 6.3  $\mu\text{s}$  to 20  $\mu\text{s}$ . Like the previous images, the shock wave is evidenced by the dark shadow caused a localized gradient in the index of refraction. The bright emissive plume is visible in the earlier images as a white central region above the target surface. The apparent size differences of the emissive plume in the images is partly due to the image contrast adjustments required to enhance the visibility of the shock wave in

the image. As before, hemispheres centered at the target are superimposed on the images. Unlike in the emissive plume imagery comparison, the shock waves for the circular laser spot show similar propagation distances to the rectangular shock waves especially at later times  $\sim 20 \mu\text{s}$ . The shock waves have slowed down to similar velocities for both cases at these later times. The shock curvature at 45 degrees is similar at each gate delay, with minimal change to the distance of the shock wave across the temporal propagation of the shock wave.

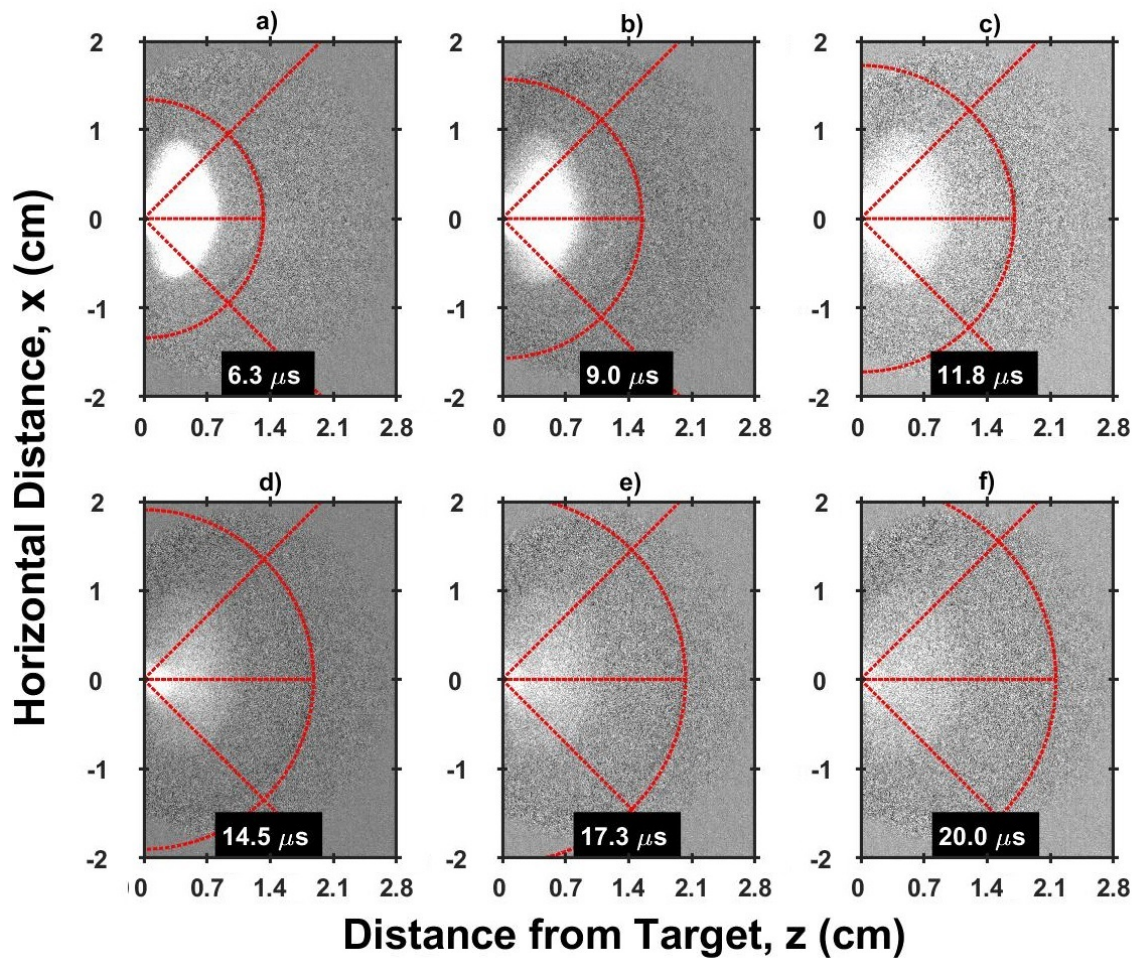


**Figure 36:** Schlieren ICCD image series demonstrating shock wave morphology for ablation of graphite in nitrogen at 10 Torr for a circular laser footprint with gate delays from  $6.3 \mu\text{s}$  to  $20 \mu\text{s}$ .

Figure 37 show the circular spot schlieren imagery at gate delay of  $t = 14.5 \mu\text{s}$  in nitrogen, argon, and  $\text{CO}_2/\text{N}_2$  with pressures ranging from 3–180 Torr. Like the rectangular

imagery, the shock wave is visibly darker and more prominent in the 180 Torr gas cases, with the index gradient fading in magnitude as pressure is decreased. The shock imagery shows a slower shock wave propagation for the higher pressure gas cases with the least progression evident in the CO<sub>2</sub>/N<sub>2</sub> gas. The propagation in nitrogen and argon background gases is similar at similar pressures, as is the curvature of the plume at the 45 degree angle points. At angles less than 45 degrees, the shock waves continue to deviate from a spherical, however the deviation is less pronounced than in the rectangular schlieren imagery. The emissive plumes in the circular schlieren imagery extend a shorter distance outwards from the target surface than the plumes in the the rectangle imagery,

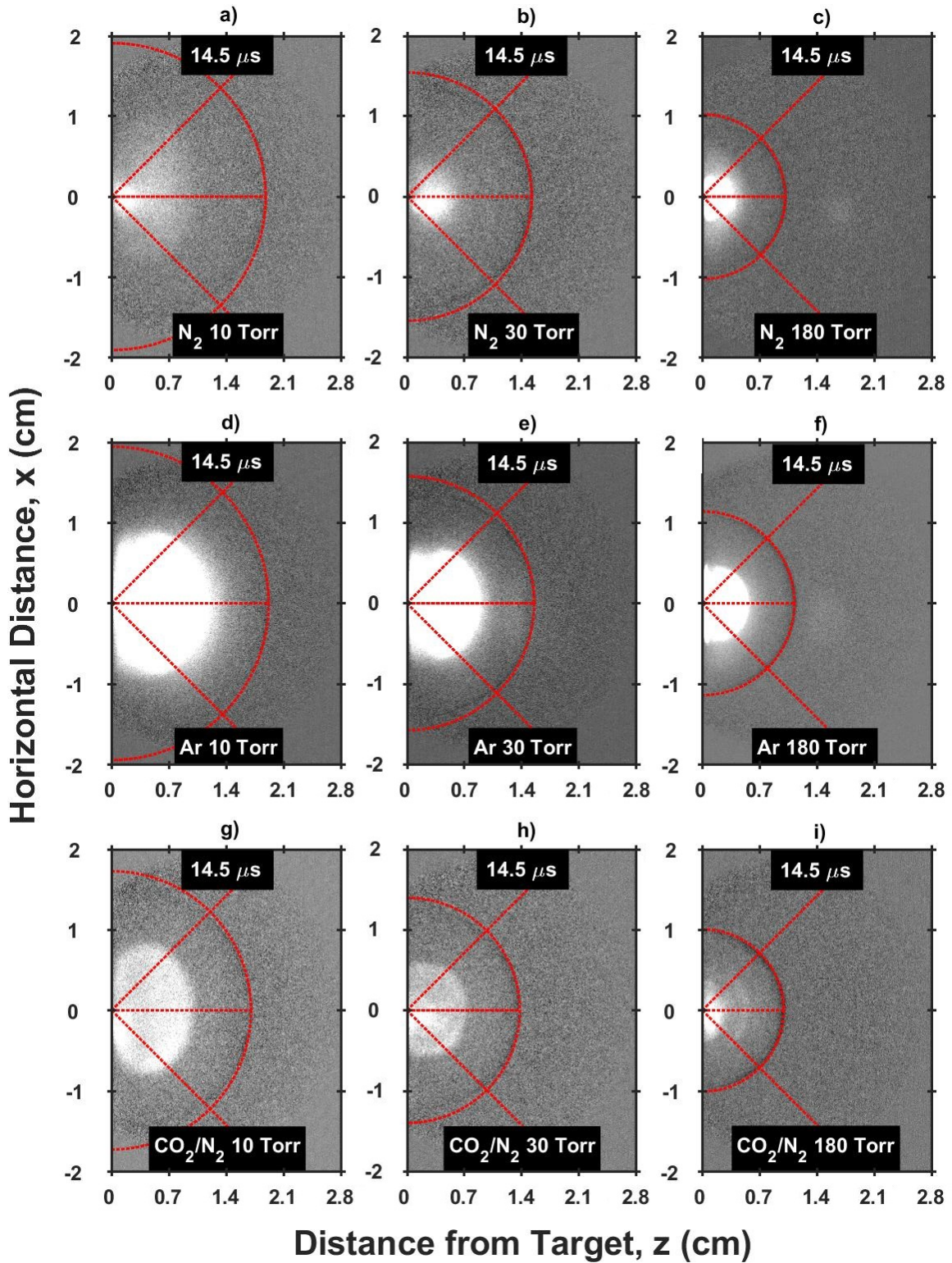


**Figure 37:** Schlieren image series at  $t = 14.5 \mu\text{s}$  demonstrating shock wave morphology for ablation of graphite in nitrogen (a–c), argon (d–f), and 70%  $\text{CO}_2$ /30%  $\text{N}_2$  (g–i), for a circular laser footprint in pressures ranging from 10 to 180 Torr.

As before, the radius of curvature ratio was calculated by finding the distance from the target to the shock wave along the 45 degree line, and dividing by the distance of the target to the shock wave along the normal 90 degree line. Table 11 gives the curvature ratio from the circular spot shock wave imagery and compares it to the Sedov-Taylor dimensionality parameter. The dimensionality values for the circular spot were calculated in Chapter 4. Like the rectangular comparison, the circular Sedov-Taylor dimensionality reveal shock waves approaching spherical dimensionality as the pressure is decreased. The highest pressure cases show a dimensionality between cylindrical ( $n = 2$ ) and spherical ( $n = 3$ ) geometry, tending towards a more cylindrical shock wave especially in the  $\text{CO}_2/\text{N}_2$  and argon gases. The lower pressures progress towards a mix of spherical dimensionality and cylindrical dimensionality with the 10 Torr cases trending closer to spherical. At  $n = 2.98 \pm 0.03$ , the 10 Torr  $\text{CO}_2/\text{N}_2$  case exhibited a nearly spherical Sedov-Taylor dimensionality factor. The circular spot radius of curvature ratios show the same reverse trend as the rectangular ratios, where the highest pressure cases exhibit the more spherical radius of curvature ratios.

**Table 11:** Circular laser spot Sedov-Taylor dimensionality and radius of curvature ratio for ablation shock wave.

Gas	Pressure (Torr)	Sedov-Taylor Dimensionality, $n$	Curvature Ratio
N <sub>2</sub>	180	2.44 ± 0.08	0.95 ± 0.01
N <sub>2</sub>	30	2.92 ± 0.05	0.95 ± 0.01
N <sub>2</sub>	10	2.91 ± 0.03	0.89 ± 0.02
Ar	180	2.35 ± 0.06	0.97 ± 0.01
Ar	30	2.64 ± 0.04	0.95 ± 0.01
Ar	10	2.86 ± 0.03	0.94 ± 0.01
CO <sub>2</sub> /N <sub>2</sub>	180	2.35 ± 0.06	0.97 ± 0.01
CO <sub>2</sub> /N <sub>2</sub>	30	2.87 ± 0.06	0.95 ± 0.01
CO <sub>2</sub> /N <sub>2</sub>	10	2.98 ± 0.03	0.93 ± 0.01

## 5.4 Conclusions

Pulsed laser ablation of pyrolytic graphite with a 5.7 J/cm<sup>2</sup> frequency-doubled Nd:YAG laser in backgrounds of argon, nitrogen, and mixed gas at pressures from 3–180 Torr was performed to explore morphology of the plume emissive contact front and ablation shock wave. Fast gated and schlieren shock wave imagery was used to explore emissive plume morphology and shock wave propagation for a rectangular laser spot and a circular laser spot. The view of the short x-axis of the rectangular laser spot revealed significant plume confinement by the background gas at higher pressures, while exhibiting larger tails and plume spreading as pressures are decreased. The horizontal distribution of plume material is evident in the view of the long y-axis, with locally denser regions of plume emission visible, possibly due to uneven ablation within the laser spot footprint, as the plume propagates away from the target and interacts with the background gas. Significant differences were found between the appearances of the emissive plume for circular and rectangular laser spots. The viewing angle of a non-circular plume revealed significantly different plume shapes and temporal progressions between the long and short axes of the rectangular spots viewed by the camera. The short axis rectangle spot plume was similar in appearance to

the circular spot plume, however, the circular plume propagated through the background gas at a significantly higher velocity.

The morphology of the rectangular and circular spot plumes and shock waves are compared using the emissive imagery, and the shock waves were characterized using the Sedov-Taylor blast model to examine dimensionality. In addition, the radii of curvature ratios for the shock wave were calculated. The shock imagery for both the rectangular and circular spots were found to trend more towards spherical dimensionality as pressure was decreased, while the curvature ratios exhibited the opposite trend.

Further experimental studies should be performed to better characterize the relationships between the emissive plumes and the shock waves generated by pulsed ablation of graphite and other target materials. In addition, further exploration of the effects of laser wavelength and temporal laser-plume coincidence on graphite plume propagation would better establish the conditions that dominate plume dynamics. The present survey of plume and shock wave morphology is necessary for improving understanding of emissive contact front and shock wave propagation dynamics, which would lead to improved predictive capabilities for characterizing laser-target interactions.

## VI. Conclusions

### 6.1 Conclusions

Pulsed laser ablation has been studied with the aim of improving the interpretation of common diagnostic techniques used to characterize pulsed laser ablation, to find simple but universal scaling relationships for comparing ablation dynamics across different target materials and ablation conditions, and to provide a comprehensive and systematic analysis of emissive plume and shock wave dynamics for graphite. A mid-level goal of this work was to establish a comprehensive and high-fidelity data set of graphite plumes and shock waves that will be of use in validating laser ablation models since graphite has been studied less than other target materials, thus filling a niche in the literature. To accomplish that end, three graphite ablation experiments were performed using fast gated emission imaging and schlieren imaging to capture plume and shock propagation dynamics in helium, nitrogen, argon, and 70% CO<sub>2</sub> 30%N<sub>2</sub> mixed gas in a range of pressures from the low-pressure regime at 1 Torr up to the high-pressure regime at 180 Torr. Multiple laser parameters were utilized including 248 nm and 532 nm ablation laser sources, rectangular and circular laser spot geometries, and fluences from 4–5.7 J/cm<sup>2</sup>.

In Chapter 3, pulsed laser ablation of graphite was performed to find and validate new scaling relationships for common ablation diagnostic parameters. Initial plume expansion velocities of 1.37–1.98 cm/μs corresponded to plume kinetic energies between 12–25 eV/atom. The Sedov-Taylor energy released in the sudden ablation was typically 33% of the laser pulse energy. An examination of the normalized shock thickness and shock strength ( $M \sim 48$ ) for the graphite emissive plume was compared to prior ablation studies and to 1-D shock tube studies ( $M \leq 10$ ) using a commonly used analytical model. The analytical theory was found to under predict normalized shock thickness for the high Mach numbers seen in pulsed laser ablation with significant deviation for  $M > 35$ . In addition,

the graphite data was used to validate a recently proposed method using non-dimensional factors for hole depth, fluence, and pulse duration, and the present results were found to be consistent with the prior data which included target materials such as metals and semiconductors, but did not include graphite. The graphite non-dimensional results filled in the low non-dimensional fluence region where the previous data was sparse, increasing the size of validated materials and conditions for the non-dimensional comparison. Most importantly, a new scaling method for the Sedov-Taylor blast energy to laser energy ratio was developed and validated, enabling comparisons of laser-plume energy coupling between different target materials ablated under varying environmental and system conditions. Blast energy and plume dimensionality were found to be correlated with stopping distances, which are typically greater than  $10^3$  mean free paths. The energy ratio scaling was validated over a broad range of studies despite differences in wavelength, pulse duration, fluence and target material. As a result, the scaling of Sedov-Taylor energy can be used by future researchers for comparing emissive plume parameters across many materials and conditions.

In Chapter 4, pulsed laser ablation of graphite was performed to develop and validate an improvement to Sedov-Taylor laser-plume energy analysis, a common laser ablation diagnostic technique. Graphite was ablated with a pulsed frequency-doubled Nd:YAG laser with a  $5.70 \text{ J/cm}^2$  in argon, nitrogen, and mixed gas backgrounds from 3–180 Torr. Initial plume expansion velocities of 1.9–3.45 cm/ $\mu\text{s}$  corresponding to kinetic energies between 26–74 eV/atom. White light schlieren imaging and optical emission imaging with a fast-gated ICCD camera were used to determine the conditions and location for shock detachment. Sedov-Taylor analyses of emissive plumes depend on the sectioning of the plume trajectory data since the model was created to predict the blast energy in a shock wave. If the model is fit to a portion of the plume trajectory that is not shock-like, it can over or under predict shock energies depending on where the fit is terminated. In addition, the Sedov-Taylor dimensionality factor is an average of a time dependent variable and can

dramatically change if some or all of the emissive plume drag region is included in the fit, which negatively affects the accuracy of energy estimates. As a result, Sedov-Taylor analysis has not reliably given energy estimates that scale with pressure or other factors in a coherent way across pulsed laser ablation literature. To resolve these difficulties, shock detachment positions were characterized and used to define a new high limit for sectioning emissive plume data during Sedov-Taylor analysis. A robust Sedov-Taylor analysis study was performed for both the emissive plumes and the shock waves, and the results for the Sedov-Taylor dimensionality parameters, energies, and  $a$ -coefficients were compared for the full trajectories and the detachment-limited trajectories. Shock detachment typically occurs at 80–85% of the plume stopping distance. This limit is significantly closer than the Sedov-Taylor high limit. Limiting the Sedov-Taylor fit with shock detachment enables more reliable laser-plume coupling energy estimates, providing a more meaningful interpretation of the laser energy deposited into the plume. Shock detachment can be used to enhance plume diagnostics of other laser ablation target materials as well. The shock detachment technique was validated over a range of experimental conditions, with detachment-limited Sedov-Taylor energy calculations for the emissive plume in agreement with the shock wave energy values to within 3–5%. The improved emissive plume blast energy estimates ranged from 55–75% of the laser pulse energy. Shock detachment was found to scale with mean free path, which supports the potential for prediction of shock detachment in other pressures and gases. Shock detachment points can be used to improve laser-plume energy estimates for any target material where a Sedov-Taylor analysis is performed.

In Chapter 5, pulsed laser ablation of graphite was performed to examine the morphology of emissive plumes and corresponding ablation shock waves. Graphite was ablated with a pulsed  $5.70 \text{ J/cm}^2$  frequency-doubled Nd:YAG laser in argon, nitrogen, and mixed gas backgrounds from 3–180 Torr. An analysis comparing laser rectangular and circular

spot geometries was explored using white light schlieren shock wave imaging and fast-gated optical emission imaging. The imagery was used to determine how plume and shock wave expansion depends on laser footprint geometry and aspect ratio. The aspect ratio of the rectangular spot was approximately 1:11, and the viewing angle of the rectangular spot plume greatly affected the apparent plume shape as viewed by the ICCD camera. The view of the long y-axis yielded an elongated emissive plume with initial dimensions approximately matching the 4.2 mm spot width. Localized knots of increased emission were evident in the y-axis view of the plume, possibly from uneven ablation resulting in varying plume densities. Since the long y-axis emissive plume is stretched out considerably compared to the short x-axis plume, plume diagnostics and model fitting using imagery from that field of view will be much more sensitive to the initial ablation conditions. The short axis plume was considerably closer in shape to the circular spot plume, and provides a much better target for consistent plume trajectory analysis and subsequent expansion fitting. The emissive plume from the circular spot propagated through the background gases with significantly greater velocities than the rectangular spot plumes, most likely due to a more hydrodynamic shape as it propagated through the background gas as compared to the blunt rectangular plumes. In addition, the circular spot plume showed evidence of plume splitting with an apparent rebounded emission feature occurring at later times, possibly due to a late faster plume component colliding with and then rebounding off an earlier slow component. Finally, radii of curvature ratios were developed using shock wave imagery for each geometry and compared to the Sedov-Taylor model dimensionality fit parameter,  $n$ . Combined with the findings from Chapter 3 and Chapter 4, the plume morphology study completes a comprehensive and systematic analysis of emissive plume and shock wave dynamics for graphite over a large range of environmental and laser source conditions.

There is still much work to be done in order to fully characterize plume and shock wave dynamics during pulsed laser ablation of graphite and other target materials. How-

ever, during this effort, we developed and validated a significant diagnostic improvement to Sedov-Taylor analysis energy estimates that can be useful for all target materials, we discovered and verified a new plume-laser energy scaling that allows for the direct comparison of different target materials under different ablation conditions, and we provided a comprehensive and systematic analysis of emissive plume and shock wave dynamics for graphite over a large range of conditions. Furthermore, the graphite plume and shock dynamics and parameters captured in this work are useful as high-fidelity benchmarks for validating current and future laser effects models used for industrial process control monitoring, battle damage assessment, and graphite material characterization.

The next section includes recommendations for additional experimental studies that would further the state of the art in understanding and predicting the effects of pulsed laser ablation on graphite and other materials.

## **6.2 Recommendations for Future Work**

An examination of shock front detachment for a wider array of target materials, laser parameters, pressures, and background gases would dramatically increase the understanding of the variables that affect shock detachment, and lead to the development of an analytical model for predicting shock detachment under all conditions. This would enable an increase in the accuracy of laser-plume energy coupling estimates via Sedov-Taylor analysis and improve understanding of the effects of laser-plume coupling on plume propagation. Next, the first-order ablated mass and hole depth estimation using initial velocities could be validated with crater volume measurements using confocal microscopy and precision weighing of samples. Ablation experiments focusing on differences in gas viscosities and thermal properties to include Reynolds numbers could help to further collapse dimensionality of the shock strength versus Mach number relationship and allow for a clearer comparison between different target materials and conditions. Experimental studies should

be performed to better characterize the relationships between the emissive plumes and the shock waves generated by pulsed ablation of graphite and other target materials. Finally, the numerous results from this dissertation could be used to validate existing and future ablation models such as the Directed Energy Illumination Visualization (DEIVI) physics-based laser ablation model [130].

In addition to improvements to the research presented in this dissertation, many other avenues of research are possible, three of which are presented in brief here. First, an exploration of the effects of Nd:YAG versus KrF laser ablation on shock propagation could be conducted to examine the effects of the two very different laser sources on shock propagation. It would also be interesting to compare the effects of Nd:YAG graphite emissive and non-emissive plume dynamics using laser induced fluorescence or absorption imaging spectroscopy. Next, the graphite ablation target could be doped with potassium or other elements with different emission wavelengths to facilitate improved species isolation for the analysis of plume dynamics and allow for enhanced detection and characterization of non-emissive plume species.

Finally, tens of thousands of graphite pulsed laser ablation emissive plume and schlieren shock wave images (over 500 GB of data) were captured for a range of environmental and laser parameters including ablation at 248 nm, 532 nm, and 1064 nm laser wavelengths and both single and temporally-spaced double pulses. This vast trove of data could be mined for a wealth of insights into pulsed laser ablation of graphite and laser ablation process in general, the analyses of which could lead to greater understanding and characterization of overall ablation plume and shock wave dynamics. It is clear that a significant amount of work remains to be accomplished towards reaching the goal of a full and complete understanding of pulsed laser ablation dynamics.

## Bibliography

1. J. G. Jones and A. A. Voevodin, "Magnetron sputter pulsed laser deposition: technique and process control developments," *Surface and Coatings Technology*, vol. 184, no. 1, pp. 1–5, 2004.
2. D. B. Chrisey and G. K. Hubler, Eds., *Pulsed Laser Deposition of Thin Films*. New York: J. Wiley, 1994, pp. 144–157.
3. M. W. Stapleton, A. P. McKiernan, and J.-P. Mosnier, "Expansion dynamics and equilibrium conditions in a laser ablation plume of lithium: Modeling and experiment," *Journal of Applied Physics*, vol. 97, no. 6, p. 064 904, Mar. 2005.
4. L. I. Sedov, *Similarity and dimensional methods in mechanics*. New York: Academic Press, 1959.
5. G. I. Taylor, "The formation of a blast wave by a very intense explosion," *Proceedings of the Royal Society of London. Series A. Mathematical and Physical Sciences*, vol. 201, no. 1065, pp. 159–174, 1950.
6. M. Elayaperumal, K. Gnanasekaran, M. K. Moodley, B. W. Mwakikunga, R. Gaur, S. Umapathy, R. Ladchumananandasivam, and M. Maaza, "Ultrananocrystalline diamond-like carbon (un-dlc) assembled on epitaxial zno film by pld technique and sims raman rutherford spectroscopic fingerprint investigation," *Journal of Raman Spectroscopy*,

7. U. Baig, A. Khan, M. Gondal, M. Dastageer, and S. Akhtar, "Single-step synthesis of silicon carbide anchored graphitic carbon nitride nanocomposite photocatalyst for efficient photoelectrochemical water splitting under visible-light irradiation," *Colloids and Surfaces A: Physicochemical and Engineering Aspects*, vol. 611, p. 125 886, 2021.
8. M. Natali, J. M. Kenny, and L. Torre, "Science and technology of polymeric ablative materials for thermal protection systems and propulsion devices: A review," *Progress in Materials Science*, vol. 84, pp. 192–275, 2016.
9. B. Anderberg and M. L. Wolbarsht, *Laser Weapons*, 1st ed. New York: Springer US, 1992.
10. G. P. Perram, S. J. Cusumano, S. T. Fiorino, and R. L. Hengehold, *An introduction to laser weapon systems*. Albuquerque, New Mexico: Directed Energy Professional Society, 2010.
11. T. A. Van Woerkom, G. P. Perram, B. D. Dolasinski, C. D. Phelps, and P. A. Berry, "Laser ablation of metals and semiconductors with 100 ps to 100  $\mu$ s pulses," *Optical Engineering*, vol. 58, no. 08, p. 1, 2019.
12. S. J. Henley, J. D. Carey, S. R. Silva, G. M. Fuge, M. N. Ashfold, and D. Anglos, "Dynamics of confined plumes during short and ultrashort pulsed laser ablation of graphite," *Physical Review B - Condensed Matter and Materials Physics*, vol. 72, no. 20, pp. 1–13, 2005.

13. S. Abdelli-Messaci, T. Kerdja, A. Bendib, S. M. Aberkane, S. Lafane, and S. Malek, "Investigation of carbon plasma species emission at relatively high KrF laser fluences in nitrogen ambient," *Applied Surface Science*, vol. 252, no. 5, pp. 2012–2020, 2005.
14. Y. Yamagata, A. Sharma, J. Narayan, R. M. Mayo, J. W. Newman, and K. Ebihara, "Optical emission study of ablation plasma plume in the preparation of diamond-like carbon films by KrF excimer laser," *Journal of Applied Physics*, vol. 86, no. 8, pp. 4154–4159, 1999.
15. T. Ikegami, S. Ishibashi, Y. Yamagata, K. Ebihara, R. K. Thareja, and J. Narayan, "Spatial distribution of carbon species in laser ablation of graphite target," *Journal of Vacuum Science & Technology A: Vacuum, Surfaces, and Films*, vol. 19, no. 4, pp. 1304–1307, 2001.
16. Z. Zelinger, M. Novotný, J. Bulíř, J. Lančok, P. Kubát, and M. Jelínek, "Laser plasma plume kinetic spectroscopy of the nitrogen and carbon species," *Contributions to Plasma Physics*, vol. 43, no. 7, pp. 426–432, 2003.
17. K. F. Al-Shboul, S. S. Harilal, A. Hassanein, and M. Polek, "Dynamics of C<sub>2</sub> formation in laser-produced carbon plasma in helium environment," *Journal of Applied Physics*, vol. 109, no. 5, p. 053 302, 2011.
18. S. S. Harilal, A. Hassanein, and M. Polek, "Late-time particle emission from laser-produced graphite plasma," *Journal of Applied Physics*, vol. 110, no. 5, pp. 1–5, 2011.

19. N. M. Bulgakova and A. V. Bulgakov, "Pulsed laser ablation of solids: Transition from normal vaporization to phase explosion," *Applied Physics A: Materials Science and Processing*, vol. 73, no. 2, pp. 199–208, 2001.
20. R. K. Thareja, R. K. Dwivedi, and K. Ebihara, "Interaction of ambient nitrogen gas and laser ablated carbon plume: Formation of CN," *Nuclear Instruments and Methods in Physics Research, Section B: Beam Interactions with Materials and Atoms*, 2002.
21. H. Yousfi, S. Abdelli-Messaci, O. Ouamerali, and A. Dekhira, "A comparative study of carbon plasma emission in methane and argon atmospheres," *Spectrochimica Acta - Part B Atomic Spectroscopy*, vol. 142, pp. 97–107, 2018.
22. S. S. Harilal, C. V. Bindhu, V. P. Nampoory, and C. P. Vallabhan, "Influence of ambient gas on the temperature and density of laser produced carbon plasma," *Applied Physics Letters*, vol. 72, no. 2, pp. 167–169, 1998.
23. S. S. Harilal, "Expansion dynamics of laser ablated carbon plasma plume in helium ambient," *Applied Surface Science*, vol. 172, no. 1-2, pp. 103–109, 2001.
24. A. Kushwaha and R. K. Thareja, "Dynamics of laser-ablated carbon plasma: formation of C<sub>2</sub> and CN," *Applied Optics*, vol. 47, no. 31, G65–G67, 2008.
25. C. Ursu, P. Nica, B. Rusu, and C. Focsa, "V-shape plasma generated by excimer laser ablation of graphite in argon: Spectroscopic investigations," *Spectrochimica Acta Part B: Atomic Spectroscopy*, vol. 163, no. January 2020, p. 105 743, 2020.

26. C. Ursu, P. Nica, C. Focsa, and M. Agop, "Fractal method for modeling the peculiar dynamics of transient carbon plasma generated by excimer laser ablation in vacuum," *Complexity*, vol. 2018, 2018.
27. C. Ursu, P. Nica, and C. Focsa, "Excimer laser ablation of graphite: The enhancement of carbon dimer formation," *Applied Surface Science*, vol. 456, no. June, pp. 717–725, 2018.
28. K. F. Al-Shboul, S. S. Harilal, and A. Hassanein, "Spatio-temporal mapping of ablated species in ultrafast laser-produced graphite plasmas," *Applied Physics Letters*, vol. 100, no. 22, pp. 3–6, 2012.
29. K. F. Al-Shboul, S. S. Harilal, and A. Hassanein, "Gas dynamic effects on formation of carbon dimers in laser-produced plasmas," *Applied Physics Letters*, vol. 99, no. 13, p. 131 506, Sep. 2011.
30. K. F. Al-Shboul, S. S. Harilal, and A. Hassanein, "Emission features of femtosecond laser ablated carbon plasma in ambient helium," *Journal of Applied Physics*, vol. 113, no. 16, p. 163 305, Apr. 2013.
31. J. J. Camacho, L. Díaz, M. Santos, L. J. Juan, and J. M. Poyato, "Temporal evolution of the laser-induced plasma generated by IR CO<sub>2</sub> pulsed laser on carbon targets," *Journal of Applied Physics*, vol. 106, no. 3, 2009.
32. J. J. Camacho, M. Santos, L. Díaz, and J. M. Poyato, "Spatial characterization of the laser-induced plasma plumes generated by IR CO<sub>2</sub> pulsed laser on carbon targets,"

- Applied Physics A: Materials Science and Processing*, vol. 94, no. 2, pp. 373–380, 2009.
33. J. J. Camacho, L. Díaz, M. Santos, D. Reyman, and J. M. Poyato, “Optical emission spectroscopic study of plasma plumes generated by IR CO<sub>2</sub> pulsed laser on carbon targets,” *Journal of Physics D: Applied Physics*, vol. 41, no. 10, 2008.
  34. A. M. Keszler and L. Nemes, “Time averaged emission spectra of Nd:YAG laser induced carbon plasmas,” *Journal of Molecular Structure*, vol. 695-696, pp. 211–218, 2004.
  35. T. I. Calver, W. A. Bauer, C. A. Rice, and G. P. Perram, “Shock front behavior during pulsed laser ablation of graphite,” *Optical Engineering*, vol. 60, no. 5, pp. 1–20, 2021.
  36. A. M. Fox, *Optical Properties of Solids*, ser. Oxford master series in condensed matter physics. Oxford University Press, 2001.
  37. W. Demtröder, *Laser Spectroscopy 2: Experimental Techniques*. Springer Berlin Heidelberg, 2015.
  38. V. Letokhov, *Laser Photoionization Spectroscopy*. Orlando, FL: Harcourt Brace Jovanovich, 1987.
  39. A. Gold and H. B. Bebb, “Theory of multiphoton ionization,” *Phys. Rev. Lett.*, vol. 14, pp. 60–63, 3 Jan. 1965.
  40. D. A. Gurnett and A. Bhattacharjee, *Introduction to plasma physics: with space and laboratory applications*. Cambridge university press, 2005.

41. G. T. Phillips, W. A. Bauer, C. D. Fox, A. E. Gonzales, N. C. Herr, R. C. Gosse, and G. P. Perram, "Mass removal by oxidation and sublimation of porous graphite during fiber laser irradiation," *Optical Engineering*, vol. 56, no. 1, p. 11 013, 2016.
42. J. Rumble, Ed., *CRC handbook of chemistry and physics*, 98th ed. Boca Raton: CRC Press, 2017.
43. M. Stafe, N. Niculae, and A. Marcus, *Pulsed laser ablation of solids*, 1st ed. Berlin Heidelberg: Springer Science & Business Media, 2014, pp. 143–188.
44. A. A. Ionin, S. I. Kudryashov, and L. V. Seleznev, "Near-critical phase explosion promoting breakdown plasma ignition during laser ablation of graphite," *Physical Review E - Statistical, Nonlinear, and Soft Matter Physics*, vol. 82, no. 1, pp. 1–9, 2010.
45. S. Sinha, "Nanosecond laser ablation of graphite: A thermal model based simulation," *Journal of Laser Applications*, vol. 30, no. 1, p. 012 008, 2018.
46. M. Lenner, A. Kaplan, C. Huchon, and R. E. Palmer, "Ultrafast laser ablation of graphite," *Physical Review B - Condensed Matter and Materials Physics*, vol. 79, no. 18, pp. 1–11, 2009.
47. M. Lenner, A. Kaplan, and R. E. Palmer, "Nanoscale Coulomb explosion in ultrafast graphite ablation," *Applied Physics Letters*, vol. 90, no. 15, pp. 15–18, 2007.
48. D. L. Wiggins, C. T. Raynor, and J. A. Johnson, "Evidence of inverse bremsstrahlung in laser enhanced laser-induced plasma," *Physics of Plasmas*, 2010.

49. J. Vadillo, J. Fernandez Romero, C. Rodriguez, and J. Laserna, "Effect of plasma shielding on laser ablation rate of pure metals at reduced pressure," *Surface and Interface Analysis*, vol. 27, no. 11, pp. 1009–1015, 1999.
50. A. E. Hussein, P. K. Diwakar, S. S. Harilal, and A. Hassanein, "The role of laser wavelength on plasma generation and expansion of ablation plumes in air," *Journal of Applied Physics*, vol. 113, no. 14, p. 143 305, 2013.
51. P. Schaaf, *Laser processing of materials: fundamentals, applications and developments*. Springer Science & Business Media, 2010, vol. 139.
52. C. Phelps, C. J. Druffner, G. P. Perram, and R. R. Biggers, "Shock front dynamics in the pulsed laser deposition of YBa 2Cu3O7-x," *Journal of Physics D: Applied Physics*, vol. 40, no. 15, pp. 4447–4453, 2007.
53. D. B. Geohegan and A. A. Puretzky, "Species-resolved imaging and gated photon counting spectroscopy of laser ablation plume dynamics during KrF- and ArF-laser PLD of amorphous diamond films," in *Materials Research Society Symposium - Proceedings*, 1996.
54. W. A. Bauer, "Laser Heating of Graphite and Pulsed Laser Ablation of Titanium and Aluminum," Ph.D. dissertation, Air Force Institute of Technology, 2017.
55. A. Misra and R. K. Thareja, "Investigation of laser ablated plumes using fast photography," *IEEE Transactions on Plasma Science*, vol. 27, no. 6, pp. 1553–1558, 1999.

56. W. Bauer, G. Perram, and T. Haugan, "Plume dynamics from UV pulsed ablation of Al and Ti," *Laser-Induced Damage in Optical Materials 2016*, vol. 10014, no. December 2016, 100140S, 2016.
57. Stanford Computer Optics, *Time Resolved Spectroscopy with ICCD cameras*.
58. G. S. Settles, *Schlieren and Shadowgraph Techniques: Visualizing Phenomena in Transparent Media*, 1st ed. Berlin Heidelberg: Springer, 2001.
59. F. Claeysens, M. N. Ashfold, E. Sofoulakis, C. G. Ristoscu, D. Anglos, and C. Fotakis, "Plume emissions accompanying 248 nm laser ablation of graphite in vacuum: Effects of pulse duration," *Journal of Applied Physics*, vol. 91, no. 9, pp. 6162–6172, 2002.
60. D. Diaz and D. W. Hahn, "Plasma chemistry produced during laser ablation of graphite in air, argon, helium and nitrogen," *Spectrochimica Acta - Part B Atomic Spectroscopy*, vol. 166, p. 105 800, 2020.
61. A. A. Puretzky, D. B. Geohegan, R. E. Haufler, R. L. Hettich, X.-Y. Zheng, and R. N. Compton, "Laser ablation of graphite in different buffer gases," in *AIP Conference Proceedings*, American Institute of Physics, vol. 288, AIP, 1993, pp. 365–374.
62. P. E. Nica, C. Ursu, and C. Focsa, "Electrical characterization of carbon plasma generated by excimer laser ablation of graphite," *Applied Surface Science*, vol. 540, p. 148 412, 2021.

63. P. E. Nica, C. Ursu, and C. Focsa, “Long-range oscillations of a laser-produced carbon plasma recorded by an electrostatic energy analyzer,” *Journal of Applied Physics*, vol. 129, no. 5, p. 53 305, 2021.
64. R. P. Singh, S. L. Gupta, and R. K. Thareja, “Optical probe investigation of laser ablated carbon plasma plume in nitrogen ambient,” *Physics of Plasmas*, vol. 20, no. 12, 2013.
65. G. Ben-Dor, O. Igra, and T. Elperin, *Handbook of Shock Waves, Volume 2. Shock wave interactions and propagation*. Academic Press, New York, 2001.
66. M. Camac, “Argon shock thickness,” *The Physics of Fluids*, vol. 7, no. 7, pp. 1076–1078, 1964.
67. E. F. Greene and D. F. Hornig, “The shape and thickness of shock fronts in argon, hydrogen, nitrogen, and oxygen,” *The Journal of Chemical Physics*, vol. 21, no. 4, pp. 617–624, 1953.
68. G. M. Kremer and I. Müller, “Shock thickness in monatomic gases,” *Meccanica*, vol. 32, no. 4, pp. 295–299, 1997.
69. M. Linzer and D. F. Hornig, “Structure of shock fronts in argon and nitrogen,” *The Physics of Fluids*, vol. 6, no. 12, pp. 1661–1668, 1963.
70. A. H. Shapiro, *The dynamics and thermodynamics of compressible fluid flow*, Vol 1. John Wiley & Sons, 1953.

71. S. George, R. K. Singh, V. P. N. Nampoory, and A. Kumar, "Fast imaging of the laser-blow-off plume driven shock wave: Dependence on the mass and density of the ambient gas," *Physics Letters A*, vol. 377, no. 5, pp. 391–398, 2013.
72. W. Bauer and G. Perram, "Laser ablated Ti velocity distribution dynamics," *JOSA B*, vol. 35, no. 10, B27–B37, 2018.
73. G. A. Askar'yan, M. S. Rabinovich, M. M. Savchenko, and V. K. Stepanov, "Optical Breakdown" Fireball" in the Focus of a Laser Beam," *ZhETF Pisma Redaktsiiu*, vol. 5, p. 121, 1967.
74. J. M. Gordon, K. C. Gross, and G. P. Perram, "Fireball and shock wave dynamics in the detonation of aluminized novel munitions," *Combustion, Explosion, and Shock Waves*, vol. 49, no. 4, pp. 450–462, 2013.
75. F. Kokai, K. Takahashi, K. Shimizu, M. Yudasaka, and S. Iijima, "Shadowgraphic and emission imaging spectroscopic studies of the laser ablation of graphite in an Ar gas atmosphere," *Applied Physics A Materials Science & Processing*, vol. 69, S223–S227, 1999.
76. M. Eliceiri and C. P. Grigoropoulos, "Comparison of transient absorption of laser ablation plasma with fundamental plasma absorption relations," *Applied Physics A: Materials Science and Processing*, vol. 127, no. 7, pp. 1–10, 2021.
77. X. Li, W. Wei, J. Wu, S. Jia, and A. Qiu, "The Influence of spot size on the expansion dynamics of nanosecond-laser-produced copper plasmas in atmosphere," *Journal of Applied Physics*, vol. 113, no. 24, pp. 1–6, 2013.

78. S. S. Harilal, C. V. Bindhu, M. S. Tillack, F. Najmabadi, and A. C. Gaeris, "Internal structure and expansion dynamics of laser ablation plumes into ambient gases," *Journal of Applied Physics*, vol. 93, no. 5, pp. 2380–2388, 2003.
79. S. S. Harilal, P. K. Diwakar, M. P. Polek, and M. C. Phillips, "Morphological changes in ultrafast laser ablation plumes with varying spot size," *Optics Express*, vol. 23, no. 12, p. 15 608, 2015.
80. S. S. Harilal, N. Farid, J. R. Freeman, P. K. Diwakar, N. L. LaHaye, and A. Hassanein, "Background gas collisional effects on expanding fs and ns laser ablation plumes," *Applied Physics A: Materials Science and Processing*, vol. 117, no. 1, pp. 319–326, 2014.
81. J. F. Maguire, J. D. Busbee, D. C. Liptak, D. P. Lubbers, S. R. LeClair, and R. R. Biggers, "Process control for pulsed laser deposition using Raman spectroscopy," 2000.
82. N. I. U. Qinglin, Y. Zhichao, C. Biao, and D. Shikui, "Infrared radiation characteristics of a hypersonic vehicle under time-varying angles of attack," *Chinese Journal of Aeronautics*, vol. 32, no. 4, pp. 861–874, 2019.
83. J. Teichman and L. Hirsch, "Visible signatures of hypersonic reentry," *Journal of Spacecraft and Rockets*, vol. 51, no. 3, pp. 815–822, 2014.
84. N. C. Herr, A. E. Gonzales, and G. P. Perram, "Kinetics, evolving thermal properties, and surface ignition of carbon fiber reinforced epoxy composite during laser-induced decomposition," *Polymer Degradation and Stability*, vol. 152, pp. 147–161, 2018.

85. Z. Márton, P. Heszler, A. Mechler, B. Hopp, Z. Kántor, and Z. Bor, "Time-resolved shock-wave photography above 193-nm excimer laser-ablated graphite surface," *Applied Physics A*, vol. 69, no. 1, S133–S136, 1999.
86. M. D. Shirk and P. A. Molian, "Ultra-short pulsed laser ablation of highly oriented pyrolytic graphite," *Carbon*, vol. 39, no. 8, pp. 1183–1193, 2001.
87. R. Windholz and P. A. Molian, "Nanosecond pulsed excimer laser machining of chemical vapour deposited diamond and highly oriented pyrolytic graphite: Part I An experimental investigation," *Journal of materials science*, vol. 32, no. 16, pp. 4295–4301, 1997.
88. C. Germain, C. Girault, R. Gisbert, J. Aubreton, and A. Catherinot, "KrF laser photo-ablation of a graphite target: application to the development of thin films," *Diamond and related Materials*, vol. 3, no. 4-6, pp. 598–601, 1994.
89. D. J. Krajnovich, "Laser sputtering of highly oriented pyrolytic graphite at 248 nm," *The Journal of chemical physics*, vol. 102, no. 2, pp. 726–743, 1995.
90. H. C. Ong and R. P. H. Chang, "Effect of laser intensity on the properties of carbon plasmas and deposited films," *Physical Review B*, vol. 55, no. 19, p. 13 213, 1997.
91. C. D. Roberts, M. A. Marciniak, and G. P. Perram, "Pulsed ablation of carbon/graphite surfaces and development of plume-kinetics model," in *Laser-Induced Damage in Optical Materials: 2011*, G. J. Exarhos, V. E. Gruzdev, J. A. Menapace, D. Ristau, and M. J. Soileau, Eds., vol. 8190, Boulder: International Society for Optics and Photonics, Oct. 2011, 81901F.

92. C. D. Roberts, R. A. Acosta, M. A. Marciniak, and G. P. Perram, "Hyperspectral and gated ICCD imagery for laser irradiated carbon materials," *High-Power Laser Materials Processing: Lasers, Beam Delivery, Diagnostics, and Applications II*, vol. 8603, no. February 2013, 86030Q, 2013.
93. S. Bardy, B. Aubert, L. Berthe, P. Combis, D. Hébert, E. Lescoute, J.-L. Rullier, and L. Videau, "Numerical study of laser ablation on aluminum for shock-wave applications: development of a suitable model by comparison with recent experiments," *Optical Engineering*, vol. 56, no. 1, p. 011 014, 2016.
94. D. C. Swift, T. E. Tierney IV, R. A. Kopp, and J. T. Gammel, "Shock pressures induced in condensed matter by laser ablation," *Physical Review E*, vol. 69, no. 3, p. 36 406, 2004.
95. P. T. Murray and E. Shin, "Formation of silver nanoparticles by through thin film ablation," *Materials Letters*, vol. 62, no. 28, pp. 4336–4338, 2008.
96. T. T. P. Nguyen, R. Tanabe-Yamagishi, and Y. Ito, "Impact of liquid layer thickness on the dynamics of nano- to sub-microsecond phenomena of nanosecond pulsed laser ablation in liquid," *Applied Surface Science*, 2019.
97. A. E. Gonzales, N. C. Herr, and G. P. Perram, "Experimental study of laser irradiated graphite oxidation using IFTS," *Combustion and Flame*, vol. 192, pp. 180–189, 2018.
98. GraphiteStore.com, *PG-SN Pyrolytic Graphite Data Sheet*, 2020.

99. A. Butland and R. Maddison, "The specific heat of graphite: An evaluation of measurements," *Journal of Nuclear Materials*, vol. 49, no. 1, pp. 45–56, Nov. 1973.
100. G. Glockler, "The Heat of Sublimation of Graphite and the Composition of Carbon Vapor," *The Journal of Chemical Physics*, vol. 22, no. 59, pp. 159–161, 1954.
101. W. Bauer, G. P. Perram, and T. Haugan, "Comparison of plume dynamics for laser ablated metals: Al and Ti," *Journal of Applied Physics*, vol. 123, no. 9, p. 095 304, 2018.
102. A. V. Gusarov, A. G. Gnedovets, and I. Smurov, "Gas dynamics of laser ablation: influence of ambient atmosphere," *Journal of Applied Physics*, vol. 88, no. 7, pp. 4352–4364, 2000.
103. K.-R. Chen, J. N. Leboeuf, R. F. Wood, D. B. Geohegan, J. M. Donato, C. L. Liu, and A. A. Puretzky, "Mechanisms affecting kinetic energies of laser-ablated materials," *Journal of Vacuum Science & Technology A: Vacuum, Surfaces, and Films*, vol. 14, no. 3, pp. 1111–1114, 1996.
104. Y. B. Zel'Dovich and Y. P. Raizer, *Physics of shock waves and high-temperature hydrodynamic phenomena*, Dover 2002. Mineola: Dover Publications Inc., 2002.
105. S. Mahmood, R. S. Rawat, S. V. Springham, T. L. Tan, and P. Lee, "Material ablation and plasma plume expansion study from Fe and graphite targets in Ar gas atmosphere," *Applied Physics A*, vol. 101, no. 4, pp. 695–699, 2010.
106. A. Misra, A. Mitra, and R. K. Thareja, "Diagnostics of laser ablated plasmas using fast photography," *Applied Physics Letters*, vol. 74, pp. 929–931, 1999.

107. R. F. Wood, K. R. Chen, J. N. Leboeuf, A. A. Puretzky, and D. B. Geohegan, "Dynamics of plume propagation and splitting during pulsed-laser ablation," *Physical Review Letters*, vol. 79, no. 8, p. 1571, 1997.
108. D. Yadav, V. Gupta, and R. K. Thareja, "Ground state C2 density measurement in carbon plume using laser-induced fluorescence spectroscopy," *Spectrochimica Acta - Part B Atomic Spectroscopy*, vol. 64, no. 10, pp. 986–992, 2009.
109. M. R. Querry, "Optical constants," Missouri Univ-Kansas City, Tech. Rep., 1985.
110. H. Alsmeyer, "Density profiles in argon and nitrogen shock waves measured by the absorption of an electron beam," *Journal of Fluid Mechanics*, vol. 74, no. 3, pp. 497–513, 1976.
111. A. Chikitkin, B. Rogov, G. Tirskey, and S. Utyuzhnikov, "Effect of bulk viscosity in supersonic flow past spacecraft," *Applied Numerical Mathematics*, vol. 93, pp. 47–60, 2015, International Conference Difference Schemes and Applications in Honor of the 90-th Birthday of Professor V. S. Ryaben'kii.
112. T. G. Elizarova, A. A. Khokhlov, and S. Montero, "Numerical simulation of shock wave structure in nitrogen," *Physics of Fluids*, vol. 19, no. 6, p. 068 102, 2007.
113. P. Jordan, *Chemical kinetics and transport*. New York: Springer US, 1979.
114. S. S. Batsanov, "Van der Waals radii of elements," *Inorganic Materials*, 2001.
115. K. Hansen and D. F. Hornig, "Thickness of shock fronts in argon," *The Journal of Chemical Physics*, vol. 33, no. 3, pp. 913–916, 1960.

116. A. O. Dikovska, M. T. Alexandrov, G. B. Atanasova, N. T. Tsankov, and P. K. Stefanov, "Silver nanoparticles produced by PLD in vacuum: Role of the laser wavelength used," *Applied Physics A: Materials Science and Processing*, vol. 113, pp. 83–88, 2013.
117. S. Machmudah, Wahyudiono, N. Takada, H. Kanda, K. Sasaki, and M. Goto, "Fabrication of gold and silver nanoparticles with pulsed laser ablation under pressurized CO<sub>2</sub>," *Advances in Natural Sciences: Nanoscience and Nanotechnology*, vol. 4, no. 4, p. 045 011, 2013.
118. C. J. Druffner, P. D. Kee, M. A. Lange, G. P. Perram, R. R. Biggers, and P. N. Barnes, "Optical diagnostics for pulsed laser ablation," *Journal of Directed Energy*, vol. 1, no. 3, pp. 203–218, 2005.
119. Y. Chang, C. M. Yee, W. P. Fahy, A. Kafi, S. Bateman, H. Wu, and J. H. Koo, "Design of Additively-Manufactured Lattice Structure for Thermal Protection System: Thermal Characterization and Ablation Performance," in *AIAA Scitech 2021 Forum*, American Institute of Aeronautics and Astronautics, Inc., 2021, p. 671.
120. J. Wu, X. Li, W. Wei, S. Jia, and A. Qiu, "Understanding plume splitting of laser ablated plasma: A view from ion distribution dynamics," *Physics of Plasmas*, vol. 20, no. 11, 2013.
121. J. M. Gordon, K. C. Gross, and G. P. Perram, "Temperature dynamics of aluminized cyclotrimethylenetrinitramine fireballs for event classification," *Optical Engineering*, vol. 53, no. 2, p. 021 106, 2013.

122. R. Ravichandran, S. W. Lewis, C. M. James, R. G. Morgan, and T. J. McIntyre, “Graphite ablation and radiation on interaction with hypervelocity earth-entry flows,” *Journal of Thermophysics and Heat Transfer*, vol. 35, no. 2, pp. 335–348, 2021.
123. R. Maljaei, A. H. Sari, and D. Dorrnian, “Optical properties of pva films doped with gold-graphene nanocomposite synthesized by pulsed laser ablation,” in *Journal of Nano Research*, Trans Tech Publ, vol. 68, 2021, pp. 123–137.
124. D. Fulvio, L. F. Maron, Y. C. Perez, T. Del Rosso, *et al.*, “Micrometeorite bombardment simulated by ns-pulsed laser ablation: Morphological characterization of the impact craters,” *Icarus*, vol. 366, p. 114 532, 2021.
125. R. Russo, A. Bolshakov, J. Yoo, and J. Gonzalez, “Laser ablation plasmas for diagnostics of structured electronic and optical materials during or after laser processing,” vol. 8243, Jul. 2012.
126. M. Kuzmanovic, D. Rankovic, M. Trtica, J. Ciganovic, J. Petrovic, and J. Savovic, “Optical emission of graphite plasma generated in ambient air using low-irradiance carbon dioxide laser pulses,” *Spectrochimica Acta - Part B Atomic Spectroscopy*, 2019.
127. B. A. Pierce, “CN and C<sub>2</sub> Spectroscopy on the Pulsed Ablation of Graphite in the Visible Spectrum,” Thesis, Air Force Institute of Technology, 2020.

128. S. H. Jeong, R. Greif, and R. E. Russo, “Shock wave and material vapour plume propagation during excimer laser ablation of aluminum samples,” *Journal of Physics D: Applied Physics*, vol. 32, no. 19, pp. 2578–2585, 1999.
129. F. Davanloo, E. Juengerman, D. Jander, T. Lee, C. Collins, and E. Matthias, “Mass flow in laser-plasma deposition of carbon under oblique angles of incidence,” *Applied Physics A*, vol. 54, no. 4, pp. 369–372, 1992.
130. A. Chatterjee, M. E. Decoster, A. M. Mark, X. Zhu, and K. A. Iyer, “Directed energy illumination visualization (DEIVI) physics-based laser ablation models and software user manual version 3.2,” The Johns Hopkins University Applied Physics Laboratory (APL), Laurel, MD, Tech. Rep., 2018.

# REPORT DOCUMENTATION PAGE

*Form Approved*  
OMB No. 0704-0188

The public reporting burden for this collection of information is estimated to average 1 hour per response, including the time for reviewing instructions, searching existing data sources, gathering and maintaining the data needed, and completing and reviewing the collection of information. Send comments regarding this burden estimate or any other aspect of this collection of information, including suggestions for reducing this burden to Department of Defense, Washington Headquarters Services, Directorate for Information Operations and Reports (0704-0188), 1215 Jefferson Davis Highway, Suite 1204, Arlington, VA 22202-4302. Respondents should be aware that notwithstanding any other provision of law, no person shall be subject to any penalty for failing to comply with a collection of information if it does not display a currently valid OMB control number. **PLEASE DO NOT RETURN YOUR FORM TO THE ABOVE ADDRESS.**

<b>1. REPORT DATE</b> (DD-MM-YYYY) 16-09-2021		<b>2. REPORT TYPE</b> Doctoral Dissertation		<b>3. DATES COVERED</b> (From — To) Sept 2018 — Sep 2021				
<b>4. TITLE AND SUBTITLE</b>  Improvements to Emissive Plume and Shock Wave Diagnostics and Interpretation During Pulsed Laser Ablation of Graphite			<b>5a. CONTRACT NUMBER</b>					
			<b>5b. GRANT NUMBER</b>					
			<b>5c. PROGRAM ELEMENT NUMBER</b>					
			<b>5d. PROJECT NUMBER</b>					
			<b>5e. TASK NUMBER</b>					
<b>6. AUTHOR(S)</b>  Calver, Timothy I, Major, USAF			<b>5f. WORK UNIT NUMBER</b>					
			<b>7. PERFORMING ORGANIZATION NAME(S) AND ADDRESS(ES)</b> Air Force Institute of Technology Graduate School of Engineering and Management (AFIT/EN) 2950 Hobson Way Wright-Patterson AFB OH 45433-7765			<b>8. PERFORMING ORGANIZATION REPORT NUMBER</b>  AFIT-ENP-DS-21-S-023		
						<b>9. SPONSORING / MONITORING AGENCY NAME(S) AND ADDRESS(ES)</b>  Intentionally Left Blank		
<b>11. SPONSOR/MONITOR'S REPORT NUMBER(S)</b>								
			<b>12. DISTRIBUTION / AVAILABILITY STATEMENT</b>  DISTRIBUTION STATEMENT A. APPROVED FOR PUBLIC RELEASE: DISTRIBUTION UNLIMITED.					
<b>13. SUPPLEMENTARY NOTES</b>  This work is declared a work of the U.S. Government and is not subject to copyright protection in the United States.								
<b>14. ABSTRACT</b>  This dissertation covers nanosecond pulsed laser ablation of graphite for 4–5.7 J/cm <sup>2</sup> fluences with 248 nm and 532 nm lasers in 1–180 Torr helium, argon, nitrogen, air, and mixed gas. Three experiments were performed to improve the interpretation of common diagnostics used to characterize pulsed laser ablation, find simple but universal scaling relationships for comparing dynamics across different materials and ablation conditions, and provide a systematic analysis of graphite emissive plume and shock wave dynamics. A scaling of the Sedov-Taylor energy ratio was developed and validated for a range of studies despite differences in wavelength, pulse duration, fluence, and target material. Normalized shock thickness for Mach 48 plumes were compared to prior ablation and shock tube studies (Mach ≤ 10) using a common analytical model. Shock detachment distances were identified by comparing plume and schlieren shock propagation trajectories. The shock detachment points were used to improve Sedov-Taylor blast analysis, allowing for enhanced estimates of laser-plume energy coupling. Finally, plume and shock wave morphology were compared.								
<b>15. SUBJECT TERMS</b>  pulsed laser ablation, schlieren, shock detachment, optical emission imaging								
<b>16. SECURITY CLASSIFICATION OF:</b>			<b>17. LIMITATION OF ABSTRACT</b>	<b>18. NUMBER OF PAGES</b>	<b>19a. NAME OF RESPONSIBLE PERSON</b>			
<b>a. REPORT</b>	<b>b. ABSTRACT</b>	<b>c. THIS PAGE</b>			Dr. Glen P. Perram, AFIT/ENP			
U	U	U	UU	154	<b>19b. TELEPHONE NUMBER</b> (include area code) (937) 255-3636 x4504; glen.perram@afit.edu			